Conceptual Design of the Spin Rotator for the SuperKEKB High Energy Ring

by

Yuhao Peng
B.Sc., University of Victoria, 2019

A Thesis Submitted in Partial Fulfillment of the
Requirements for the Degree of

MASTER OF SCIENCE

in the Department of Physics and Astronomy

Conceptual Design of the Spin Rotator for the SuperKEKB High Energy Ring

by

Yuhao Peng
B.Sc., University of Victoria, 2019

Supervisory Committee

Dr. J. Michael Roney, Supervisor
(Department of Physics and Astronomy)

Dr. Tobias Junginger, Departmental Member
(Department of Physics and Astronomy)

ABSTRACT

This project focuses on the conceptual design of the spin rotator for a proposed electron polarization upgrade of the SuperKEKB. The goal is to achieve the longitudinal electron polarization at the interaction point (IP). In this design, four existing dipoles will be replaced with four rotator magnets on both sides of the IP. The rotator magnet structure consists of dipole-solenoid combined function magnets with skew-quadrupoles installed on top to decouple the x-y plane. The advantage of this design is that the original machine geometry is maintained, and the original machine can be recovered by turning off the solenoid-quadrupole in the rotator magnet. With Bmad, a powerful lattice simulation tool applied to perform the optimizations for this design, the longitudinal spin alignment at the IP reaches a significantly high level, greater than 99.99%. Furthermore, the influence of the installation of the spin rotator on the original machine dynamics is minimized to an acceptable level.

Contents

List of Tables

List of Figures

ACKNOWLEDGEMENTS

I would like to thank:

Dr. J. Michael Roney, for the encouragement and valuable advice in my research and academic career.

Dr. Uli Wienands, for proposing the fundamental idea of this project and his patient guidance and supervision of the project.

Dr. David Sagan, for helping us build the BMAD model of the spin rotator magnet, and guidance on the use of BMAD.

Dr. Tobias Junginger, for teaching me particle accelerator physics, and valuable advice in my research.

Dr. Mika Masuzawa, Dr. Rejun Yang, and Dr. Demin Zhou for providing technical details and the lattice file of the SuperKEKB High Energy Ring.

Dr. Thomas Planche, for giving helpful suggestions on the beam tracking.

Mr. Caleb Miller, for giving useful advice in thesis writing.

It doesn't matter, it's all the same.
Zhang, Beihai

Chapter 1

Introduction

The SuperKEKB is a high luminosity positron-electron particle collider with a circumference of 3 km located in Japan. SuperKEKB collides 7 GeV electrons with 4 GeV positrons at the centre-of-momentum energy of 10.58 GeV close to the mass of Υ(4S). A proposed electron polarization upgrade program is being considered for SuperKEKB [1]. Polarized electron beam provides precise measurements of electroweak parameters in the process $e^+ + e^- \to f\bar{f}$, where f denotes the fermion (e, μ, τ, c-quark, b-quark). The measurement of the left-right asymmetry A_{LR}^f for each identified final-state of the non-electron fermion-pair (μ, τ, c-quark, b-quark) can determine neutral current vector coupling g_V^f of the fermion (μ, τ, c-quark, b-quark) through the relation for full acceptance, s-channel $f\bar{f}$ production:

$$A_{LR}^f = \frac{\sigma_L - \sigma_R}{\sigma_L + \sigma_R} = \frac{sG_F}{\sqrt{2}\pi\alpha Q_f} g_A^e g_V^f \langle Pol \rangle,$$

with

$$g_V^f = T_3^f - 2Q_f \sin^2\theta_W,$$

where the superscript f denotes the non-electron fermion (μ, τ, c-quark, b-quark), T_3^f is the 3rd component of weak isospin of f, Q_f is the electric charge of f in units of electron charge, θ_W is the weak mixing angle, σ_L, σ_R denote the left, right interaction cross sections, g_A^e=T_3^e =-$\frac{1}{2}$ is the neutral current axial coupling of the electron, G_F is the Fermi coupling constant, s is the square of the centre-of-mass energy, and $\langle Pol \rangle$ is the average beam polarization of the electron, which is given by:

$$\langle Pol \rangle = \frac{1}{2}\left[\left(\frac{N_{eR} - N_{eL}}{N_{eR} + N_{eL}} \right)_{\mathbf{R}} - \left(\frac{N_{eR} - N_{eL}}{N_{eR} + N_{eL}} \right)_{\mathbf{L}} \right],$$

where N_{eR} and N_{eL} denote the the number of left-handed and right-handed electrons in the left and right polarized beam bunch, which is denoted by **L**, **R**, respectively.

Note that the $e^+e^- \to e^+e^-$ Bhabha scattering includes a t-channel component with A_{LR} sensitivity to θ_W given in Reference [2]. Also, electroweak studies of u-$\bar{\text{u}}$, d-$\bar{\text{d}}$ and s-$\bar{\text{s}}$ final states are also possible, but not where they are separately identified. With the high luminosity of the SuperKEKB and the 70% (with a systematic error smaller than $\pm$ 0.5%) polarized electron beam, the precision of the weak measurements can reach an unprecedented level [1].

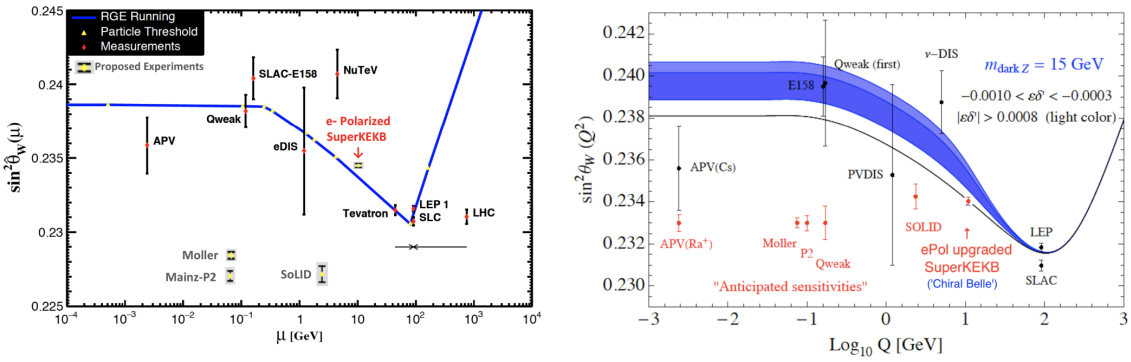

Figure 1.1: Left: Existing measurements of $\sin^2\theta_W$ and projected measurements at future experimental facilities as a function of energy scale. Right: Dark blue band indicates the Q^2-dependent shift in $\sin^2\theta_W$ caused by a 15 GeV mass dark Z.

Figure 1.1 [1] shows the existing measurements of the $\sin^2\theta_W$ as function of the energy scale and the future measurements including the electron polarization upgraded SuperKEKB. With 20 ab^{-1} data and 70% polarized electron beam, the ratio of the vector couplings g_V^b/g_V^c will be measured to 0.3% which is more an order-of-magnitude precise than existing measurements. With 40 ab^{-1} data, $\sin^2\theta_W$ can be measured with a statistics-dominated uncertainty of $\pm$ 0.00016, which is equal to the

world average from the LEP and SLD experiments at Z^0 pole and more than twice as precise as the current world average from LHC. Also, the electron polarization upgrade provides the possibility to search for the "Dark Sector", especially when the off-shell energy of the Z_{dark} is between $\sim$ 10 to 35 GeV, or even up the Z^0 pole, or it couples to the 3rd generation [1].

The electron polarization upgrade includes three hardware upgrades for the SuperKEKB High Energy Ring (HER)/Electron Ring [1]: a low emittance source to provide a longitudinally polarized electron beam which will be transversely polarized before it reaches the injection point, a spin rotator to polarize the beam longitudinally at the interaction point(IP), and a Compton polarimeter installed before the IP to measure the beam polarization.

This project focuses on the spin rotator design. There are four types of magnets (solenoid, dipole, Wien filter, and helical dipole) that can be applied to provide the spin rotation [3]. The solenoid magnet induces the magnetic field in the longitudinal direction and provides spin rotation along the longitudinal axis. The dipole magnets provide the spin rotation in the horizontal plane, and the vertical spin is preserved. The Wien filter is a combination of the transverse electrical and magnetic fields that can offer spin rotation without bringing orbit distortion to the beam. The helical dipole has a helical structure which gives an additional degree of freedom compared with the normal dipoles and the orbit excursion in the helical dipole magnet.

The spin rotating device introducing a 180 degrees spin rotation for each turn is called the "Siberian Snake", which was conceptually developed by Ya.S. Derbenev and A.M. Kondratenko in Budker Institute in Novosibirsk in 1976 [4]. The Siberian Snake can be applied to eliminate the depolarization effects, allowing the spin polarization to be preserved after the beam undergoes many revolutions in the ring. Relativistic Heavy Ion Collider (RHIC) is the first polarized proton collider, and with the installation of two Siberian Snakes made of helical dipoles in each ring, it is also the first polarized proton collider with no polarization loss [5].

The spin rotator is a spin rotating device for beam polarization purposes. The first electron storage ring which provided longitudinal spin polarization was the Hadron-Electron Ring Accelerator (HERA) [6]. It is a lepton-position particle collider at

DESY in Hamburg and operating from 1992 to 2007. HERA collided a positron or electron with the proton at a center of mass energy of 318 GeV. With the installation of the three pairs of the spin rotator, the longitudinal beam polarization was achieved at three collision points in HERA, as shown in **Figure 1.2** [6]. The Mini-Rotator in HERA was made of six alternating bends, including three horizontal bends and three vertical bends [7].

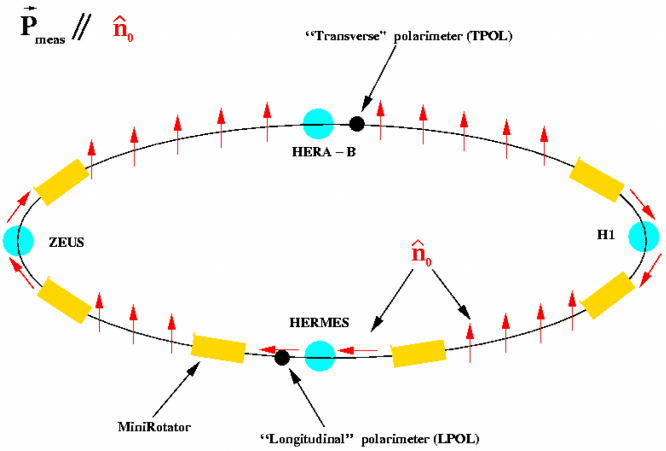

Figure 1.2: The HERA electron storage ring

This project aims at designing the spin rotator with the dipole-solenoid combined function function magnets for the electron polarization upgrade of the SuperKEKB HER. The left picture [8] in **Figure 1.3** shows the SuperKEKB collider, the right picture shows the spin motion in the KEK frame when rotator is installed in the HER. As it shows, the full spin rotator structure has two components: the left rotator (L-Rot) is installed before the IP to polarize the electron beam in the longitudinal direction; the right rotator (R-Rot) is located downstream of the IP to bring thelectron polarization back to the transverse. Thelectron polarization at the IP depends on thelectron polarization at the injection point. With the injected beam polarized in the direction aligned with the dipole field, thelectron polarization at the IP is longitudinal (Right-handed) and anti-aligned with the dipole field corresponds to the anti-longitudinal polarization (Left-handed). The dipole field direction is downward in the KEK frame [8].

The structure of this thesis follows: **Chapter 2** describes the theory of accelerator

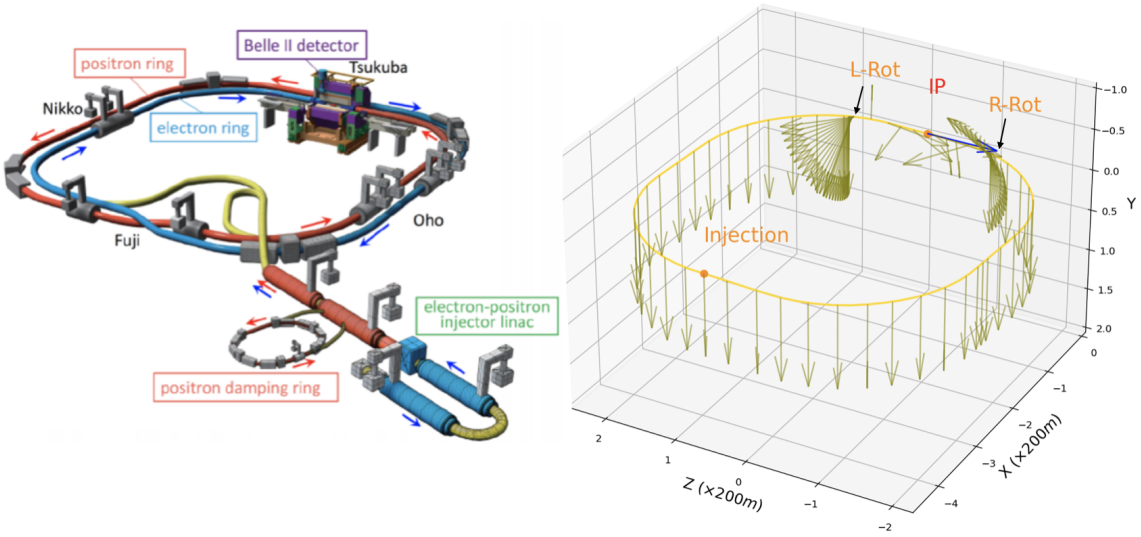

Figure 1.3: Spin motion of the electron (KEK frame) in the High Energy Ring with spin rotator installed, the L-Rot is located $\sim$ 210 m upstream of the IP, and the R-Rot is located at $\sim$ 169 m downstream of the IP. The blue arrow at the IP is the Right-handed polarized spin.

physics and spin dynamics relevant to this project. **Chapter 3** gives the fundamental idea of the rotator design, including the magnet structure, constraints, and discussion of the installation position. Next, **Chapter 4** talks about the lattice simulation tool, details about the simulation and optimization procedures, and the optimization results. Finally, **Chapter 5** discusses the future steps that need to be performed to finalize the design of the spin rotator and also includes the implementation of beam tracking, and **Chapter 6** is the conclusion.

Chapter 2

Theory of Accelerator Physics and Spin Dynamics

2.1 Linear Optics

In magnetic field, a charged particle experiences the Lorentz force, which provides the centripetal force causing the particle to follow a circular trajectory. The relation between the magnetic field and the curvature of the circular motion, R, is given by:

$$\frac{1}{R} = \frac{q}{p}B, \tag{2.1}$$

where B is magnetic field, q is the charge of the particle, and p is the momentum of the particle.

In the ideal case, particles follow the ideal orbit. However, the beam oscillates around the ideal orbit within a small range in the circular accelerator. Consider a small horizontal displacement x to the ideal orbit, and Taylor expand the magnetic field to get the expression for the multipole field:

$$B = B_0 + \frac{dB}{dx}x + \frac{1}{2!}\frac{d^2B}{dx^2}x^2 + ..., \tag{2.2}$$

Multiplying by $\frac{q}{p}$ gives the strength of multipoles :

$$\begin{aligned}\frac{q}{p}B &= \frac{q}{p}B_0 + \frac{q}{p}\frac{dB}{dx}x + \frac{1}{2!}\frac{q}{p}\frac{d^2B}{dx^2}x^2 + ... \\ &= \frac{1}{R} + kx + \frac{1}{2!}mx^2 + ...\end{aligned} \tag{2.3}$$

$\frac{1}{R}$ corresponds to the dipole strength, k the quadrupole strength, m the sextupole strength, etc [9]. In a circular accelerator, multipoles are installed for different purposes: dipoles are applied to bend the beam, quadrupoles are applied for the beam focusing, and sextupoles are used for the chromaticity compensation which will be explained in **Section 2.1.4**.

2.1.1 Co-Moving Coordinate

The way to track particles' trajectories in the accelerator is through the ideal orbit, also called 'orbit'. The ideal orbit passes through the center of the cross-section of each magnet along the longitudinal direction, so it is defined by the machine's geometry. The co-moving coordinate system, introduced to describe each particle's trajectory, has an origin moving along the ideal orbit in the longitudinal direction. As **Figure 2.1** [9] shows, in this coordinate system, the transverse position of the particle relative to the ideal orbit is denoted by x for the horizontal position, y for the vertical, and s for the origin position in the reference orbit.

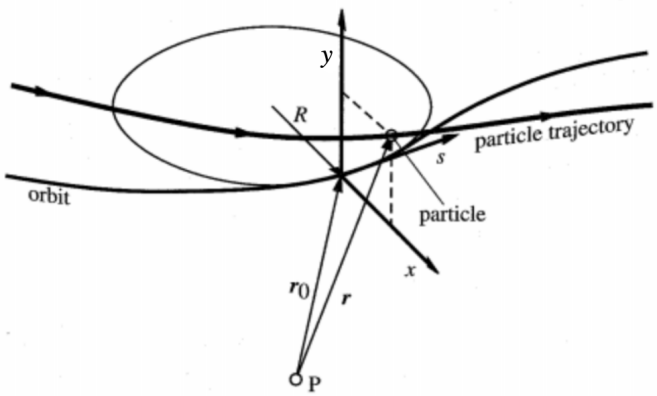

Figure 2.1: co-moving coordinate system

2.1.2 Hill's Equation

The transverse motion of a particle in the synchrotron is described by Hill's equation [9]:

$$x''(s) + K(s)x(s) = 0, \tag{2.4}$$

with

$$K(s) = \frac{1}{R(s)} - k(s), \tag{2.5}$$

where x is transverse trajectory of the particle, R is the local bending radius, k is the quadrupole strength.

Hill's equation can not be solved analyitcally but the solution can be expressed in following form :

$$x(s) = \sqrt{\varepsilon\beta(s)}\cos\big(\Psi(s) + \phi\big), \tag{2.6}$$

where $\beta(s)$ is the amplitude function depending on local magnetic structure, the constant ε is known as the emittance, ϕ is the initial phase, and $\Psi(s)$ is the phase function and given by $\Psi(s) = \int_0^s \frac{d\sigma}{\beta(\sigma)}$. It describes a transverse motion that oscillates around the reference orbit with a positional dependent amplitude, called betatron oscillation.

The speed of the transverse motion is given by:

$$x'(s) = -\sqrt{\frac{\varepsilon}{\beta}}\Big[\alpha\cos\big(\Psi(s) + \phi\big) + \sin\big(\Psi(s) + \phi\big)\Big], \tag{2.7}$$

Where $\alpha \equiv -\frac{\beta'(s)}{2}$.

Manipulating the expression of x and x' can determine following equations:

$$\cos\big(\Psi(s) + \phi\big) = \frac{x}{\sqrt{\varepsilon\beta(s)}}, \tag{2.8}$$

$$\sin\big(\Psi(s)+\phi\big)=\sqrt{\frac{\beta(s)}{\varepsilon}}x'(s)+\frac{\alpha(s)x(s)}{\sqrt{\varepsilon\beta(s)}}. \tag{2.9}$$

Applying the identity $\sin^2\theta+\cos^2\theta=1$ can get:

$$\frac{x^2}{\beta(s)}+\Big(\frac{\alpha(s)}{\sqrt{\beta(s)}}+\sqrt{\beta(s)}x'\Big)^2=\varepsilon, \tag{2.10}$$

α,β,γ are known as Twiss parameters, where $\gamma(s)\equiv\frac{1+\alpha^2(s)}{\beta(s)}$, and rewrite the equation above in following form:

$$\gamma x^2+2\alpha xx'+\beta x'^2=\varepsilon. \tag{2.11}$$

It is an ellipse equation, the area of the ellipse is given by $\pi\varepsilon$, as shown in **Figure 2.2** [10]. According to Liouville's theorem, the area of the phase space is invariant, which indicates the emittance is an invariant quantity.

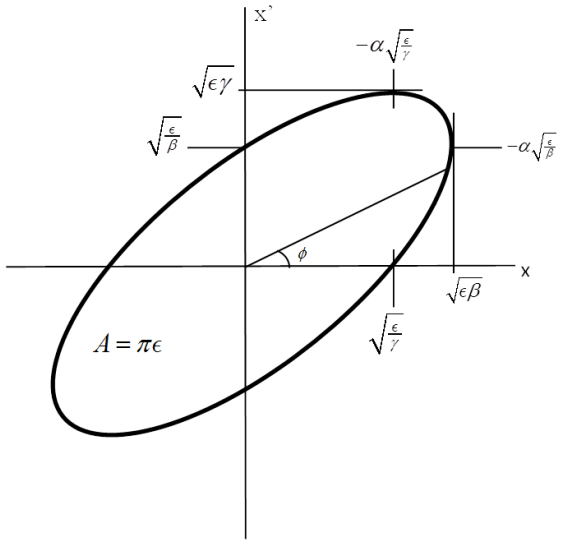

Figure 2.2: The ellipse in the x-x' phase space

2.1.3 Tune

The repeated magnetic structure that the beam travels through in the circular machine might introduce a resonance to the beam motion, which amplifies the transverse amplitude rapidly. This is called an optical resonance. The resonant behaviour of the betatron oscillation significantly depends on the phase advance over a complete revolution [9]:

$$\Delta\Psi = \Psi(s+L) - \Psi(s), \tag{2.12}$$

where L denotes the circumference of the ring.

To study the optical resonance, the Tune value Q is defined to describe the betatron oscillation number over the full orbit

$$Q \equiv \frac{\Delta\Psi}{2\pi} = \frac{1}{2\pi}\int_0^L \frac{ds}{\beta(s)} = \frac{1}{2\pi}\oint \frac{ds}{\beta(s)}. \tag{2.13}$$

Also define the normalized quantities: $\phi(s) \equiv \frac{\Psi(s)}{Q}$ is the normalized phase; $\eta(s) \equiv \frac{x(s)}{\sqrt{\beta(s)}}$ is the normalized amplitude. Consider the dipole field offset, ΔB and applying the Floquet's theorem can show that [9]

$$\eta(\phi) = \frac{Q}{2\sin\pi Q}\int_\phi^{\phi+2\pi} \beta^{\frac{3}{2}}\frac{\Delta B}{RB}\cos\big[Q(\pi+\phi+\theta)\big]d\theta. \tag{2.14}$$

It is obvious to see that the amplitude blows up when Q is an integer. It describes a physical picture that transverse motion continues to be amplified by the same field error when a particle reaches the field with the same betatron phase after many revolutions. Thus, integer Q should be avoided. It also can be shown that half-integer Q corresponds to the resonance caused by quadrupole field error, third-integer Q corresponds to the sextupoles resonance, etc.

The transverse beam motion has two components, the horizontal and the vertical. Therefore, it has two Tune values, Q_x for the horizontal, Q_y for the vertical. The coupled resonances have to be considered, and the optical resonances occur when

$$mQ_x + nQ_y = p, \tag{2.15}$$

where m,n,p are integers, and $|m| + |n|$ gives the order of resonance. It describes the linear relation between Q_x and Q_y for the optical resonance condition. The choice of Tunes referred to as the 'working point' should avoid these resonance lines. Usually, the choice of the working point is considered up to fifth-order because of the rapid reduction of resonance with the order [9]. Also, since p is an arbitrary integer number, the integer component of the Tunes is irrelevant to the choice of working point; only the fractional component matters. As **Figure 2.3** shows an example of the Tune diagram, linear lines correspond to the optical resonance, the choice of the working point should avoid them.

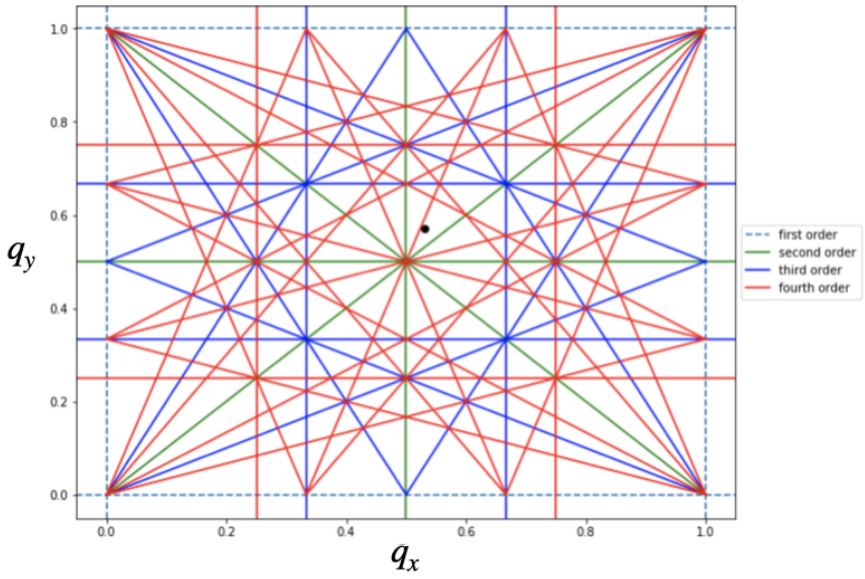

Figure 2.3: Tune Diagram (up to 4th order): the black dot is the working point; linear lines corresponding to the optical resonance are computed from Eq.2.15; $q_x = Q_x - \lfloor Q_x \rfloor$, $q_y = Q_y - \lfloor Q_y \rfloor$ denote the fractional component of horizontal and vertical Tunes

2.1.4 Chromaticity

For the small quadrupole error Δk, the tune shift is given by [9]:

$$4\pi dQ = \Delta k \beta ds. \tag{2.16}$$

The quadrupole strength k is given by $k = \frac{q}{p}g$, where g is the field gradient. Let p_0 denote the reference momentum of the particle, and Δk denotes the quadrupole field error. Take the first-order approximation, and the quadrupole field error due to the momentum deviation Δp is given by:

$$\Delta k \simeq \frac{\partial k}{\partial p}\Big|_{p=p_0} \Delta p = -g\frac{q}{p_0}\frac{\Delta p}{p_0} = -\frac{\Delta p}{p_0}k_0. \tag{2.17}$$

Thus, the tune shift introduced by the momentum deviation is given by:

$$dQ = -\frac{\Delta p}{p_0}\frac{1}{4\pi}k_0\beta(s)ds. \tag{2.18}$$

The chromaticity is defined as the ratio of the Tune shift and the momentum deviation:

$$\xi \equiv \frac{\Delta Q}{\Delta p/p} = -\frac{1}{4\pi}\oint k(s)\beta(s)ds. \tag{2.19}$$

It can be seen immediately that the natural chromaticity is a negative value if there is a strong focusing effect in the ring because k is positive for focusing quadrupoles. Negative chromaticity can cause head-tail instability [9]. Also, small momentum can cause a significant Tune shift when chromaticity is large, leading to optical resonances. Thus, it is necessary to compensate for the chromaticity by installing sextupoles to provide extra quadrupole strength $k_{sext} = mD\frac{\Delta p}{p}$, where m is the sextupole strength, and D is the dispersion function. In addition, it is beneficial to overcompensate the chromaticity, which prevents the field error from driving the chromaticity back to negative and positive chromaticity leads to head-tail damping [9].

2.2 Spin Dynamics

The Thomas BMT equation [11] describes the spin motion of a charged particle traveling in the electromagnetic field:

$$\frac{d\vec{s}}{dt} = \vec{\Omega} \times \vec{S} = -\frac{q}{m\gamma}\big((1+a\gamma)\vec{B}_{\perp} + (1+a)\vec{B}_{//} + (a\gamma + \frac{\gamma}{1+\gamma})\frac{\vec{E}\times\vec{\beta}}{c}\big) \times \vec{S}, \quad (2.20)$$

where $\vec{S}$ is the spin vector in the rest frame of the particle; t is the time in the lab frame; q is the charge of the particle; $\vec{B}_{\perp}$ and $\vec{B}_{//}$ are the transverse and longitudinal component of the magnetic field with respect to the velocity of the particle in the lab frame; $\vec{E}$ is the electric field in the lab frame; the velocity of the particle is given by $\vec{\beta}c$ and c is the speed of light; γ is the Lorentz factor; $a = \frac{g-2}{2}$ is the anomalous gyromagnetic g-factor; $\vec{\Omega}$ is the axial vector of the spin precession.

The derivation of the solution to the Thomas BMT equation is developed as following. For electron, the charge q = -e, where e is the elementary charge. Since there is no transverse electric field in the SuperKEKB High Energy Ring (HER), the $\vec{E}$ field term vanishes. Taking the approximation $\frac{ds}{dt} \simeq v$ can express the equation as:

$$\frac{d\vec{s}}{ds} = \frac{d\vec{s}}{dt}\frac{dt}{ds} = \frac{1}{v}\frac{d\vec{s}}{dt} = \frac{e}{p_0}\big((1+a\gamma)\vec{B}_{\perp} + (1+a)\vec{B}_{//}\big) \times \vec{S}, \quad (2.21)$$

where s is the s-position, v is the reference speed of the electron in the ring, p_0 is the reference momentum of the electron in the HER, which is about 7 GeV/c. Note that $\frac{P_0}{e}$ is equal to the magnetic rigidity $B\rho$ of the ring.

There is no vertical bending in the ring, so the transverse field is in the vertical direction $\hat{y}$, the longitudinal direction is denoted as $\hat{z}$. Let $\frac{e}{p_0}(1+a\gamma)\vec{B}_{\perp} = \omega_{\perp}\hat{y}$, $\frac{e}{p_0}(1+a)\vec{B}_{//} = \omega_{//}\hat{z}$, and $\omega = \sqrt{\omega_{//}^2 + \omega_{\perp}^2}$ is the rotational speed. Express the equation in the co-moving coordinate:

$$\frac{d\vec{s}}{ds} = \big(\omega_{\perp}\hat{y} + \omega_{//}\hat{z}\big) \times \vec{S} = \big(-\omega_{//}S_y + \omega_{\perp}S_z\big)\hat{x} + \omega_{//}S_x\hat{y} - \omega_{\perp}S_x\hat{z}. \quad (2.22)$$

Three first order differential equations can be summarized from Eq.2.22:

$$\begin{cases} \dot{S}_x \equiv \frac{dS_x}{ds} = -\omega_{//} S_y + \omega_{\perp} S_z \\ \dot{S}_y \equiv \frac{dS_y}{ds} = \omega_{//} S_x \\ \dot{S}_z \equiv \frac{dS_z}{ds} = -\omega_{\perp} S_x \end{cases} . \tag{2.23}$$

Take the derivative of the equations above and get the second order equations of motion:

$$\begin{cases} \ddot{S}_x \equiv \frac{d^2 S_x}{ds^2} & = -\omega_{//} \dot{S}_y + \omega_{\perp} \dot{S}_z = -\omega^2 S_x \\ \ddot{S}_y \equiv \frac{d^2 S_y}{ds^2} & = \omega_{//} \dot{S}_x = -\omega_{//}^2 S_y + \omega_{//} \omega_{\perp} S_z \\ \ddot{S}_z \equiv \frac{d^2 S_z}{ds^2} & = -\omega_{\perp} \dot{S}_x = \omega_{//} \omega_{\perp} S_y - {\omega_{\perp}}^2 S_z \end{cases} . \tag{2.24}$$

It describes a simple harmonic oscillation in x and a coupled harmonic oscillation in the y-z plane. For S_x, the solution is given by:

$$S_x = A \sin(\omega s + \phi). \tag{2.25}$$

To solve for the coupled motion in the y-z plane, a matrix formalism is developed based on Eq.2.24:

$$\begin{pmatrix} \ddot{S}_y \\ \ddot{S}_z \end{pmatrix} = \begin{pmatrix} -\omega_{//}^2 & \omega_{//}\omega_{\perp} \\ \omega_{//}\omega_{\perp} & -\omega_{\perp}^2 \end{pmatrix} \begin{pmatrix} S_y \\ S_z \end{pmatrix} . \tag{2.26}$$

There are two eigenvalues 0, $-\omega^2$ can be found, and the corresponding normalized eigenvector is $\frac{1}{\omega}\begin{pmatrix} \omega_{\perp} \\ \omega_{//} \end{pmatrix}$, $\frac{1}{\omega}\begin{pmatrix} -\omega_{//} \\ \omega_{\perp} \end{pmatrix}$ respectively. The corresponding eigenvector for the eigenvalue 0 is parallel to the axial vector, which indicates that the component of the spin vector which is parallel to the rotational axis remains unchanged. The eigenvalue

$-\omega^2$ has an eigenvector perpendicular to the rotation axis in the y-z plane, it indicates that the component of the spin vector which is perpendicular to the rotational axis rotates around the axis with an angular speed of ω. The general solution for the spin motion in the y-z plane can be written as:

$$\begin{cases} S_y = -\frac{\omega_{//}}{\omega} B\cos(\omega s + \psi) + \frac{\omega_{\perp}}{\omega} C \\ S_z = \frac{\omega_{\perp}}{\omega} B\cos(\omega s + \psi) + \frac{\omega_{//}}{\omega} C \end{cases} . \tag{2.27}$$

Given the fact that the length of the spin vector is invariant $S_x^2 + S_y^2 + S_z^2 = 1$, it requires B = A, $A^2 + C^2 = 1$, and $\psi = \phi$. The spin motion in the co-moving frame can be represented as:

$$\begin{cases} S_x = A\sin(\omega s + \phi) \\ S_y = -\frac{\omega_{//}}{\omega} A\cos(\omega s + \phi) + \frac{\omega_{\perp}}{\omega} C \\ S_z = \frac{\omega_{\perp}}{\omega} A\cos(\omega s + \phi) + \frac{\omega_{//}}{\omega} C \end{cases} . \tag{2.28}$$

Giving the arbitrary initial spin $\vec{S}_0 = (\tilde{S}_x, \tilde{S}_y, \tilde{S}_z)$ can determine the constants:

$$\begin{cases} C = \frac{\omega_{\perp}\tilde{S}_y + \omega_{//}\tilde{S}_z}{\omega} \\ A\sin\phi = \tilde{S}_x \\ A\cos\phi = \frac{-\omega_{//}\tilde{S}_y + \omega_{\perp}\tilde{S}_z}{\omega} \end{cases} , \tag{2.29}$$

or

$$\begin{cases} C = \frac{\omega_{\perp}\tilde{S}_y + \omega_{//}\tilde{S}_z}{\omega} \\ \phi = \arctan\left(\frac{\omega\tilde{S}_x}{-\omega_{//}\tilde{S}_y + \omega_{\perp}\tilde{S}_z}\right) \\ A = \frac{-\omega_{//}\tilde{S}_y + \omega_{\perp}\tilde{S}_z}{\omega}\cos\phi + \tilde{S}_x\sin\phi \end{cases} . \tag{2.30}$$

Consider the case that there is no solenoid field and only the dipole field exists, the spin motion follows:

$$\begin{cases} S_x = \tilde{S}_x \cos\omega_\perp s + \tilde{S}_z \sin\omega_\perp s \\ S_y = \tilde{S}_y \\ S_z = -\tilde{S}_x \sin\omega_\perp s + \tilde{S}_z \cos\omega_\perp s \end{cases} . \tag{2.31}$$

It describes the spin rotation in the horizontal plane, and the vertical component of the spin vector remains as a constant. The spin vector, which is parallel to the dipole field($S_y = \pm 1$) remains unchanged. The natural spin polarization direction is close to vertical direction in the ring due to bending fields. Thus, the vertical spin is most stable in the ring.

2.3 Coupling Formalism

The spin rotator magnet described in **Section 3.1** requires using solenoids which cause the transverse coupling of the beam motion. To study the coupled motion in the rotator region, the coupling formalism must be developed. Following David Sagan and David Rubin, the formalism is developed as following [12].

Let $\mathbf{T}$ denote the 1-turn map for the transverse beam motion (x, x', y, y'). $\mathbf{T}$ is a 4×4 matrix, and if the off-diagonal terms are zero, the motion is not coupled. T can be transferred to normal mode through:

$$\mathbf{T} = \mathbf{V}\mathbf{U}\mathbf{V}^{-1}. \tag{2.32}$$

$\mathbf{U}$ is uncoupled and has the following form:

$$\mathbf{U} = \begin{pmatrix} \mathbf{A} & \mathbf{0} \\ \mathbf{0} & \mathbf{B} \end{pmatrix}, \tag{2.33}$$

with

$$\mathbf{V} = \begin{pmatrix} \gamma\mathbf{I} & \mathbf{C} \\ -\mathbf{C}^{+} & \gamma\mathbf{I} \end{pmatrix}. \tag{2.34}$$

$\mathbf{V}$ is symplectic, which demands $\gamma^2 + \|\mathbf{C}\| = 1$, and where $\mathbf{C}$ is a 2×2 matrix and $\mathbf{C}^{+}$ is the symplectic conjugate given by:

$$\mathbf{C}^{+} = \begin{pmatrix} C_{22} & -C_{12} \\ -C_{21} & C_{11} \end{pmatrix}, \tag{2.35}$$

and $\mathbf{V}^{-1}$ is given by:

$$\mathbf{V}^{-1} = \begin{pmatrix} \gamma\mathbf{I} & -\mathbf{C} \\ \mathbf{C}^{+} & \gamma\mathbf{I} \end{pmatrix}. \tag{2.36}$$

$\mathbf{C}$ is a measure of the coupling, and $\mathbf{T}$ is uncoupled if and only if $\mathbf{C} = 0$ [13].

Chapter 3

Fundamental Idea of the Spin Rotator Design

As **Figure 3.1** shows, the spin rotator has two components: the left side rotator (L-Rot) located at 210 m upstream of the interaction point (IP), and the right side rotator (R-Rot) located at 169 m downstream of the IP. When the electron beam travels upstream and passes through the L-Rot, its vertical spin is rotated to some direction in the horizontal plane. After the beam exits the L-Rot, the spin precession continues in the dipole field induced by bending magnets at the region between the L-Rot and the IP, finally reaching the longitudinal direction at the IP. After the electron beam coming out of the IP, the R-Rot rotates the horizontal spin back to the vertical, which remains unchanged in the horizontal bending field. Thus, when the electron undergoes one revolution in the ring and re-enters the L-Rot, its spin is still in the vertical direction and follows the same motion as the previous revolution.

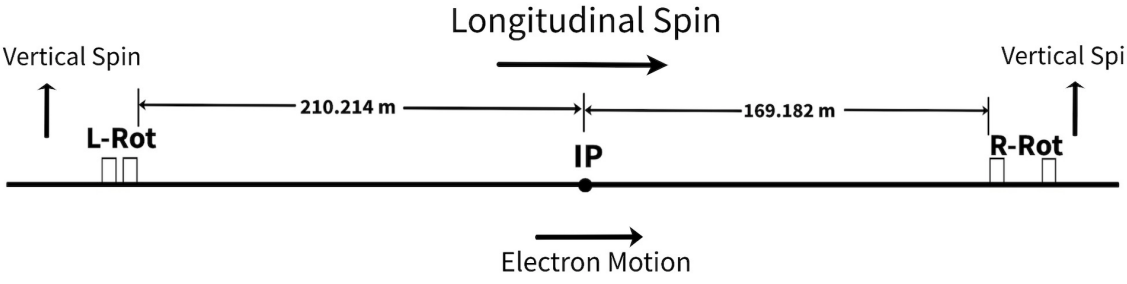

Figure 3.1: Overview of the Spin Rotator Structure

3.1 Spin Rotator Magnet Structure

Uli Wienands at Argonne National Laboratory proposed building the spin rotator with solenoid-dipole-quadrupole combined function magnets. In 2019, Uli Wienands and Ningdong Wang explored the possibility of designing the compact spin rotator with the solenoid-dipole-quadrupole combined function magnets [14]. The basic idea of the design is to replace some existing dipole magnets on both sides of the IP with dipole-solenoid combined function magnets and keep the original dipole strength to preserve the machine geometry. With the additional longitudinal magnetic field provided by the solenoid, the rotator magnet can produce a constant magnetic field in the x-y plane, allowing the spin rotation to happen between the vertical direction and horizontal plane. In addition, there are six skew-quadrupole installed on the top of the dipole-solenoid to compensate for the x-y plane coupling caused by the solenoid [15]. One of the motivations of using the solenoid-dipole combined function magnets is to recover the original machine by turning off the solenoids and the skew-quads in the rotator and minimizing any disruption to the existing.

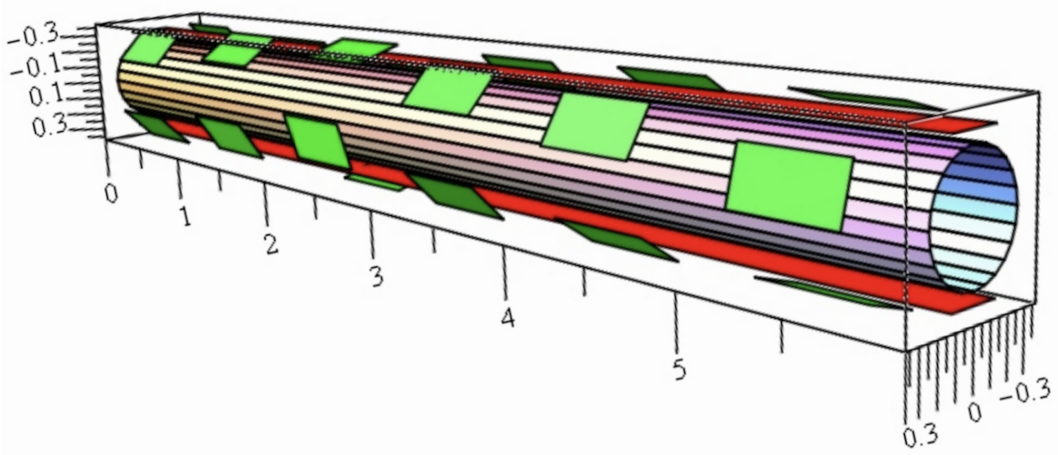

Figure 3.2: Spin Rotator Magnet Structure: two red planes and the blue pipe represents the dipole and solenoid respectively, and they are wrapped by 6 skew-quads which are the green planes.

3.2 Constraints of the Design

The installation of the spin rotator will change the machine dynamics significantly and lead to beam loss, which brings the first constraint to the design, which is to make the spin rotator transparent to the ring. The transparency is achieved by recovering the original beam dynamics downstream of both the L-Rot and the R-Rot. To maintain the original dynamics as much as possible, skew-quads are installed to compensate for the x-y plane coupling, and the ring quads near the Rotator magnets are tuned to rematch the optics at the exit of the tuning area. Due to the complicated magnetic fields induced by rotator magnets and variation of the ring quads strength, the overall machine parameters such as the Tunes and the chromaticities will also be changed; the Tune needs to be maintained as the original, and the Chromaticity is not necessary to be matched to the original as long as it stays in a reasonable range. It can be recovered by tuning the sextupoles, but the more important purpose is to reach the maximum dynamic aperture, which is achieved by tuning the 45 existing focusing (SF*) and defocusing (SD*) sextupole pairs that are not in the rotator region and they are located at four arc sections shown in **Figure 3.3** [16]. To match the Tune, it requires finding a straight section in the High Energy Ring with no bending magnets. In this region, the dispersion function is zero; varying the strength of quadrupoles can match the Tune value without affecting the dispersion. Also, the emittance has to be kept low to maintain the high luminosity.

Another constraint is the technical/physical constraint: all new magnets must be manufacturable and installable. The particle follows a curved motion in the lab frame when passing through bending magnets. It will experience the solenoid-quadrupoles field if the rotator magnet is straight. Thus, the dipole-solenoid-quadrupole combined function magnet must have the same curvature as the reference orbit. Therefore, manufacturing the curved rotator magnet is necessary. Also, all new magnets can not exceed the technical limit. The rotator magnet would use a direct-wind technology following the method described in Reference [17]. The technical limits we impose on the fields at this stage were based on private communications [18] with an understanding that the limits may be refined in the future as actual magnet designs are developed. For the solenoid, the technical limit is 5 T. Another reason for restricting the strength of solenoids is that the strength of skew-quads applied for the decoupling is positively correlated to the solenoid. Therefore, strong solenoids may lead to skew-

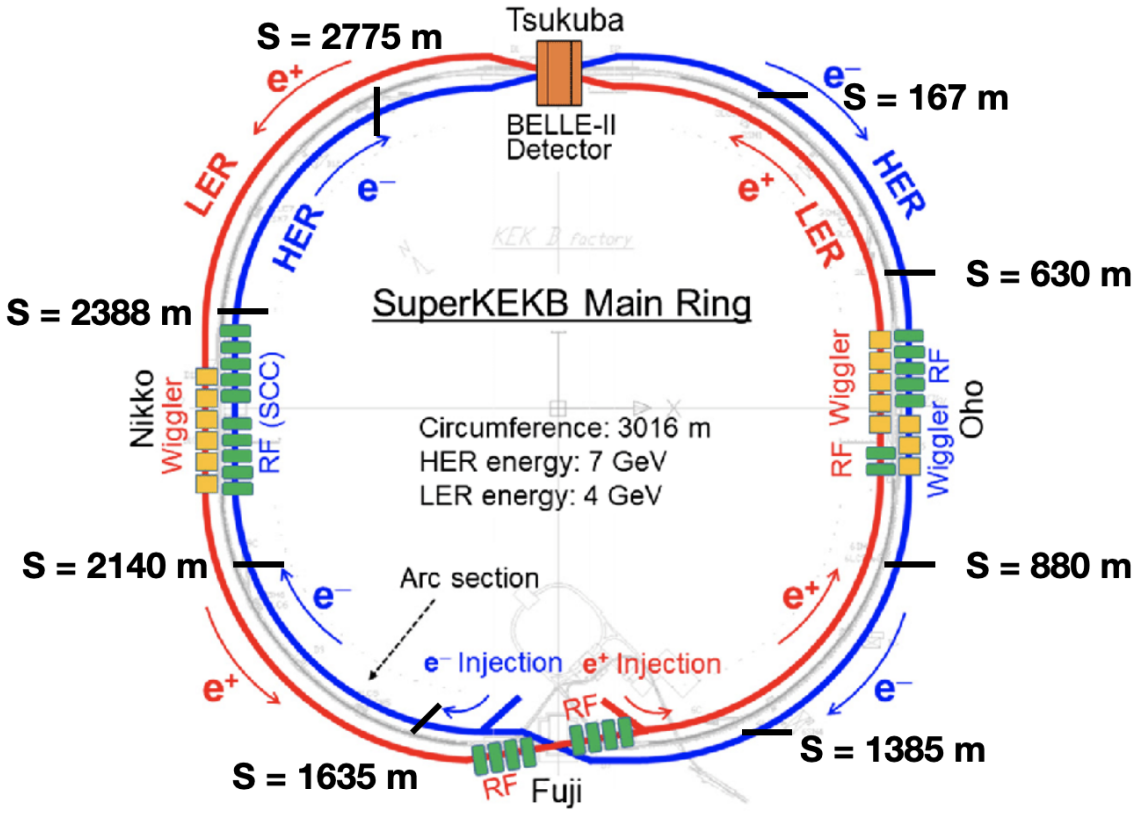

Figure 3.3: The blue ring is the HER or the Electron Ring, SD/SF sextupoles are located at four arc sections between s =167 to 630 m, s = 880 to 1385 m, s = 1635 to 2140m, and s = 2338 to 2775 m

quads exceeding their physical limit. The magnetic strength of skew-quads needs to be limited at 3T at the coil, which corresponds to quadrupole strength of 30 T/m requiring 3 T at r = 10 cm. The pipe has a width of about 20 cm at the location of the spin rotator installation, corresponds to radius r = 10 cm. The technical limit of ring quadrupoles is to be confirmed with the KEK experts. Right now, it is assumed to be the same as the strongest existing quadrupole in the machine, which is about 13 T/m.

3.3 Determine the nominal position for spin rotator installation in the HER

As discussed at the beginning of this chapter, the goal is to have the spin rotating back and forth between the vertical direction and the horizontal plane. We first apply the Thomas BMT Equation to explore the nominal installation position for the spin rotator and to study the spin motion in the rotator by building a "toy model" that does not consider the effects of radiation, fringe fields and etc. Assume there is a specific spin vector $\vec{\hat{S}} = (\hat{S}_x, 0, \hat{S}_z)$ in the horizontal plane that can be rotated to the longitudinal direction at the IP by existing dipoles in between. There are three parameters ($S_x = \hat{S}_x$, $S_y = 0$, $S_z = \hat{S}_z$) to be matched at the exit of L-Rot. Notice that one spin component can be determined by another two because the length of the spin vector is invariant. Thus, to match the spin at the exit, it requires at least two variables (two solenoids), which means at least two ring dipoles have to be replaced with the Rotator magnets for the L/R-Rot. The main principle for designing the rotator is to maintain the original machine dynamics as much as possible, so it needs to minimize the number of ring dipoles that will be replaced. Consider the simplest case that the L-Rot is made of two rotator magnets having the identical dipole-solenoid field and assume it can reach $\vec{\hat{S}}$ at the exit. Give the vertical spin $\vec{S}_0 = (0, 1, 0)$ at the entrance of the L-Rot, plugging it into Eq. 2.28 and 2.30 can determine the spin motion:

$$\begin{cases} S_x = -\frac{\omega_{//}}{\omega} \sin \omega s \\ S_y = \frac{\omega_{//}^2}{\omega^2} \cos \omega s + \frac{\omega_{\perp}^2}{\omega^2} \\ S_z = -\frac{\omega_{//}\omega_{\perp}}{\omega^2} \cos \omega s + \frac{\omega_{//}\omega_{\perp}}{\omega^2} \end{cases} . \tag{3.1}$$

Let L denote the length of the dipole magnets that are going to be replaced, at the exit of L-Rot s = 2L, and $\omega_{\perp}$ can be determined by the known dipole fields. The spin is in the horizontal plane at the exit, $S_y = 0$ gives the equation:

$$\omega_{//}^2 \cos 2\omega L + \omega_{\perp}^2 = 0. \tag{3.2}$$

Eq.3.2 can not be solved analytically but can be solved numerically to determine the desired solenoid strength. Note that it must satisfy $2n\pi + \frac{\pi}{2} \leqslant 2\omega L \leqslant 2n\pi + \frac{3\pi}{2}$ (n $\in \mathbf{N}$) and $|\omega_{//}| \geqslant |\omega_{\perp}|$ to guarantee a solution with the real root. This constraint describes the physical picture that the spin precession trajectory must intersect with the horizontal plane and have the right amount of rotation to reach the intersection points. In addition, the solenoid strength should stay below 5 T due to the technical constraint. Once the desired solenoid strength is found, it is entered into Eq.3.1 to compute $\hat{S}_x$ and $\hat{S}_z$. The place of installation of L-Rot can be determined by investigating the High Energy Ring lattice to find where the spin vector that can reach the longitudinal direction at the IP is close to the ideal spin $(\hat{S}_x, 0, \hat{S}_z)$. The non-identical dipole-solenoid spin rotator can be considered as an adjustment to the identical case. Adjusting the solenoid strength around the ideal value can compensate for the small deviation to the ideal spin $(\hat{S}_x, 0, \hat{S}_z)$. Dipoles that have the exit spin with a large deviation to the ideal spin are not candidates because it requires adjusting the solenoid field significantly to match the exit spin, which may lead to the solenoid strength exceeding 5 T.

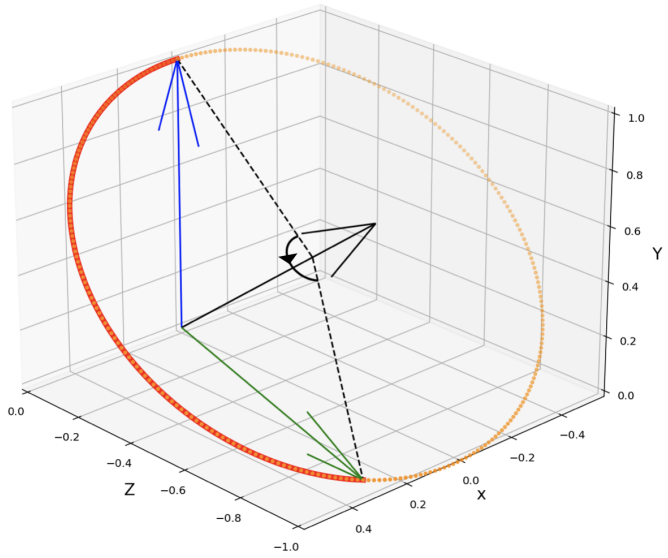

Figure 3.4: The toy model of the L-Rot made of two identical dipole-solenoid combined function magnets : the red curve is the trajectory of the spin vector; the straight black arrow is the rational axis; the blue arrow is the initial spin vector which is vertical; and the green arrow is the exit spin vector, which is in the horizontal plane

Another constraint for choosing the rotator candidate position is to avoid the region where the beta function needs to be maintained as the original, such as the location of SLX and SLY sextupoles shown in **Figure 3.5**. These sextupoles are important to the crab waist, and at their location, the beta function is large; so we avoid changing the lattice elements at this region as doing so can affect the ring dynamics significantly. They are located within 100m on both sides of the IP, which should be avoided. Also, the spin Rotator should be installed as close to the IP as possible. The natural polarization direction in the ring is close to vertical, and the spin motion is more stable if it mostly stays in the vertical direction in the ring. Considering all constraints discussed above, the L-Rot candidate region is decided to be from 120 to 300 m upstream of the IP; the R-Rot candidate region is from 120 to 300 m downstream of the IP.

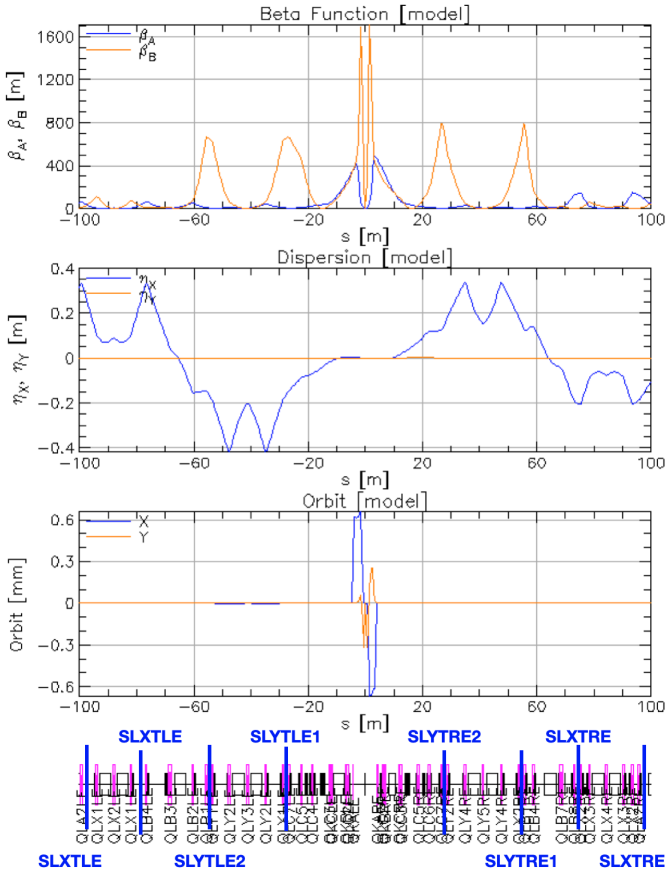

Figure 3.5: Lattice elements near the IP within ± 100 m (output from running BMAD lattice simulation with the electron): SLX and SLY Sextupoles are located at where the x,y component of the beta function reaches peaks, respectively.

As **Table 3.1** shows, there are ten dipoles in the L-Rot candidate region, eight identical B2E with a strength of 0.22075 T and two identical BLA4LE with a strength of 0.26282 T; all have the same length of 5.902m. The constraint of Eq.3.2 indicates that the minimum solenoid strength is 3.73, 4.43 T for B2E and BLA4LE, respectively. For the B2E, the solenoid field is determined to be $B_{//} = \pm 3.90$ T (sign determines the field direction), $\hat{S}_x \simeq \mp 0.29$, $\hat{S}_z \simeq \pm 0.96$; for the BLA4LE, the solenoid field is found to be about ± 4.44 T, $\hat{S}_x \simeq 0$, $\hat{S}_z \simeq \pm 1$, both solenoids have the strength below 5T. The B2E (index 4945) has the exit spin (0.53232, -0.0009246, -0.84654), which is closest to the ideal spin, and the deviation is about 15 degrees; the exit spin (0.17962, -0.00092468, 0.98374) of the BLA4LE (index 5038) is close to computed exit spin, and the deviation is about 10 degrees. Although the B2E has an exit spin with a higher deviation than the BLA4LE, it has a weaker solenoid strength. A priori, it cannot be determined which solution is better, so there exist two candidates for the L-Rot; one is made of two B2E with the index 4939 and 4945, another one is made of two BLA4LE. Due to the deviation of the exit spin, two rotator magnets of the L-Rot will have non-identical solenoid strength.

	index	name	key	s (m)	l (m)	B_field (T)	spin.x	spin.y	spin.z
0	4847	B2E	Sbend	2722.18	5.902	0.22075	-0.96076	-0.00092458	-0.27739
1	4853	B2E	Sbend	2730.43	5.902	0.22075	-0.8223	-0.00092459	0.56905
2	4885	B2E	Sbend	2755.34	5.902	0.22075	-0.078937	-0.00092456	0.99688
3	4907	B2E	Sbend	2772.94	5.902	0.22075	0.72249	-0.00092455	0.69138
4	4939	B2E	Sbend	2797.85	5.902	0.22075	0.99244	-0.0009246	-0.12271
5	4945	B2E	Sbend	2806.1	5.902	0.22075	0.53232	-0.0009246	-0.84654
6	4978	B2E	Sbend	2831.01	5.902	0.22075	-0.31938	-0.00092468	-0.94763
7	5000	B2E	Sbend	2848.61	5.902	0.22075	-0.93614	-0.00092465	-0.35162
8	5032	BLA4LE	Sbend	2872.44	5.902	0.26282	-0.76738	-0.00092464	0.64119
9	5038	BLA4LE	Sbend	2880.68	5.902	0.26282	0.17962	-0.00092468	0.98374

Table 3.1: Table listing the HER dipole elements that were considered to be replaced by L-Rot spin rotators combined function magnets, which is generated from running the BMAD simulation for the electron in the HER lattice. Elements circled by red rectangle have the exit spin which is close to the ideal spin.

	index	name	key	s (m)	l (m)	B_field (T)	spin.x	spin.y	spin.z
0	1596	BLA4RE	Sbend	118.168	5.902	0.19036	0.92763	0.0011425	-0.37351
1	1617	BLA6RE	Sbend	142.221	5.902	0.1986	0.38066	0.0011426	-0.92471
2	1623	BLA6RE	Sbend	150.468	5.902	0.1986	-0.39583	0.0011426	-0.91832
3	1655	B2E	Sbend	175.085	5.902	0.22075	-0.96177	0.0011425	-0.27384
4	1675	B2E	Sbend	192.682	5.902	0.22075	-0.82019	0.0011425	0.57209
5	1707	B2E	Sbend	217.595	5.902	0.22075	-0.075245	0.0011425	0.99716
6	1713	B2E	Sbend	225.842	5.902	0.22075	0.72506	0.0011424	0.68869
7	1743	B2E	Sbend	250.755	5.902	0.22075	0.99198	0.0011425	-0.12642
8	1763	B2E	Sbend	268.352	5.902	0.22075	0.52916	0.0011425	-0.84852
9	1793	B2E	Sbend	293.265	5.902	0.22075	-0.32293	0.0011424	-0.94642

Table 3.2: Table listing the HER dipole elements that were considered to be replaced by R-Rot spin rotators combined function magnets which is generated from running the BMAD simulation for the electron in the HER lattice. Element circled by red rectangle has the exit spin close to the ideal spin

Table 3.2 shows dipole magnets in the R-Rot candidate region, and there are two identical BLA6RE and seven identical B2E. Note BLA4RE is not a candidate, and it appears in the figure because it shows the entrance spin of the BLA6RE. The R-Rot follows the same analyzing process, even though the exit spin needs to reach the vertical, which is opposite to the L-Rot. Eq. 3.1 is still applicable when taking L $\rightarrow$ -L to make the spin vector rotate backward from the exit to the entrance. Notice flipping the sign of L does not change the sign of $\hat{S}_y$ and $\hat{S}_z$, but does change the sign of $\hat{S}_x$. Thus, the computed solenoid field for the B2E is same as the L-Rot with $B_{//} = \pm 3.90$ T, and $\hat{S}_x = \pm 0.29$, and $\hat{S}_z = \pm 0.96$. There are two spots that the spin is close to the computed value. The dipole strength of BLA6RE is close to the B2E, so the ideal spin should be similar to B2E. BLA6RE is not a candidate because the exit spin of the BLA4RE is very different from the ideal spin. For the B2E, the first spot is the exit of BLA6RE (index 1623), and the deviation is about 5 degrees. The second spot is the exit of the B2E (index 1793), but it is about 150m further away from the IP. Thus, the R-Rot only has one candidate, made of two B2E magnets with the index of 1655 and 1675.

Since the candidate positions for both the L-Rot and R-Rot are determined, now we focus on building the toy model for the non-identical case. The solenoid field of the first rotator magnet is denoted as $B_{1//}$, the second rotator magnet as $B_{2//}$, and the dipole field is still $B_{\perp}$. For the L-Rot, the entrance spin is vertical, following Eq.3.1, at the exit of the first L-Rot magnet, the spin vector $\vec{S_1}$ is given by:

$$\begin{cases} S_{1x} = -\frac{\omega_{1//}}{\omega_1} \sin \omega_1 L \\ S_{1y} = \frac{\omega_{1//}^2}{\omega_1^2} \cos \omega_1 L + \frac{\omega_{\perp}^2}{\omega_1^2} \\ S_{1z} = -\frac{\omega_{1//}\omega_{\perp}}{\omega_1^2} \cos \omega_1 L + \frac{\omega_{1//}\omega_{\perp}}{\omega_1^2} \end{cases} . \tag{3.3}$$

The exit spin is also known, and it's denoted as $\vec{S_2} = (S_{2x}, S_{2y}, S_{2z})$, and $S_{2y} \simeq 0$. Taking L$\rightarrow$ -L, the entrance spin of the second rotator magnet or the exit spin of the first rotator magnet can be expressed as :

$$\begin{cases} S_{1x} = A_2 \sin(-\omega_2 L + \phi_2) \\ S_{1y} = -\frac{\omega_{2//}}{\omega_2} A_2 \cos(-\omega_2 L + \phi_2) + \frac{\omega_{\perp}}{\omega_2} C_2 \\ S_{1z} = \frac{\omega_{\perp}}{\omega_2} A_2 \cos(-\omega_2 L + \phi_2) + \frac{\omega_{2//}}{\omega_2} C_2 \end{cases} . \tag{3.4}$$

Since the spin motion at the second rotator magnet runs backward from the exit to the entrance, $\vec{S_2}$ is the initial condition. The constants in Eq.3.4 can be determined as:

$$\begin{cases} C_2 = \frac{\omega_{2//} S_{2z}}{\omega_2} \\ A_2 \cos \phi_2 = \frac{\omega_{\perp} S_{2z}}{\omega_2} \\ A_2 \sin \phi_2 = S_{2x} \end{cases} . \tag{3.5}$$

Substituting Eq.3.5 into Eq.3.4 can find the expression of $\vec{S_1}$ as functions of $\omega_{2//}$:

$$\begin{cases} S_{1x} = S_{2x}\cos\omega_2 L - \frac{\omega_\perp S_{2z}}{\omega_2}\sin\omega_2 L \\ S_{1y} = -\frac{\omega_{2//}}{\omega_2}\left(\frac{\omega_\perp S_{2z}}{\omega_2}\cos\omega_2 L + S_{2x}\sin\omega_2 L\right) + \frac{\omega_{2//}\omega_\perp S_{2z}}{\omega_2^2} \\ S_{1z} = \frac{\omega_\perp}{\omega_2}\left(\frac{\omega_\perp S_{2z}}{\omega_2}\cos\omega_2 L + S_{2x}\sin\omega_2 L\right) + \frac{\omega_{2//}^2 S_{2z}}{\omega_2^2} \end{cases} . \quad (3.6)$$

There are two expressions, Eq.3.3 and Eq.3.6 for $\vec{S_1}$, they should be equivalent to each other.

$$\begin{cases} S_{2x}\cos\omega_2 L - \frac{\omega_\perp S_{2z}}{\omega_2}\sin\omega_2 L = -\frac{\omega_{1//}}{\omega_1}\sin\omega_1 L \\ -\frac{\omega_{2//}}{\omega_2}\left(\frac{\omega_\perp S_{2z}}{\omega_2}\cos\omega_2 L + S_{2x}\sin\omega_2 L\right) + \frac{\omega_{2//}\omega_\perp S_{2z}}{\omega_2^2} = \frac{\omega_{1//}^2}{\omega_1^2}\cos\omega_1 L + \frac{\omega_\perp^2}{\omega_1^2} \\ \frac{\omega_\perp}{\omega_2}\left(\frac{\omega_\perp S_{2z}}{\omega_2}\cos\omega_2 L + S_{2x}\sin\omega_2 L\right) + \frac{\omega_{2//}^2 S_{2z}}{\omega_2^2} = -\frac{\omega_{1//}\omega_\perp}{\omega_1^2}\cos\omega_1 L + \frac{\omega_{1//}\omega_\perp}{\omega_1^2} \end{cases} . \quad (3.7)$$

There are three equations and only two variables because one spin component can be determined by another two. Three equations can be reduced into two by taking the linear combination of any two of them. For example, multiply the second equation by $\omega_\perp$, and the third equation by $\omega_{1//}$, and adding them together can reduce Eq.3.7 into the following form:

$$\begin{cases} S_{2x}\cos\omega_2 L - \frac{\omega_\perp S_{2z}}{\omega_2}\sin\omega_2 L = -\frac{\omega_{1//}}{\omega_1}\sin\omega_1 L \\ \frac{(\omega_{1//}-\omega_{2//})\omega_\perp}{\omega_2}\left(\frac{\omega_\perp S_{2z}}{\omega_2}\cos\omega_2 L + S_{2x}\sin\omega_2 L\right) + \frac{\omega_{2//}\omega_\perp^2 + \omega_{1//}\omega_{2//}^2}{\omega_2^2} S_{2z} = \omega_\perp \end{cases} . \quad (3.8)$$

Again, the non-linear equations can not be solved analytically but can be solved numerically to determine the solenoid strength for the non-identical case. Solving Eq.3.8 can find that $B_{1//} = 5.5669$ T, $B_{2//} = 2.8831$ T if replacing two BLA4LE; $B_{1//} = -2.2275$ T, $B_{2//} = -5.2673$ T for the B2E. Although both candidates have one solenoid exceeding 5T with a non-significant amount, they are still potential candidates because it is only a toy model that does not consider other effects such as fringe fields, radiation, etc. To see a more realistic model, running the BMAD simulation is necessary. If the BMAD simulation still yields a result exceeding 5T,

other models must be considered until an applicable design is determined, such as investigating further upstream area in the ring, replacing three dipoles or more, etc.

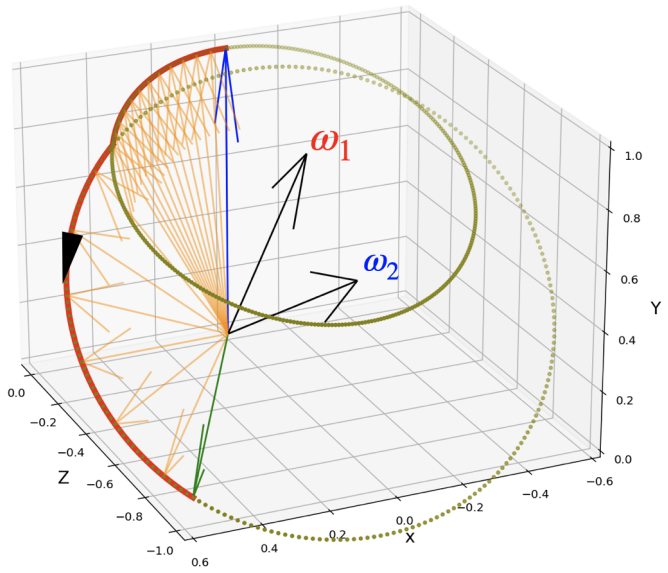

Figure 3.6: The toy model of the B2E L-Rot with non-identical solenoids: the blue arrow is the entrance spin; the green arrow is the exit spin that can reach the longitudinal spin orientation at the IP; two black arrows are the rotational axis of two rotator magnets; red curve is the trajectory of the spin vector

R-Rot follows the same analysis but again needs to take L $\rightarrow$ -L to make it rotate backward from the exit to the entrance, Eq.3.8 becomes:

$$\begin{cases} S_{2x}\cos\omega_2 L + \frac{\omega_\perp S_{2z}}{\omega_2}\sin\omega_2 L = \frac{\omega_{1//}}{\omega_1}\sin\omega_1 L \\ \frac{(\omega_{1//}-\omega_{2//})\omega_\perp}{\omega_2}\left(\frac{\omega_\perp S_{2z}}{\omega_2}\cos\omega_2 L - S_{2x}\sin\omega_2 L\right) + \frac{\omega_{2//}\omega_\perp^2+\omega_{1//}\omega_{2//}^2}{\omega_2^2}S_{2z} = \omega_\perp \end{cases} . \quad (3.9)$$

The R-Rot only has one candidate which is a pair of B2E, solving Eq. 3.9 can determine that $B_{1//} = -3.1649$ T, $B_{2//} = -4.5554$ T, both are below 5 T. Note that the spin rotation in R-Rot is opposite to the L-Rot, so $B_{2//}$ is the solenoid field of the first rotator magnet, $B_{1//}$ is for the second. Now, both the candidate for the L-Rot and R-Rot are determined, the toy model can be used as the initial guess to run BMAD optimization.

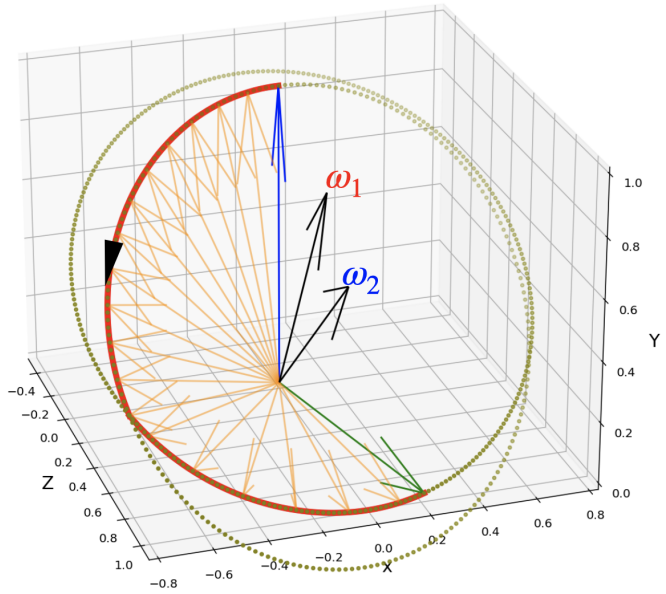

Figure 3.7: The toy model of the BLA4LE L-Rot with non-identical solenoids: the blue arrow is the entrance spin; the green arrow is the exit spin that can reach the longitudinal direction at the IP; two black arrows are the rotational axis of two rotator magnets; red curve is the trajectory of the spin vector

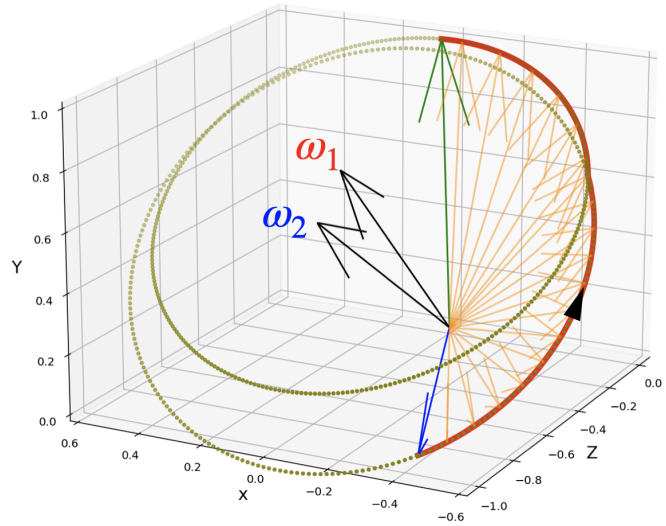

Figure 3.8: The toy model of R-Rot with non-identical solenoids: the blue arrow is the entrance spin which is in the horizontal plane; the green arrow is the exit spin which is in the vertical direction; two black arrows are the rotational axis of two rotator magnets; red curve is the trajectory of the spin vector

Chapter 4

BMAD Simulation

BMAD is an open-source, subroutine library created/maintained by David Sagan at Cornell University for simulating charged particles and X-rays [19]. Étienne Forest's "Polymorphic Tracking Code" (PTC) is incorporated into it. In addition, Tao, a user-friendly interface to BMAD, is developed to give general-purpose simulation based upon BMAD. BMAD via the Tao interface is a powerful tool used to view lattices, do Twiss and orbit calculations, and perform non-linear optimization on lattices.

The algorithm applied to perform the optimization in this project is the Lmdif [20], an optimizer based upon the Levenberg-Marquardt algorithm to minimize the merit function. The general form of merit function $\mathcal{M}$ in Tao is given by [20]:

$$\mathcal{M} \equiv \sum_i \omega_i [\delta D_i]^2 + \sum_j \omega_j [\delta V_j]^2, \tag{4.1}$$

where the δD_i and δV_j are functions of the data and variables, depending on the setting of merit type; ω_i and ω_j are weights that are specified in the fitter and can not be a negative value when using the Lmdif.

SAD, a computer program complex for accelerator design, has been developed in KEK since 1986 [21]. The BMAD lattice file of the SuperKEKB High Energy Ring (HER) is initially translated from SAD [22], in which the particle type is not defined; the simulation particle is a positron by default. The SAD lattice of HER is viewed downwardly in KEK frame, which the electron follows a counterclockwise motion equivalent to positron traveling clockwise in the HER.

4.1 BMAD Elements

4.1.1 Multipole Representation in BMAD

The normalized integrated multipole k_nL is used to specify magnetic multipole components [13], which is equivalent to k_n in SAD.

$$k_nL = \frac{qLB_n}{p_0}, \tag{4.2}$$

where q is the charge, L is the length of the magnetic multipole, p_0 is the reference momentum of the particle, B_n is the field of the magnetic multipole. For example, k_1 is the strength of the quadrupole and B_1 is corresponding magnetic field gradient. A useful approximation can be taken. The momentum of the electron in the HER is about 7 GeV/c, plugging it into the equation above can find that $k_n \simeq \frac{3}{70}B_n$ or $B_n \simeq \frac{70}{3}k_n$.

Another representation that BMAD uses is to divide the field into the normal component b_n and the skew a_n, and the expression for the nth order multipole is given by [13]:

$$\frac{qL}{p_0}(B_y + iB_x) = (b_n + ia_n)(x + iy)^n. \tag{4.3}$$

If there is no skew component, b_n is given by:

$$b_n = \frac{k_nL}{n!}. \tag{4.4}$$

In particular, b_2 is used to represent the integrated strength of the sextupole in BMAD simuation for this project, which is equivalent to $\frac{k_2L}{2}$.

4.1.2 Coordinate System

As it shows in **Figure 4.1** [13], three coordinate systems are used in BMAD to describe the positioning of the lattice elements:

The global coordinate, also called floor coordinate, is a Cartesian coordinate system denoted by (X, Y, Z) and independent of the accelerator. It can be used to describe the building where the machine is located. Usually, Y-axis is taken to point vertically up, and (X, Z) is the horizontal plane. However, in our case, Y-axis is aligned with the direction of the horizontal bending field in the HER, which points downward in the KEK frame.

The local coordinate, also called laboratory and reference coordinate, is denoted by (x, y, z), which is a Cartesian coordinate in the co-moving frame as mentioned in **Section 2.1.1**. The y-axis points the vertical direction, and (x, z) is the horizontal plane with z aligned with the longitudinal direction. It is useful when tracking the beam position in the machine.

The element body coordinate is used for describing the actual position of the elements which are shifted from the nominal position. If there is no shift to the nominal position, it is the same as the local coordinate.

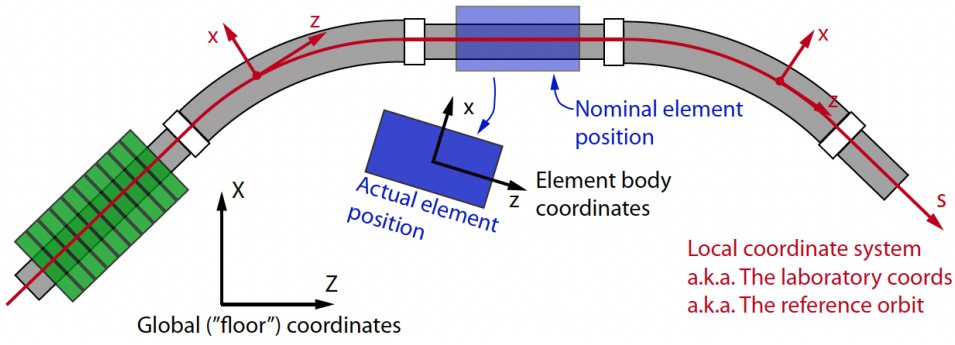

Figure 4.1: The three coordinate systems used by BMAD: The global (or "floor") coordinate system is independent of the accelerator. The local curvilinear coordinate system follows the bends of the accelerator. Each lattice element has element body coordinates which, if the element is not "misaligned" is the same as the local coordinates. The x = y = 0 curved line of the laboratory coordinate system is known as the "reference orbit".

As **Figure 4.2** [13] shows, for a given s-position on the reference orbit, there are 6 parameters applied to describe the local coordinate system with respect to the global coordinate system:

(X,Y,Z) global position or floor

θ azimuth angle in the (X, Z) plane

ϕ elevation angle

ψ roll angle

At the beginning of the lattice (s = 0), the local coordinate system (x, y, z) is set to be aligned with global coordinate (X, Y, Z), and θ, ϕ, ψ to be zero by default. If a machine lies on the horizontal plane, $\phi(s)$, $\psi(s) = 0$ for all s. The HER satisfies this condition, and the coordinate transformation is given by:

$$\begin{pmatrix} x \\ y \\ z \end{pmatrix} = \begin{pmatrix} \cos\theta & 0 & \sin\theta \\ 0 & 1 & 0 \\ -\sin\theta & 0 & \cos\theta \end{pmatrix} \begin{pmatrix} X \\ Y \\ Z \end{pmatrix} . \tag{4.5}$$

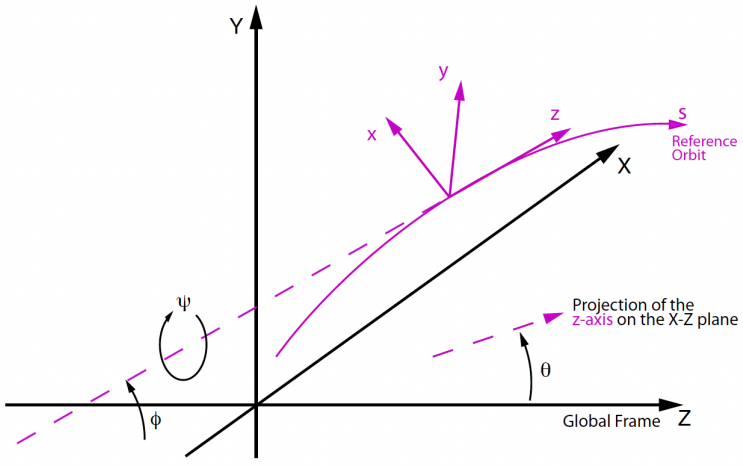

Figure 4.2: The reference coordinate system (purple), which is a function of s along the reference orbit, is described in the global coordinate system (black) by a position (X(s); Y (s); Z(s)) and and by angles $\theta(s)$, $\phi(s)$, and $\psi(s)$.

4.1.3 Element Geometry Types

Figure 4.3 [23] shows three different geometry types that BMAD uses to simulate the lattice element which are related to the rotator modelling with BMAD.

The straight geometry is used to describe the elements, such as the quadrupoles and the drifts. The orientation of local coordinate (x, y, z) does not change, and reference orbit is a straight line.

The bend geometry is used with sbend and rbend dipole elements. Sbend is a sector magnet which has a curvature, and rbend is a rectangular bending magnet. The reference orbit follows a curved trajectory in the global coordinate. The local coordinate (x, y, z) rotates about an axis which is perpendicular to the z-axis.

The patch geometry is used with patch and floor_shift elements. With the patch geometry, the exit coordinates can be arbitrary shifted from the entrance. Patch elements are applied to shift the reference orbit, which affects the downstream elements. The original of the exit is coordinates is translated by (x_offset, y_offset, z_offset). (x_pitch, y_pitch) are applied to rotate the axis of the exit coordinates.

A machine with a **closed-geometry** is like a circular machine such as the storage ring where the particle beam recirculates through the machine. A machine with an **open-geometry** is similar to a linear accelerator (Linac) [13].

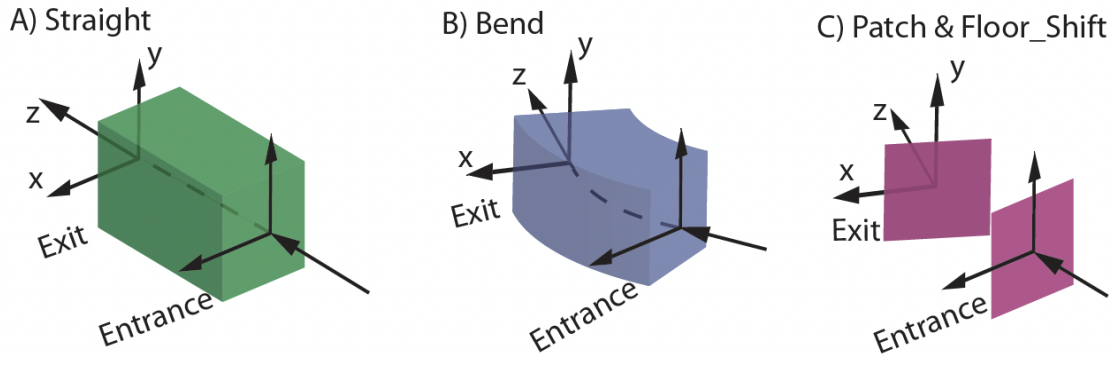

Figure 4.3: Lattice element geometry types: **Straight**, **Bend**, and **Patch**. All elements have an entrance coordinate system and an exit coordinate system.

4.2 Spin Rotator Magnet Modelling in BMAD

To run the BMAD simulation, we first need to model the rotator magnet with the BMAD elements. As mentioned in **Section 3.1**, the Rotator magnet comprises dipole-solenoid combined function magnets with skew-quads on the top. Thus, the modelling must contain a dipole-solenoid-quadrupole element. BMAD has the solenoid-quadrupole (Sol_Quad) element but does not have a dipole-solenoid-quadrupole element because the solenoid-quadrupole is a straight element, but the dipole (sbend) is a curved element. Following David Sagan's idea [24], we replace the dipole with a series of horizontal kicks ("hkicks") to approximate and model the dipole. The hkick is a straight element, and the Sol_Quad has an attribute of hkick. To preserve the original machine geometry, the strength and length of the hkick are initially set to be the same as the Sbends that will be replaced. However, there is still a problem to be addressed. As a straight element, the hkick has a different reference frame from the Sbend. As **Figure 4.4** shows, the horizontal orbit in the hkick with the same length and strength is different from the Sbend due to the observation from different frames.

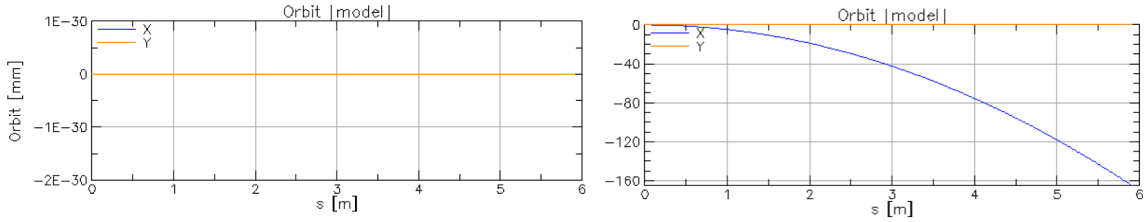

Figure 4.4: Comparison of the orbit: left shows the orbit in the Sbend; right shows orbit in the hkick

The reference orbit passes through the centre of every element, which is equivalent to the machine geometry. To keep the particle orbit on track and preserve the machine geometry, the hkick-sol-quad must be sliced into small pieces and introduce patch elements to shift the reference orbit. The hkick is initially sliced into 6 pieces called the stand-alone model to match the number of the skew-quads. Since the Sbend only bends the particle horizontally, only the horizontal geometry needs to be recovered. Patch elements (xoffset, xpitch, zoffset) are introduced to shift horizontal orbit the exit of each piece.

4.2.1 Validating the Hkick Simulation

Before running optimization for the solenoid-quad, the validity of simulating Sbend with hkick must be examined. This simulation begins with recovering the geometry of the Sbend, which is described by floor coordinate. **Table 4.1** shows the floor coordinate of the entrance and the exit of the original B2E. In order to know the floor coordinate at the exit of each hkick piece, the B2E is also equally sliced into six pieces, and the floor data is given in **Table 4.2**. The exit floor of the six sliced B2E is the same as the original, so it can be used as the optimization target when matching the reference orbit of B2E.

Index	name	key	s	l	floor.x	floor.y	floor.z	floor.theta	floor.phi	floor.psi
0	BEGINNING	Beginning_Ele	0.000	---	0.0000000000	0.0	0.0000000000	0.000000000	0.0	0.0
1	B2E	Sbend	5.902	5.902	-0.1644598229	0.0	5.8991458705	-0.055742726	0.0	0.0
2	END	Marker	5.902	0.000	-0.1644598229	0.0	5.8991458705	-0.055742726	0.0	0.0

Table 4.1: Floor coordinate of the orginal B2E: floor.x, floor.z is the horizontal floor; floor.y is the vertical floor

Index	name	key	s	l	floor.x	floor.y	floor.z	floor.theta	floor.phi	floor.psi
0	BEGINNING	Beginning_Ele	0.000	---	0.0000000000	0.0	0.0000000000	0.0000000000	0.0	0.0
1	B2E	Sbend	0.984	0.984	-0.0045694786	0.0	0.9836861824	-0.0092904543	0.0	0.0
2	B2E	Sbend	1.967	0.984	-0.0182775202	0.0	1.9672874611	-0.0185809087	0.0	0.0
3	B2E	Sbend	2.951	0.984	-0.0411229414	0.0	2.9507189393	-0.0278713630	0.0	0.0
4	B2E	Sbend	3.935	0.984	-0.0731037705	0.0	3.9338957353	-0.0371618173	0.0	0.0
5	B2E	Sbend	4.919	0.984	-0.1142172472	0.0	4.9167329893	-0.0464522716	0.0	0.0
6	B2E	Sbend	5.902	0.984	-0.1644598229	0.0	5.8991458705	-0.0557427260	0.0	0.0
7	END	Marker	5.902	0.000	-0.1644598229	0.0	5.8991458705	-0.0557427260	0.0	0.0

Table 4.2: Floor coordinate of the 6-sliced B2E: floor.x, floor.z is the horizontal floor; floor.y is the vertical floor

We fit patch elements to match the floor coordinate to ten decimal places and slightly vary the strength of each hkick segment to keep the horizontal orbit at zero at the exit of every second piece because the horizontal orbit has two parameters(x, x') requiring two variables to do the fit. **Figure 4.5** shows the geometry of the B2E and the hkick with the floor matched as the original. In **Figure 4.6**, it can be seen that the optics matched to the original, and the particle orbit is also on track. The

sawtooth shape orbit excursion is not physical; it is an artificial effect. When a particle passes through each segment of the hkick, it is not in the co-moving frame, but once it reaches the exit, patch elements shift it back to the co-moving frame.

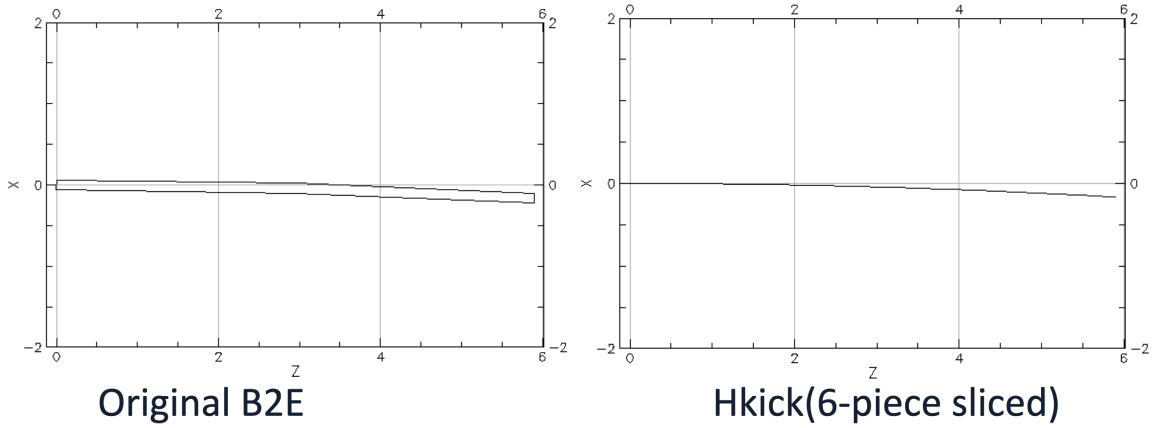

Figure 4.5: Comparison of the geometry between the B2E and the 6-sliced hkick

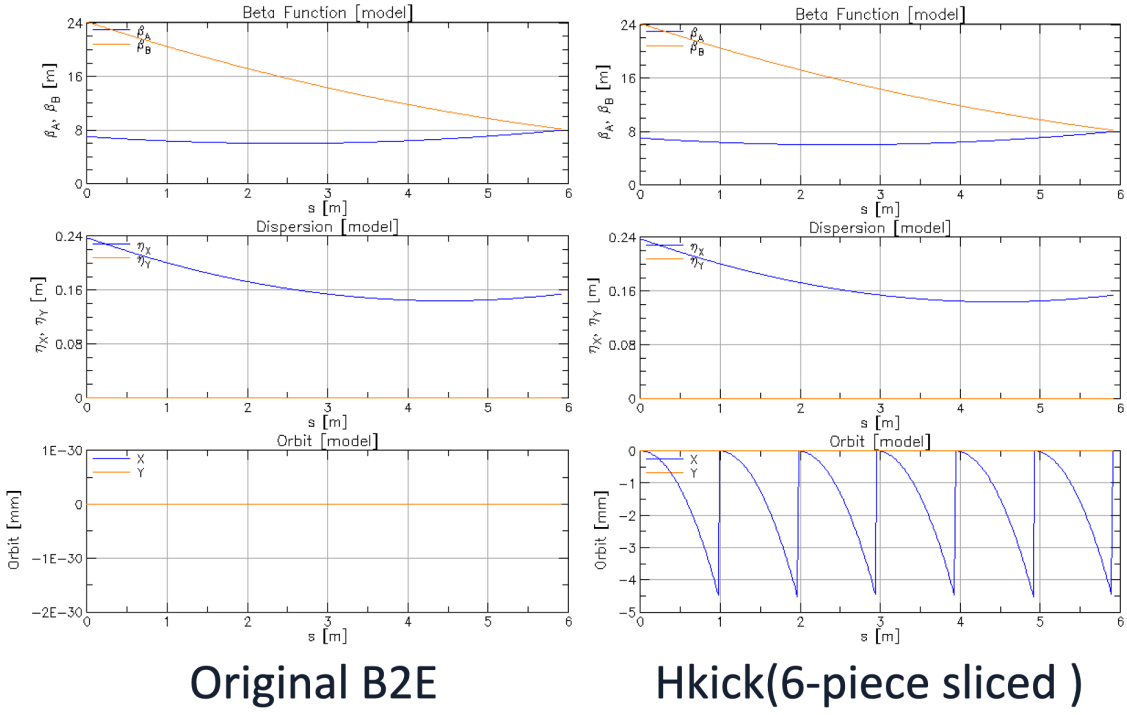

Figure 4.6: Comparison of Beta functions, dispersion and the orbit between the B2E and the 6-sliced hkick, note that the saw-tooth pattern is an artifact of using the hkick model of the dipole.

The spin motion in the hkick also needs to be examined. Given the same arbitrary non-vertical initial spin at the entrance of B2E and the hkick, check if they have the same exit spin. As **Table 4.3** shows, the deviation of the horizontal exit spin happens at the 10th decimal place, so the effect of the artificial orbit excursion on the spin motion is negligible.

Element	position	spin.x	spin.y	spin.z
B2E	entrance	0.5321165994	-0.0009243602	-0.8466705795
	exit	0.9924121470	-0.0009243602	-0.1229523323
Hkick	entrance	0.5321165994	-0.0009243602	-0.8466705795
	exit	0.9924121471	-0.0009243602	-0.1229523319

Table 4.3: Comparison the spin of the B2E and the 6-piece sliced hkick

To see the behaviour of the hkick in the High Energy Ring, replace all Rotator candidate Sbends with 6-piece sliced hkick in the High Energy Ring and check the floor, optics, and the orbit. **Figure 4.7** shows the overall ring geometry, only floor.z has a deviation at the 10th decimal place, and all the rest floor quantities are the same; **Figure 4.8** shows the comparison of the optics and the orbit, and they are identical except for the non-physical orbit excursion; As **Table 4.4** shows, the ring parameters are well maintained after replacing the Sbends with the hkicks. All these comparisons agree that the simulation of Sbend with hkick is quite successful.

Index	name	key	s	l	floor.x	floor.y	floor.z	floor.theta	floor.phi	floor.psi
0	BEGINNING	Beginning_Ele	0.000	---	0.0	0.0	0.0000000000	0.0000000000	0.0	0.0
6650	END	Marker	3016.315	0.000	0.0	0.0	-0.0000000055	-6.2831853072	0.0	0.0

Original Ring

Index	name	key	s	l	floor.x	floor.y	floor.z	floor.theta	floor.phi	floor.psi
0	BEGINNING	Beginning_Ele	0.000	---	0.0	0.0	0.0000000000	0.0000000000	0.0	0.0
6694	END	Marker	3016.315	0.000	0.0	0.0	-0.0000000056	-6.2831853072	0.0	0.0

6-piece sliced Hkick

Figure 4.7: Comparison of the floor coordinate between the original ring and the 6-piece sliced hkick

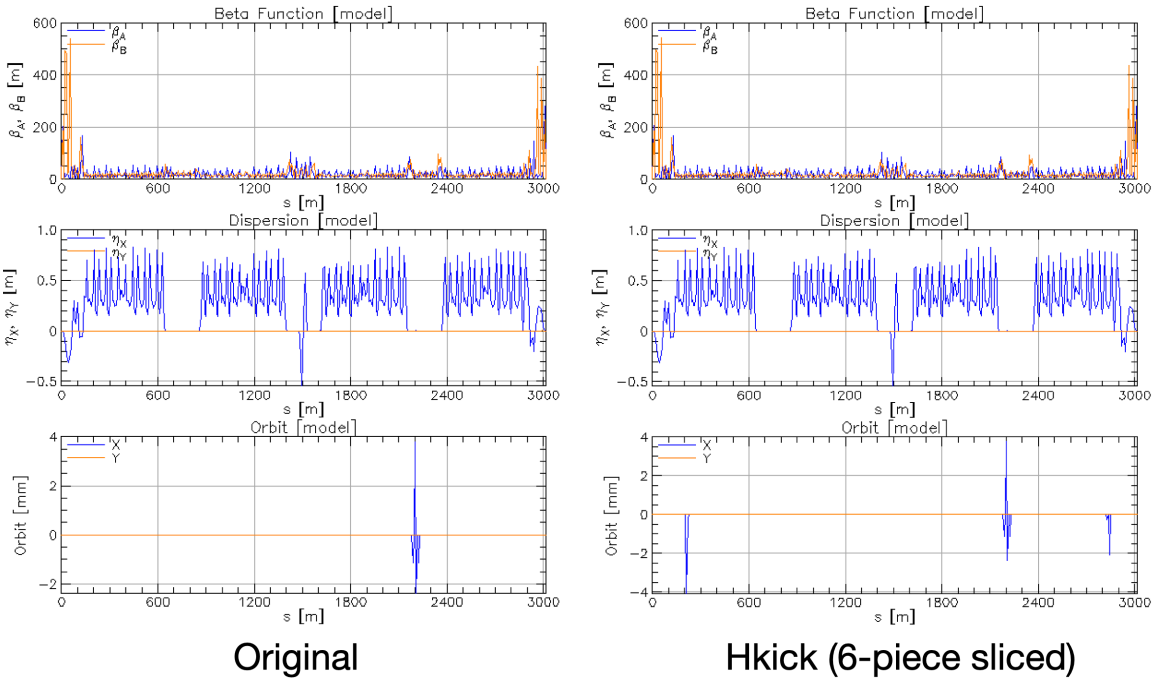

Figure 4.8: Comparison of Beta functions, dispersion and the orbit between the original ring and Rot candidate replaced with 6-piece sliced hkicks. Note that the orbit excursion at s $\sim$ 2200m is associated with the 'wiggler' element in the HER, and the excursions in the hkick version are artifacts of the approach taken to model dipoles with hkicks.

Machine parameter	Original Ring	6-piece sliced hkick
Tune Q_x	45.530994	45.531139
Tune Q_y	43.580709	43.578638
Chromaticity ξ_x	1.593508	1.575556
Chromaticity ξ_y	1.622865	1.658182
Damping partition J_x	1.000064	0.999940
Damping partition J_y	1.000002	1.000002
Emittance ε_x (m)	4.44061×10^{-9}	4.43884×10^{-9}
Emittance ε_y (m)	5.65367×10^{-13}	5.70308×10^{-13}

Table 4.4: Comparison the ring parameters of the original ring and the 6-piece sliced hkick

4.2.2 Slice Model

Due to the non-physical orbit excursion, the simulation particle experiences the sol-quad field when passing through the rotator magnet. The dipole field strength of the quadrupole is proportional to the transverse displacement of the particle with respect to the reference orbit. Thus, a large orbit excursion could significantly affect the particle orbit in the simulation. To minimize the effect of the artificial orbit excursion, we slice each piece of the stand-alone model (6-piece hkick) into 16 pieces, 96 in total. The slice model has six major components associated with 16 minor pieces sharing the same hkick-quad field, and all 96 pieces have the same solenoid field. Also, due to transverse coupling and the orbit excursion, particles following the ideal orbit gain extra vertical motion when passing through the rotator. Following David Sagan's idea [24], this problem is addressed by introducing the vertical kick (vkick) to control the vertical motion of the particle. Note that the use of vkick is only for the BMAD simulation; the real rotator magnet does not have this element. Each sol-quad can only have one attribute of vkick; using six vkicks can control the vertical motion at three spots because the vertical orbit also has two parameters (y, y'). As with the horizontal motion, the vertical orbit is matched to be zero at the exit of every second major section of the rotator model. Summarizing the information above, the rotator modelling is made of six sol-quad associated with hkicks and vkicks, and each section is sliced into 16 pieces.

Before running the optimization for the solenoid, we apply the slice model to the hkick with the sol-quad field off to see how much the orbit excursion can be reduced. Then, refit the patch elements to match the floor coordinate and the orbit. Once the patch elements of the slice model are determined, they are no longer touched in future optimization. As **Figure 4.9** shows, applying the slice model can significantly reduce the orbit excursion; the amplitude of the orbit excursion is reduced to 0.4 percent level of the stand-alone model. Increasing the number of slicing can further reduce the orbit excursion but make the simulation more computationally expensive, so we need to compromise precision and efficiency. It turned out that 96 is approximately the maximum number to guarantee efficiency; going higher leads to difficulty running the optimization.

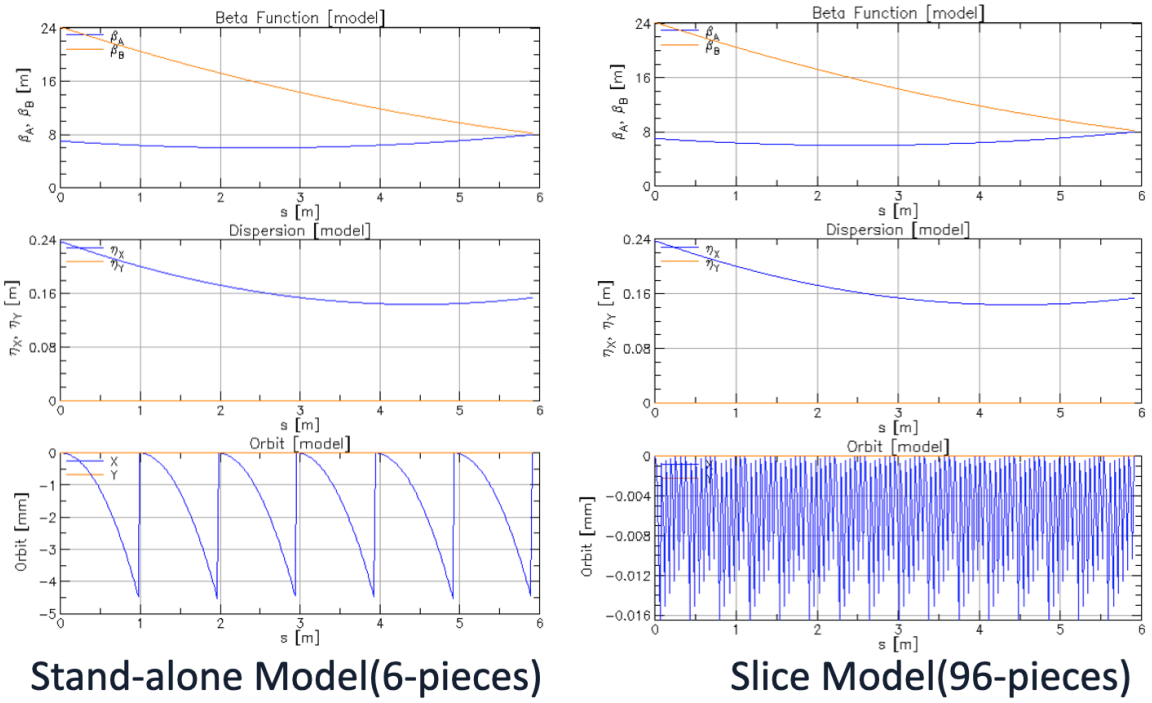

Figure 4.9: Comparison of stand-alone model and slice model applied to the hkick

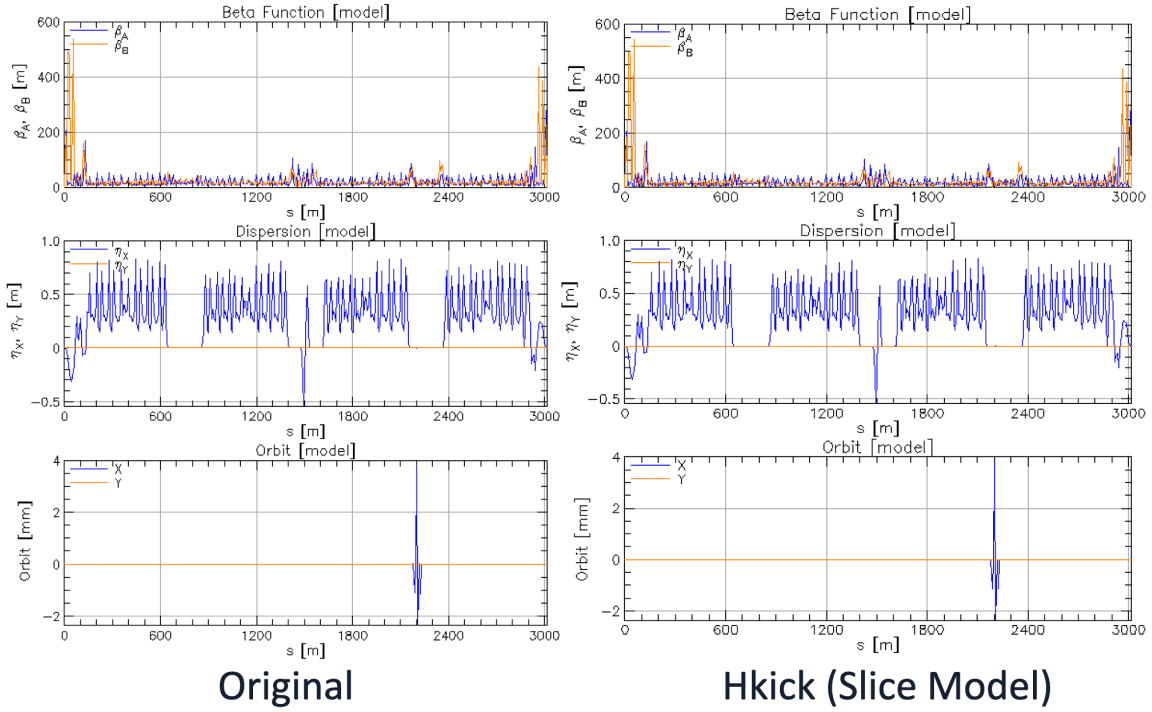

Figure 4.10: Rot candidates replaced by hkicks(slice model) in the full lattice

4.3 Solenoid Optimization

In the previous section, the slice model for the dipole magnet has been established. This enables us to add the solenoid field. As discussed in **Section 3.3**, there are two rotator candidates for the L-Rot; they are a pair of B2E and a pair of BLA4LE. As mentioned at the beginning of this chapter, the simulation is run by the positron rather than for the electron, which we actually have in the HER. With the positron direction reverse to that of the electron in the HER, so the L-Rot in the positron simulation is located downstream of the IP and needs to rotate the horizontal spin to the vertical direction. The fit of the solenoid field is performed in the open-geometry lattice segment shown in **4.12**, which contains the L-Rot candidate Sbends and other lattice elements in between. We replace the candidate Sbends with hkicks and turn on solenoids with quadrupole field off. The High Energy Ring lattice begins at the IP and also ends at the IP. Set the initial spin of the lattice to be longitudinal, and run the open-geometry lattice simulation shown in **Figure 4.11** with BMAD to gain the entrance spin of the L-Rot candidate by looking at the exit of the upstream element.

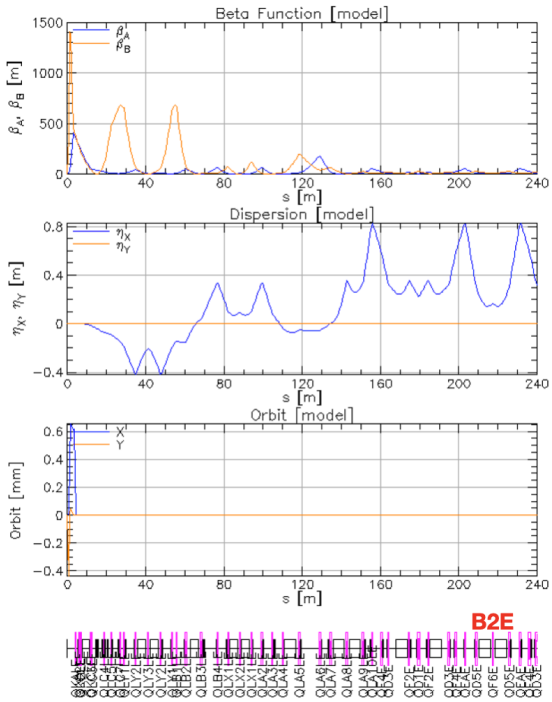

Figure 4.11: The region in the full lattice which contains the IP and the B2E pair, and elements in between

For the B2E, the entrance spin is (0.53215, -0.00092436, -0.84667); The entrance spin of the BLA4LE is (0.17992, -0.00092446, 0.98368). Use the solenoid field in the Toy model as the initial guess, and if the solenoid strength in the Toy model exceeds 5 T, set initial guess to be -4.9 T. We impose the following constraint in the fit: set the max solenoid strength to be 5 T equivalent to $k_s \simeq 0.214\ m^{-1}$. It turned out the pair of BLA4LE can not be replaced for installing the L-Rot. No solution satisfies the constraint that two solenoids stay below 5T, and the spin reaches the vertical direction at the exit. Without adding the 5 T limit in the fitter, can find the solenoid strength are $k_s = 0.29445\ m^{-1}$, -0.029988 m^{-1} equivalent to $B_s = 6.882$ T, -0.701 T. Instead, we replace the B2E pair with the Rotator magnets and name the first rotator magnet of the L-Rot as "B2EALSQ" and the second as "B2EBLSQ". We then fit the solenoids to restore the vertical spin at the exit of the L-Rot. As it shows in **Table 4.5**, the solenoid fields are determined to be k_s = -0.20720 m^{-1}, -0.11027 m^{-1}, equivalent to $B_s = -4.843$ T, -2.578 T, both are below 5 T.

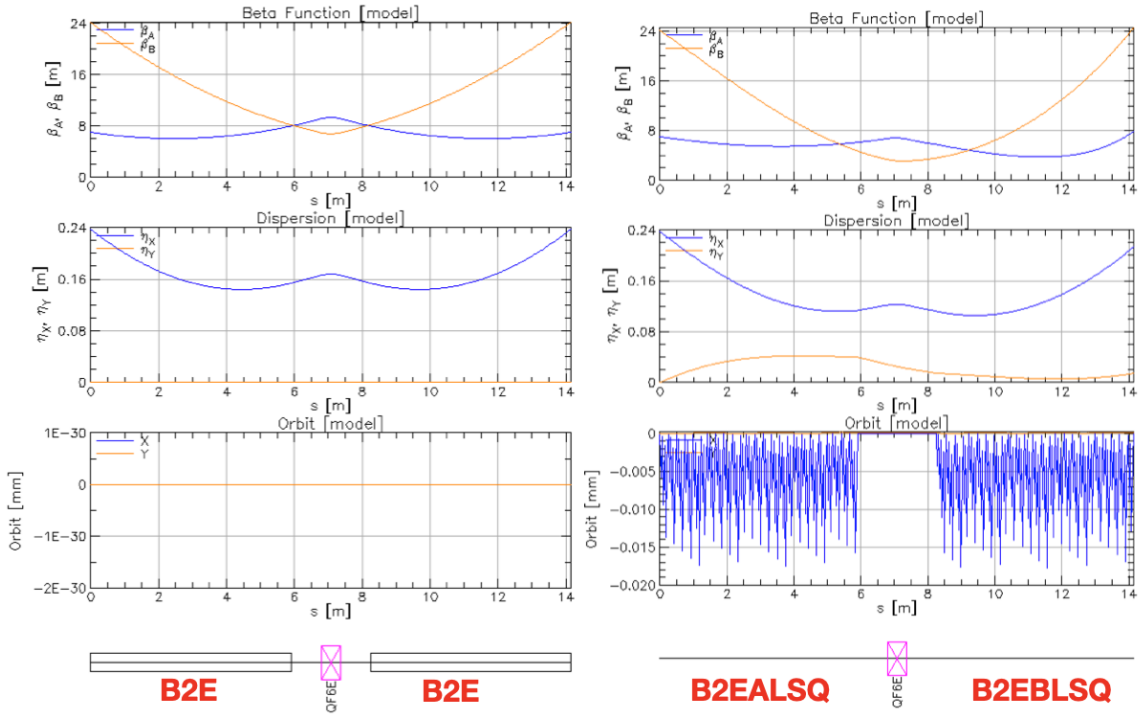

Figure 4.12: Comparison of lattice segment before and after installing the L-Rot with the solenoid on and the quadrupole off; the orbit excursion is the artificial effect of the using the hkick and patch

Rotator Manget	Toy Model	BMAD
B2EALSQ	-5.2672 T	-4.8431 T
B2EBLSQ	-2.2275 T	-2.5774 T
BLA4LEASQ	5.5669 T	6.8824 T
BLA4LEBSQ	2.8831 T	-0.70094 T

Table 4.5: Comparison of the solenoid field of between the Toy model and the BMAD model for the L-Rot; the BLA4LE pairs are not to be replaced with the L-Rot due to the solenoid strength exceeding 5 T; the naming of the rotator magnet follows: the dipole name "B2E","A", "B" to distinguish the dipole pairs, "L" for the L-Rot, and "SQ" is the solenoid-quadrupole

When simulating with the positron, the L-Rot rotates the vertical spin to the horizontal plane at the exit that can reach the longitudinal direction at the IP. It follows the same fitting procedure as the L-Rot. The only difference is that the R-Rot is located upstream of the IP as shown in **Figure 4.13**, we cannot acquire the exit spin of the R-Rot candidate by setting the initial spin to be longitudinal. In order to know the exit spin, we need to fit the initial spin in the open-geometry full lattice simulation to match the longitudinal spin at the end. We perform the optimization and set the optimized spin to be the initial spin, the exit spin of the R-Rot candidate can be determined by looking directly at the exit of the second B2E. The exit spin of the R-Rot candidate is determined to be (-0.39583, 0.0011466, -0.91832). We next replace the B2E candidates with the rotator model, and name the first rotator magnet in the R-Rot as "B2EARSQ", the second as "B2EBRSQ", as it shows in **Figure 4.14**. Use the exit spin as the fitting target and solenoid fields for the R-Rot are determined to be k_s = -0.15438 m^{-1}, -0.16865 m^{-1}, equivalent to $B_s = -3.608$ T, -3.942 T, both are also below 5 T, as shown in **Table 4.6**.

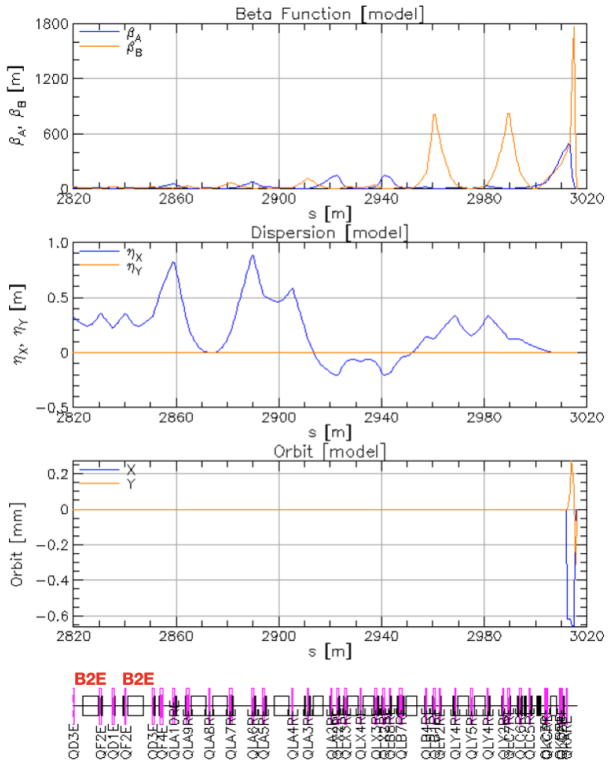

Figure 4.13: The region in the full Lattice contains the R-Rot candidate and the IP, and the elements in between

Rotator Manget	Toy Model	BMAD
B2EARSQ	-3.1649 T	-3.6084 T
B2EBRSQ	-4.5554 T	-3.9420 T

Table 4.6: Comparison of the solenoid fields between the Toy model and the BMAD model for the R-Rot, the naming of the rotator magnet follows: the dipole name "B2E", "A", "B" to distinguish the dipole pairs, "R" for the L-Rot, and "SQ" is the solenoid-quadrupole

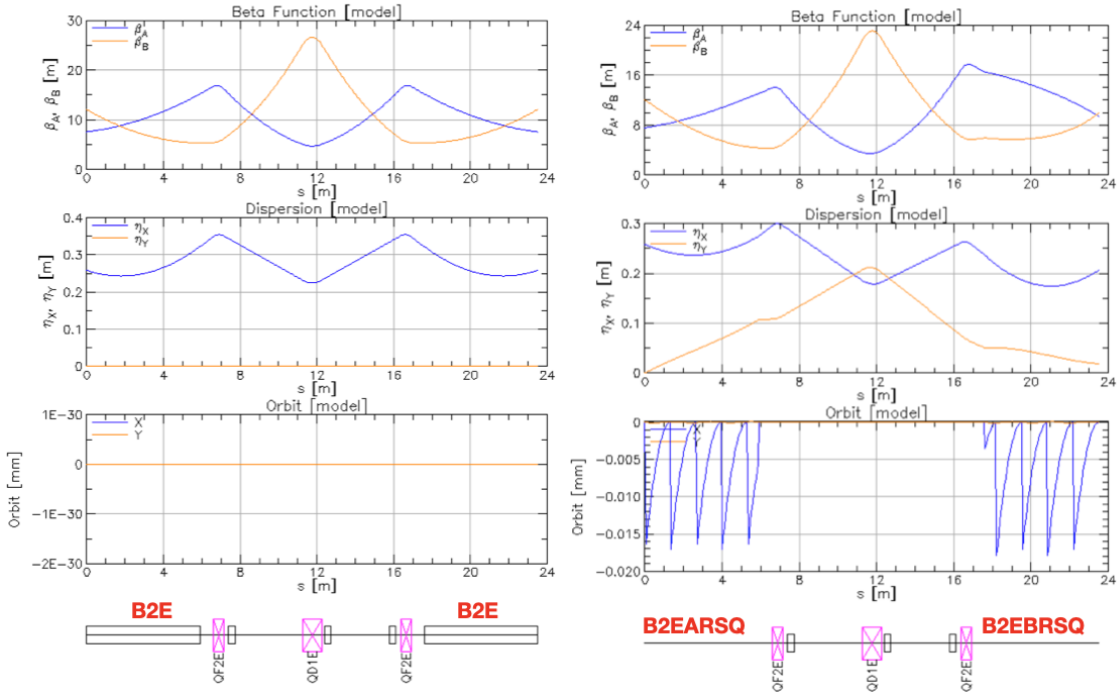

Figure 4.14: Comparison of lattice segment before and after installing the R-Rot with solenoid on and quadrupole off; the orbit excursion is the artificial effect of the using the hkick and patch

4.4 Skew-Quads Optimization

The optimization target for achieving the decoupling is to make the **C** matrix mentioned in **Section 2.3** to be zero at the exit of each rotator magnet. This procedure is performed by taking out the lattice segment for each rotator magnet and running the optimization individually. The skew-quad strength can not exceed 30 T/m, or $k_1 \simeq 1.29\ m^{-2}$ due to the technical constraint. Start with the arbitrary strength k_1 between -1 and 1, and tilt between $-\pi$ to π. In addition,add constraints to quadrupole strength $-1.29 \leqslant k_1 \leqslant 1.29$, and the tilting angle $-\pi \leqslant \text{tilt} \leqslant \pi$ in the optimizer. Only seeking a decoupling solution is not sufficient, it is necessary to consider the impact on the machine dynamics due to the installation of strong skew-quads. The stronger the skew-quad field is, the more it changes local optics, which leads to difficulty proceeding with the optical rematch. Thus, the skew-quad strength needs to be lowered as much as possible. It is achieved by iterating the optimization process manually. The basic idea is to lower the limit of the quadrupole strength gradually. It follows: run the first optimization, manually lower the optimization result below the new limit, and use it as the initial guess running for the next optimization. Do the iteration until the skew-quads strength can not be further lowered. For the L-Rot, the maxim quadrupole strength k_1 of the first and the second rotator magnet is about 0.8, $0.5m^{-2}$, respectively; for the R-Rot, the max of both magnets is about $0.6m^{-2}$.

Furthermore, it is necessary to control the behaviour of the beta function in the rotator region, and this is achieved by adding extra constraints on the beta function at the exit of each rotator magnet. The final step is to put individual rotator magnets back together to observe the behaviour of the beta function in the L/R-Rot and nearby region. If the beta function rapidly increases and reaches a large value in a short-range, the skew-quads need to be adjusted. Usually, it happens at the drift regions nearby the exit of the rotator magnets, and this problem is addressed by adding a limit to the beta function at these drift regions. **Figure 4.15**, **Figure 4.16** show the optics and orbit of the L-Rot and R-Rot lattice after the decoupling is accomplished. Beta functions are well behaved even though they are much higher than the original.

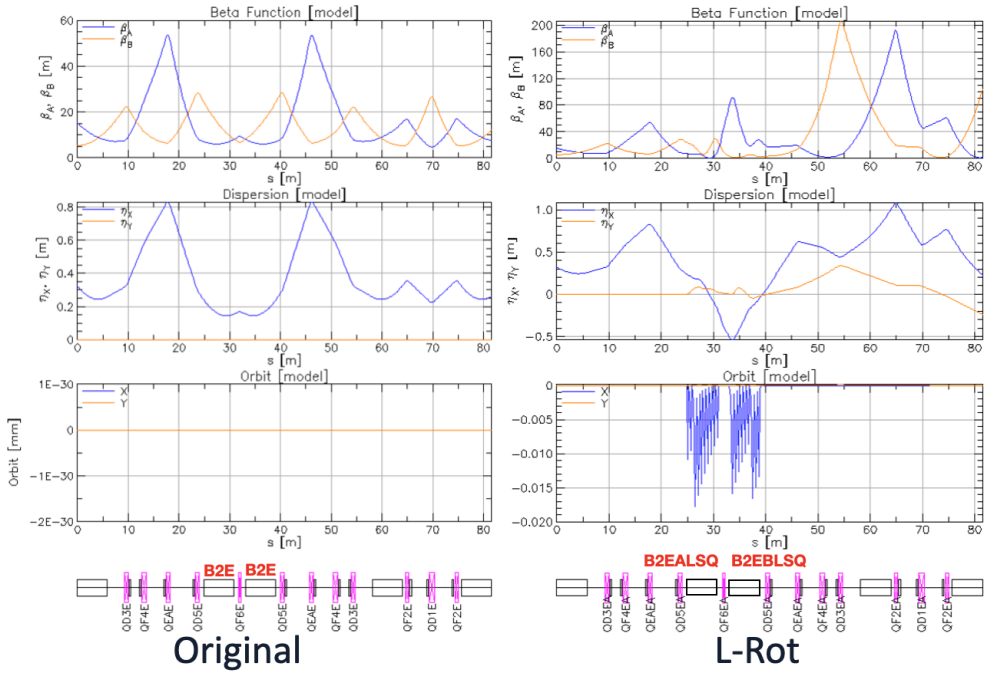

Figure 4.15: Comparison of the L-Rot Tuning Region before performing the optical rematch

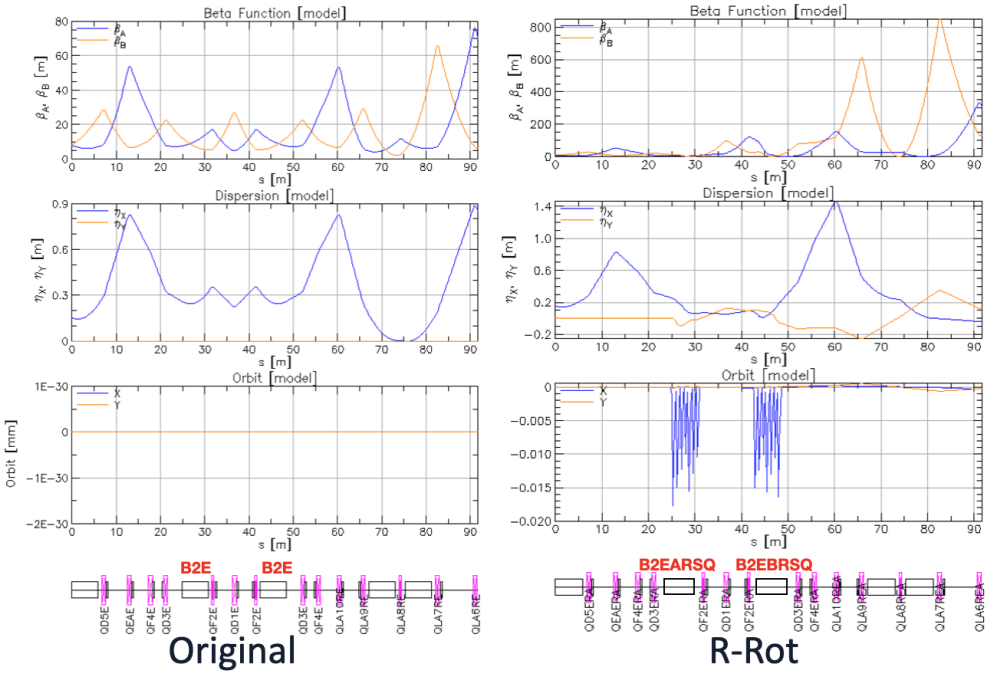

Figure 4.16: Comparison of the R-Rot Tuning Region before performing the optical rematch

4.5 Optical Rematch

The installation of the spin rotator is for the electron polarization purpose only, so it must be kept transparent to the ring. To achieve transparency, quadrupoles near the spin rotator are tuned to recover optics at the exit of the tuning area. After the tuning, optical functions will be matched to the original lattice outside the tuning area but changed inside, resulting in variations in the overall machine parameters such as chromaticity, Tune, and emittance. The chromaticity and the Tune must be rematched by taking other tuning measures to make the spin rotator fully transparent to the ring. However, the emittance can not be corrected as the original, and the best solution is to keep it as low as possible.

The optical rematch at the exit of the tuning region includes the match of Twiss parameters β_x, β_y, α_x, α_y, and the dispersion functions η_x,η_y, and η'_x,η'_y, eight parameters in total to be matched. Also, hkicks and vkicks need to be re-fitted to match the orbit. Performing this step is challenging, not only does it require the eight optical parameters to match, but also it has to consider the influence on ring parameters, such as the variation on the Tune and the emittance. If performing the optical rematch significantly affects the Tune, it is unrealistic to restore the original Tune. The best situation is that only the fractional component of the Tune is affected. Other than that, the luminosity directly depends on the horizontal and vertical emittances, which must be kept low to guarantee high luminosity [8].

Also, the match of vertical dispersion is quite tricky due to no vertical bending effect in the ring. An effective way to control the behaviour of vertical dispersion is to add extra constraints when performing the decoupling, which is to fix it at zero at the exit of each rotator magnet. However, it requires the use of strong skew-quads to achieve this goal. The stronger skew-quads are, the more they change the Twiss and overall ring parameters, making it more challenging to match these parameters. An alternative way is to control the dispersion at the rotator region, which requires fitting all skew-quads when tuning the ring quads and give up the decoupling at the exit of the first rotator magnet. Each skew-quad has two variables, strength and tilt. Thus, six skew-quads in the first rotator magnet will give 12 extra variables to match optical parameters. Refitting the six skew-quads in the second rotator magnet will adjust the behaviour of local optics and decouple the plane at the exit.

4.5.1 Optical Rematch for the L-Rot

The optical rematch for the L-Rot is performed by investigating existing quadrupoles located in nearby upstream and downstream regions. A finalized tuning plan is shown in **Figure 4.17**. As it shows, 12 quadrupoles near the L-Rot, including five identical pairs, are involved in the optical rematch for the L-Rot. We adjust the first four quadrupoles to control the upstream optics, the last seven quadrupoles to control the downstream optics, and QF6E to manipulate the behaviour of optics between two rotator magnets. Also, the beta functions are limited at two spots: one is located between two rotator magnets, and another is located at 6 meters downstream of the exit. In addition, all skew-quads are refitted at the same time, the limit on their strength k_1 is relaxed to 0.88 m^{-2} and 0.58 m^{-2} for B2EALSQ and B2EBLSQ respectively. After taking all these measures, the optics is recovered at the exit of the second QF2E in the tuning region. Due to the tuning of identical pairs, the symmetric structure of beta functions is preserved to a certain extent outside the rotator area. In the rotator region, the optical structure changed significantly due to the installation of rotator magnets.

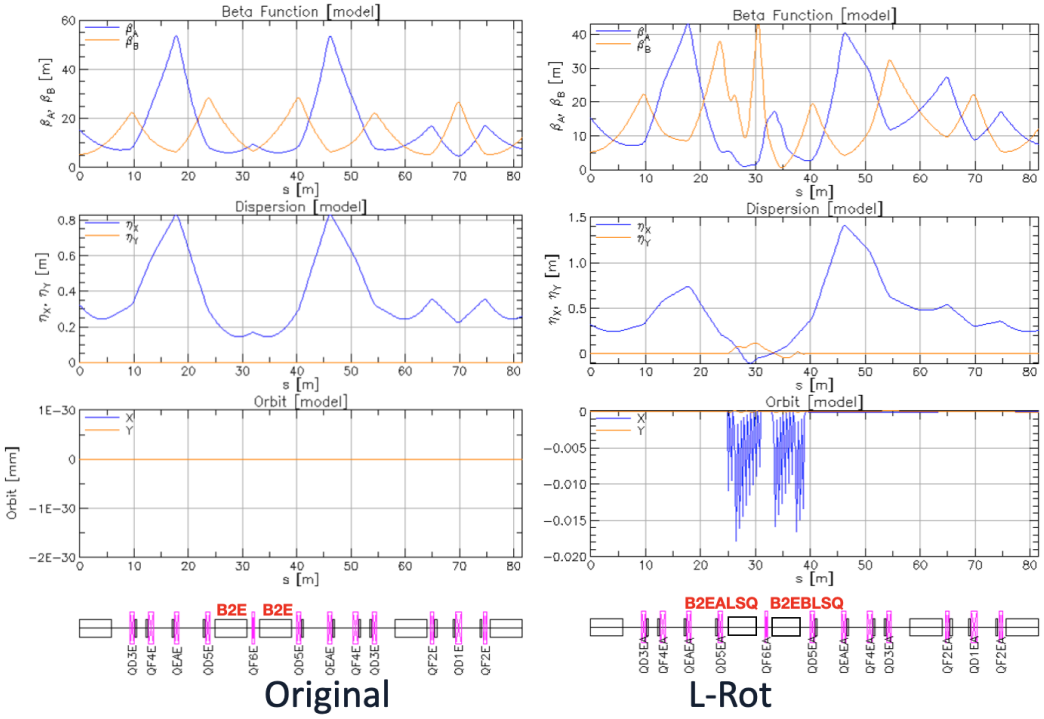

Figure 4.17: Comparison of the L-Rot Tuning Area after the match of optics

Achieving the optics rematch alone is insufficient for the desired solution, which also must guarantee there is no significant variation in the Tunes and keep the emittance low. Every time a result is determined for the open-geometry optimization, the L-Rot is put back into the HER lattice to run a closed-orbit simulation and see if exists a considerable influence on the horizontal, vertical Tunes and emittances. It turned out the installation of the spin rotator has no critical impact on the horizontal emittance but does have on the vertical emittance. The limit of the new vertical emittance is set to be 10 times as the original lattice because the overall vertical emittance is approximately the sum of the L-Rot and R-Rot rings when both of them are installed in the HER lattice. The current design of the machine is about 13 pm [8] for the vertical emittance, which is about 20 times of the HER lattice. In addition, the variation of Tunes needs to be limited to one. Some optimization results are used as better starting points in the new optimizations. It also might require stepping back to re-perform the decoupling to acquire a reasonable magnetic structure. There is no practical way to tell what the ideal magnetic design should be like, and it only can be examined by trial and error. The tuning has been performed dozens of times until determining the desired solution that satisfies all requirements. The finalized design of the L-Rot varies the Tunes with $\Delta Q_x = 0.38$, $\Delta Q_y = 0.27$, and amplifies the vertical emittance by 2.36 times and a negligible variation for the horizontal emittance. The key to finding the desired solution is to limit the beta function at a small value between the two rotator magnets, which is achieved by adjusting QF6E and requires strong magnetic strength. The existing strongest defocusing quadrupole is QLB7RE with an integrated strength $k_1 L$ = -0.603 m^{-1} or B_1 = -12.54 T/m; for the focusing quadrupole, the strongest one is QLA8LE with $k_1 L = 0.32443$ m^{-1} or $B_1 = 13.303$ T/m. The new integrated strength of QF6E is 0.342 m^{-1}, at the same level as the strongest focusing quadrupole, which is achievable. There is no significant adjustment for rest quadrupoles, as it is shown in **Table 4.7**. The maximum skew-quad strength is around 20 T/m, much lower than the 30 T/m technical limit.

	Tune Q_x	Tune Q_y	Emittance ε_x	Emittance ε_y
Original Ring	45.530994	43.580709	4.44061×10^{-9}	5.65367×10^{-13}
L-Rot Ring	45.912795	43.848515	4.69578×10^{-9}	1.338×10^{-12}

Table 4.7: Comparison the ring parameters of the original ring and L-Rot ring

Quads	L(m)	k_1L(Original)	k_1L(L-Rot)	B_1(Original) T/m	B_1(L-Rot) T/m
QD3E	0.826	-0.175	-0.177	-4.948	-5.012
QF4E	1.015	0.035	0.071	0.805	1.633
QEAE	0.826	0.183	0.175	5.178	4.961
QD5E	0.826	-0.179	-0.286	-5.074	-8.079
QF6E	0.557	0.163	0.342	6.855	14.366
QF2E	0.557	0.192	0.145	8.050	6.067
QD1E	1.015	-0.255	-0.203	-5.868	-4.682

Table 4.8: Ring qudrupoles used for matching the optics in the L-Rot Tuning Region

Skew-Quad	L(m)	k_1L	B_1 (T/m)	Tilt (rad)
B2EALSQ1	0.9837	0.511	12.133	-0.426
B2EALSQ2	0.9837	0.510	12.130	1.053
B2EALSQ3	0.9837	-0.314	-7.457	-0.988
B2EALSQ4	0.9837	0.855	20.315	0.030
B2EALSQ5	0.9837	0.688	16.350	-0.630
B2EALSQ6	0.9837	0.814	19.340	1.383
B2EBLSQ1	0.9837	0.558	13.266	0.651
B2EBLSQ2	0.9837	-0.482	-11.444	0.992
B2EBLSQ3	0.9837	0.426	10.119	-1.494
B2EBLSQ4	0.9837	0.338	8.024	-0.931
B2EBLSQ5	0.9837	0.562	13.359	0.735
B2EBLSQ6	0.9837	-0.185	-4.404	0.868

Table 4.9: Skew-qudrupoles in the L-Rot

4.5.2 Optical Rematch for the R-Rot

Compared with L-Rot, the tuning of the R-Rot is relatively easier. The strength of solenoids in the R-Rot is weaker, which requires weaker skew-quads to perform the plane decoupling. Thus, the installation of R-Rot less affects local optical functions. Following the same optimization procedure as the L-Rot, the finalized tuning plan is shown in **Figure 4.18**. Fourteen quadrupoles, including three identical pairs, are adjusted to match the optics at the exit of QLA6RE. Skew-quads are also re-optimized and only decouple the plane at the exit of the second rotator magnet B2EBRSQ. The transverse beam motion is coupled in two rotator magnets and the area in between where the beta functions are limited to a small value. Three quadrupoles (QF2E pair and QD1E) in that area are tuned to control local optical functions. As **Table 4.11** shows, there is no significant adjustment to the existing quadrupoles. The structure of beta functions is well preserved outside the rotator region. However, compared with the L-Rot, the R-Rot has a more significant impact on the vertical motion. It might be due to the long gap between two R-Rot magnets, where the beam motion is coupled. The installation of the R-Rot changes the Tune values by $\Delta Q_x = -0.14$, $\Delta Q_y = 0.60$, and amplifies the vertical emittance 5.78 times which is acceptable.

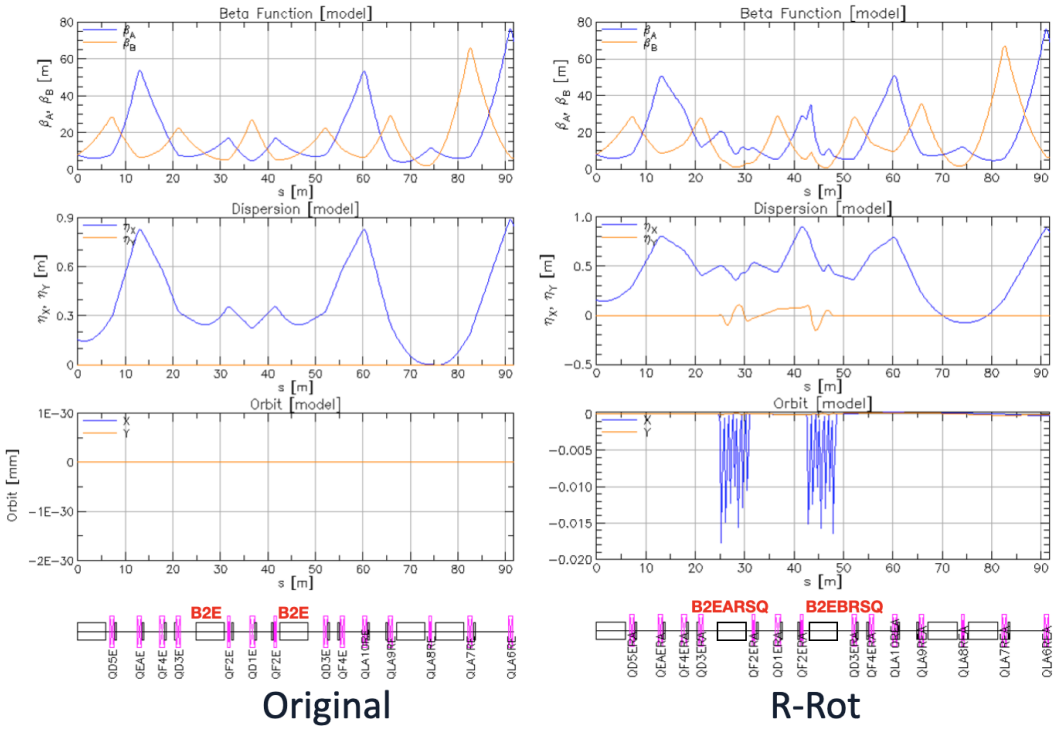

Figure 4.18: Comparison of the R-Rot Tuning Region after the optical rematch

	Tune Q_x	Tune Q_y	Emittance ε_x	Emittance ε_y
Original Ring	45.530994	43.580709	4.44061×10^{-9}	5.65367×10^{-13}
L-Rot Ring	45.395765	44.178970	4.63084×10^{-9}	3.26913×10^{-12}

Table 4.10: Comparison the ring parameters of the original ring and R-Rot ring

Quads	L(m)	k_1L(Original)	k_1L(R-Rot)	B_1(Original) T/m	B_1(R-Rot) T/m
QD5E	0.826	-0.179	-0.165	-5.074	-4.667
QEAE	0.826	0.183	0.154	5.178	4.362
QF4E	1.015	0.035	0.067	0.805	1.538
QD3E	0.826	-0.175	-0.251	-4.948	-7.088
QF2E	0.557	0.192	0.183	8.050	7.659
QD1E	1.015	-0.255	-0.274	-5.868	-6.311
QLA10RE	0.826	0.202	0.185	5.718	5.234
QLA9RE	0.826	-0.237	-0.226	-6.703	-6.385
QLA8RE	0.557	0.203	0.169	8.527	7.106
QLA7RE	0.826	-0.192	-0.195	-5.438	-5.522
QLA6RE	0.826	0.202	0.205	5.716	5.808

Table 4.11: Ring qudrupoles used for matching the optics in the R-Rot Tuning Region

Skew-Quad	L(m)	k_1L	B_1 (T/m)	Tilt (rad)
B2EARSQ1	0.9837	0.435	10.341	-2.610
B2EARSQ2	0.9837	0.600	14.258	2.290
B2EARSQ3	0.9837	0.043	1.032	2.328
B2EARSQ4	0.9837	-0.566	-13.451	-0.180
B2EARSQ5	0.9837	0.600	14.258	-2.545
B2EARSQ6	0.9837	-0.591	-14.038	0.618
B2EBRSQ1	0.9837	0.495	11.769	-2.480
B2EBRSQ2	0.9837	0.532	12.648	2.238
B2EBRSQ3	0.9837	0.280	6.663	-0.960
B2EBRSQ4	0.9837	-0.565	-13.429	-0.197
B2EBRSQ5	0.9837	0.600	14.258	-2.846
B2EBRSQ6	0.9837	-0.383	-9.098	0.475

Table 4.12: Skew-qudrupoles of the R-Rot

An alternative solution for the optical rematch of the R-Rot is determined, which only requires adjusting seven ring quadrupoles, including three identical pairs. As it shows in **Figure 4.19**, the alternative solution has a much shorter tuning region, and the local beta functions structure is almost recovered as the original. The alternative R-Rot barely changes the horizontal Tune but has a more significant impact on the vertical Tune. The variations of Tune values are $\Delta Q_x = -0.061117$, $\Delta Q_y = 0.696066$, and the vertical emittance is amplified by 5.56 times which is below the constraint of 10 times. To determine which tuning plan for R-Rot is to be implemented, further studies need to be applied to the HER lattice with both the L-Rot and the R-Rot installed.

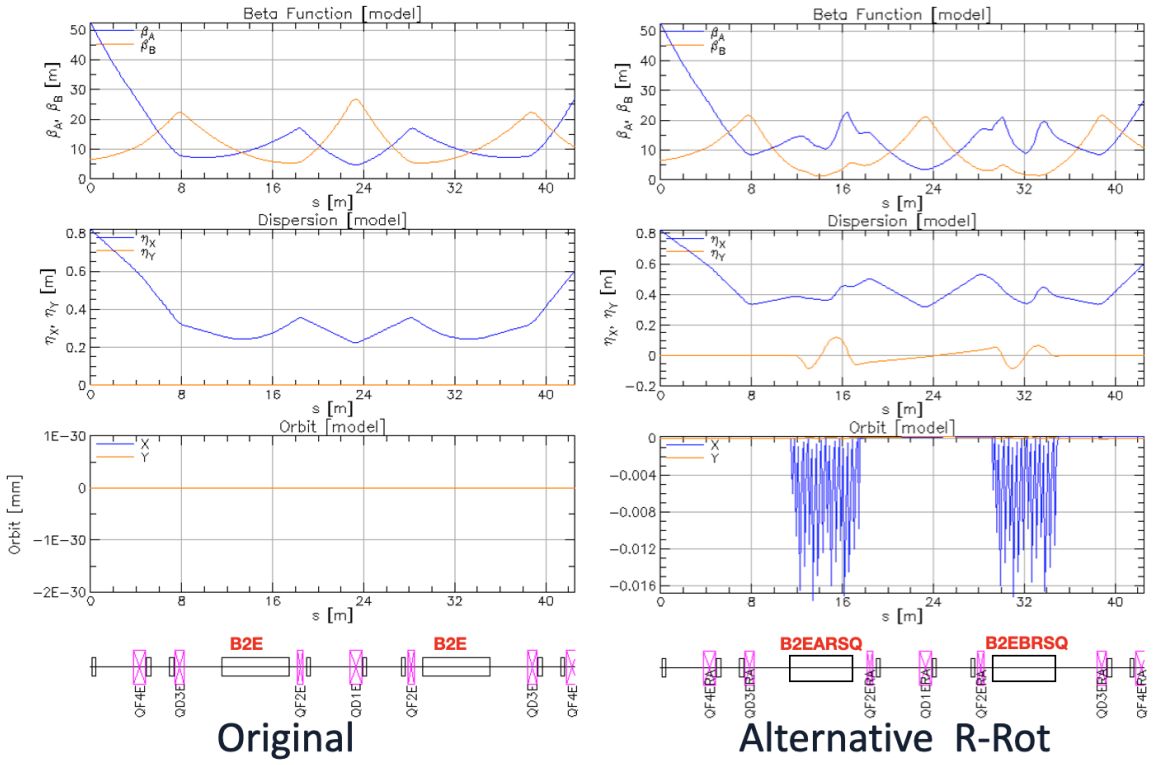

Figure 4.19: Comparison of the Alternative R-Rot Tuning Region after the optical rematch

	Tune Q_x	Tune Q_y	Emittance ε_x	Emittance ε_y
Original Ring	45.530994	43.580709	4.44061×10^{-9}	5.65367×10^{-13}
Alternative R-Rot Ring	45.469877	44.276775	4.58781×10^{-9}	3.14703×10^{-12}

Table 4.13: Comparison the ring parameters of the original ring and alternative R-Rot ring

Quads	L(m)	k_1L(Original)	k_1L(R-Rot)	B_1(Original) T/m	B_1(R-Rot) T/m
QF4E	1.015	0.035	0.031	0.805	0.716
QD3E	0.826	-0.175	-0.256	-4.948	-7.230
QF2E	0.557	0.192	0.161	8.050	6.766
QD1E	1.015	-0.255	-0.273	-5.868	-6.285

Table 4.14: Ring qudrupoles used for matching the optics in the alternative R-Rot Region

Skew-Quad	L(m)	k_1L	B_1 (T/m)	Tilt (rad)
B2EARSQ1	0.9837	0.424	10.078	-2.522
B2EARSQ2	0.9837	0.600	14.258	2.266
B2EARSQ3	0.9837	0.086	2.054	2.264
B2EARSQ4	0.9837	-0.493	-11.714	-0.276
B2EARSQ5	0.9837	0.600	14.258	-2.592
B2EARSQ6	0.9837	-0.566	-13.451	0.654
B2EBRSQ1	0.9837	0.499	11.848	-2.457
B2EBRSQ2	0.9837	0.561	13.318	2.222
B2EBRSQ3	0.9837	0.278	6.599	-1.001
B2EBRSQ4	0.9837	-0.577	-13.710	-0.273
B2EBRSQ5	0.9837	0.600	14.258	-2.877
B2EBRSQ6	0.9837	-0.352	-8.355	0.597

Table 4.15: Skew-qudrupoles of the alternative R-Rot

4.6 Studies of Rotator Ring

Since the optical functions are matched to the original ring, both the L-Rot and R-Rot are installed in the High Energy Ring lattice to perform a closed-orbit simulation and studies. The first thing to check is the transparency, including the behaviour of optics and orbit. As it is shown in **Figure 4.20**, the beta and dispersion functions look identical to the original except the rotator area, which indicates the optical re-match is quite successful. The squiggle that appeared in the orbit plot is the wiggler effect, which is avoided by rescaling the orbit. As **Figure 4.21** shows, compared with the original, the horizontal and vertical orbits in the rotator ring are approximately twice amplified; and the Rot has a relatively smaller closed-orbit distortion than the alternative Rot. More studies will be applied to the lattice of rotator ring to identify the best design.

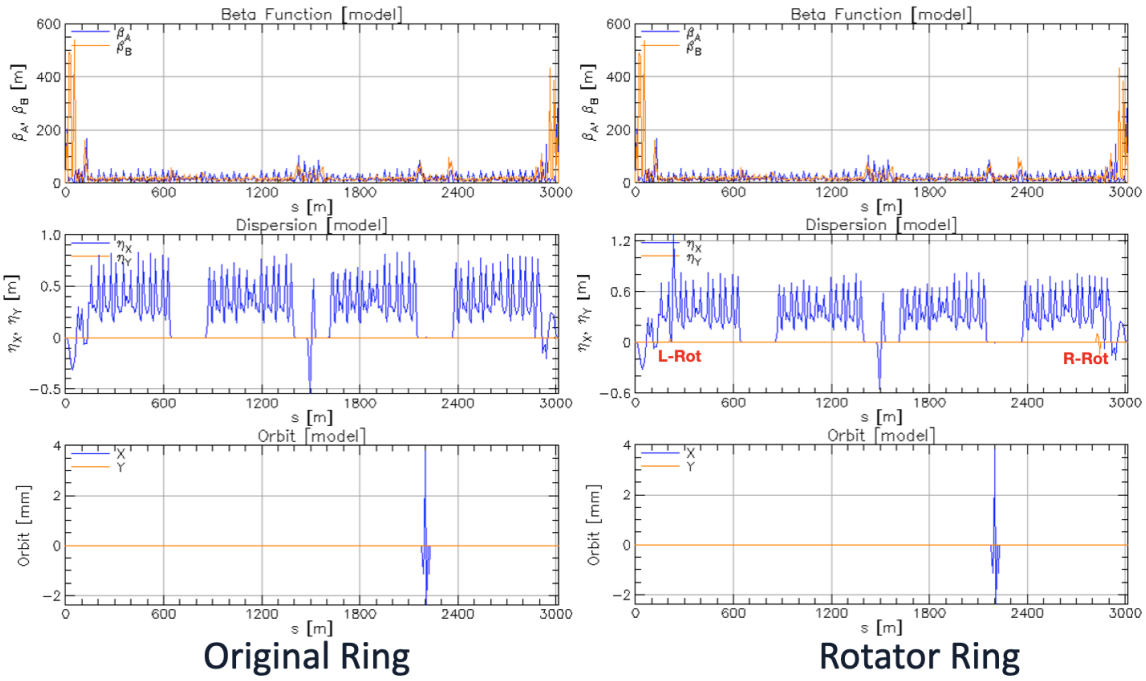

Figure 4.20: Comparison of the Full Lattice

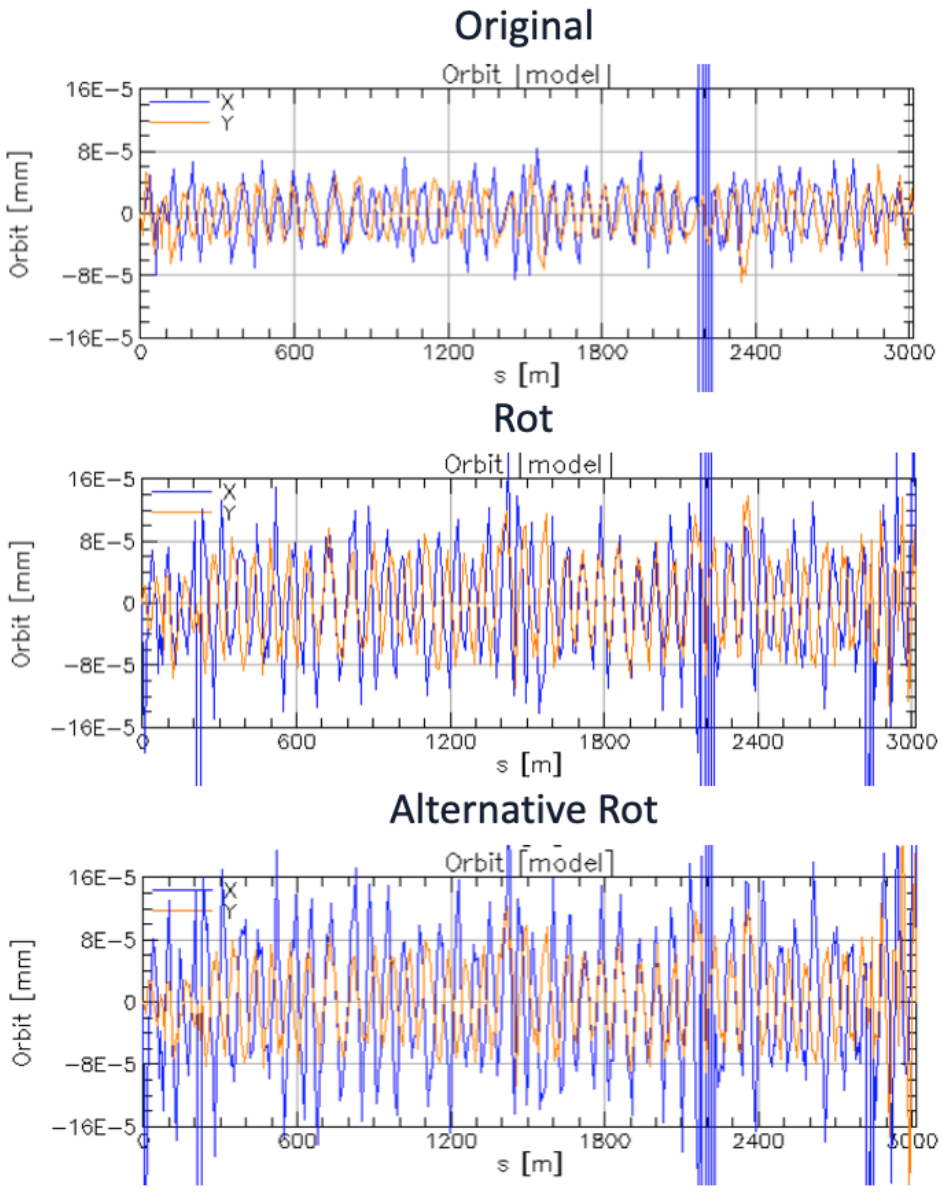

Figure 4.21: Comparison of the orbit of the Full Lattice

4.6.1 Single-Particle Spin Tracking Result

The spin tracking is performed by using the Polymorphic Tracking Code(PTC) interface in BMAD. **Table 4.16** shows the single-particle spin tracking result in the rotator ring, the longitudinal spin alignment at the IP is greater than 99.99%, and the spin at both the entrance and exit of the rotator has the vertical spin alignment also greater than 99.99%, which meets the expectation of spin rotator installation.

Spin Component	Entrance of Rot	IP	Exit of Rot
X	-0.000003279202	-0.000004467736	-0.000006374893
Y	0.999999999980	0.000002679620	0.999999999979
Z	-0.000005360028	0.999999999986	0.000000782519

Table 4.16: Spin Tracking Result with the Spin Rotator installed in the Ring

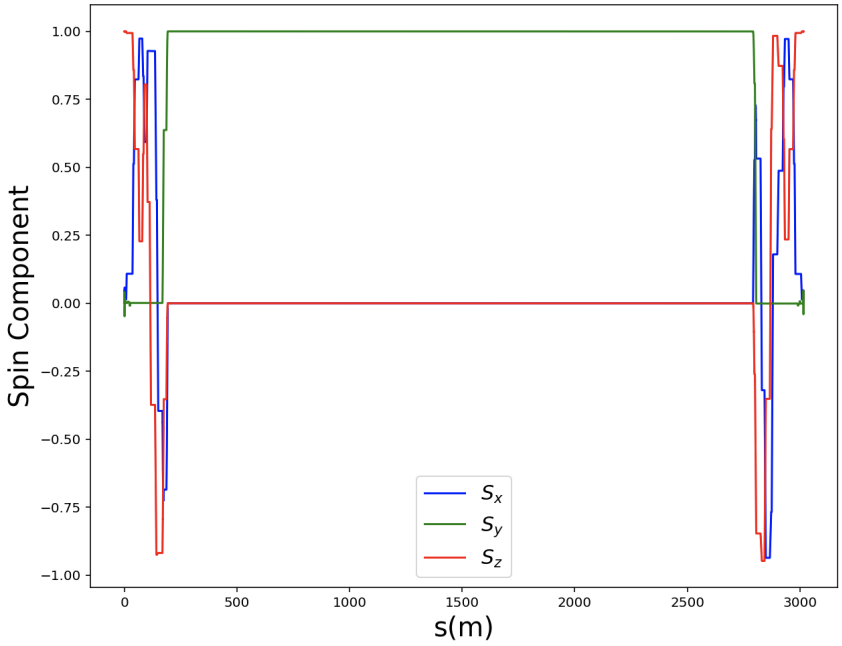

Figure 4.22: Spin motion of the electron in the Rotator Ring (Co-moving frame)

All optimizations are performed with the positron, and the electron simulation is accomplished by running the reverse lattice simulation with BMAD. The co-moving frame spin motion of the electron in the rotator ring is shown in **Figure 4.22**, and **Figure 4.23** shows the simulation of lab frame spin motion. The positive y-direction is defined to be aligned with the dipole field, which is downward in the KEK frame. The injected beam must be vertically polarized to acquire the longitudinal polarization and anti-vertically polarized to reach the anti-longitudinal polarization at the IP. The ideal spin motion follows that as the vertically polarized beam is injected into the ring, its vertical spin remains unchanged in the dipole field until it reaches the L-Rot, where the spin is rotated to the horizontal plane at the exit. The spin precession continues in the existing dipole fields at the minor arc between the L-Rot and R-Rot and reaches the longitudinal direction at the IP, then back to vertical when exits the R-Rot.

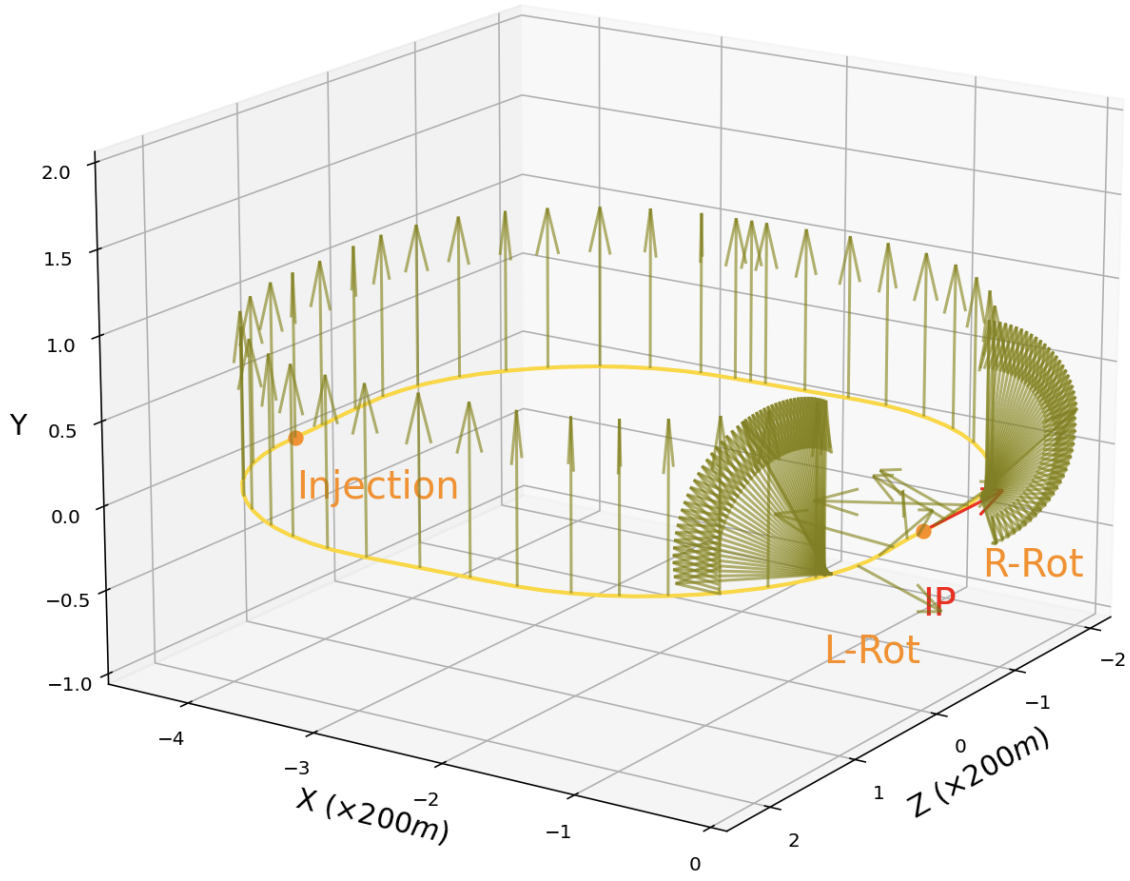

Figure 4.23: Spin motion of the electron in the Rotator Ring (Lab frame)

4.6.2 Ring Parameters

The last thing to check is the impact of the tuning area on the overall machine parameters. As shown in **Table 4.17**, the rotator rings do not have considerable influence on the Damping partitions and the horizontal emittance, but they have a critical effect on other ring parameters, including the Tunes, chromaticities, and the vertical emittance. Although the vertical emittance of the rotator ring 4 pm is much higher than the original lattice 0.57 pm, it is nonetheless substantially smaller than the HER design vertical emittance of 12.9 pm [8]. The variation on the horizontal Tune is within 0.5 for both two rotator rings, only affecting the fractional component. However, there is a significant variation on the vertical Tunes, which almost reach one and changes the integer part. Although the alternative Rot requires adjusting fewer quadrupoles to achieve the optical rematch, it has a more significant impact on horizontal and vertical Tunes. The finalized spin rotator design will be depending on the Tune match and beam tracking result. The variation in chromaticities is not worried, which can be fixed by a numerical approach discussed in the next chapter.

Machine parameter	Original Ring	Rot Installed	Alternative Rot Installed
Tune Q_x	45.530994	45.777566	45.851677
Tune Q_y	43.580709	44.446774	44.544579
Chromaticity ξ_x	1.593508	-0.725173	-1.244560
Chromaticity ξ_y	1.622865	1.879936	2.121571
Damping partition J_x	1.000064	0.984214	0.973110
Damping partition J_y	1.000002	1.005265	1.005193
Emittance ε_x (m)	4.44061×10^{-9}	4.88965×10^{-9}	4.84923×10^{-9}
Emittance ε_y (m)	5.65367×10^{-13}	4.01654×10^{-12}	3.93024×10^{-12}

Table 4.17: Comparison of the ring parameters before and after the Spin Rotator installed in the SuperKEKB High Energy Ring

4.7 Match the First Order Chromaticity

To match the original first-order chromaticity, sextupoles need to be tuned. Consider the extra quadrupole strength introduced by the sextupoles $k_{sext} = mD\frac{\Delta p}{p}$, the effective total chromaticity is given by [9]:

$$\xi_{tot} = \frac{1}{4\pi}\oint \Big[m(s)D(s) + k(s)\Big]\beta(s)ds, \tag{4.6}$$

where m is sextupole strength, $D(s)$ is the dispersion function, k is the strength of the quadrupole, and $\beta(s)$ is the beta function.

Based on Eq.4.1, it can be concluded that the chromaticity is an accumulative effect of quadrupoles and sextupoles and linearly depends on the sextupole strength because varying it does not change the local optical functions such as the beta function. Thus, the variation of the first-order chromaticity can be expressed as a linear combination of the variation of individual sextupoles strength

$$\begin{cases} \Delta\xi_x = \sum_i p_i \Delta x_i \\ \Delta\xi_y = \sum_i q_i \Delta x_i \end{cases}, \tag{4.7}$$

where $\Delta\xi_x$ is the variation of the horizontal chromaticity, and $\Delta\xi_y$ denotes the variation of the vertical chromaticity; the slope p_i, q_i depends on the horizontal and the vertical component of local optical functions, respectively; Δx_i is the variation of the integrated sextupole strength x_i.

Assume N (N > 2) sextupoles are tuned to match the first-order chromaticity. N variables to be determined and exist two equations, so there are N-2 free variables. Manipulate Eq. 4.2 can find that the variation of the integrated strength of any sextupole Δx_j can be expressed as

$$\Delta x_j = \frac{p_k \Delta\xi_y - q_k \Delta\xi_x + \sum_{i \neq j} \big(p_i q_k - p_k q_i\big)\Delta x_i}{p_k q_j - p_j q_k}, \tag{4.8}$$

with $j \neq k$.

Note Δx_k term vanishes in the expression above, Δx_j is expressed as a linear combination of free variables. For example, pick up Δx_1, Δx_2 to be computed from the rest $\{\Delta x_3, ..., \Delta x_N\}$.

$$\Delta x_1 = \frac{p_2 \Delta\xi_y - q_2 \Delta\xi_x + \big(p_3 q_2 - p_2 q_3\big)\Delta x_3 + ... + \big(p_N q_2 - p_2 q_N\big)\Delta x_N}{p_2 q_1 - p_1 q_2}, \tag{4.9}$$

$$\Delta x_2 = \frac{p_1 \Delta\xi_y - q_1 \Delta\xi_x + \big(p_3 q_1 - p_1 q_3\big)\Delta x_3 + ... + \big(p_N q_1 - p_1 q_N\big)\Delta x_N}{p_1 q_2 - p_2 q_1}. \tag{4.10}$$

Due to the high degree of freedom, there exist infinite solutions. The desired solution is to have all sextupoles staying below the physical limit. Additionally, it is beneficial to minimize the variation of the sextupole strength, which might allow the original power supply source to reach the tuning purpose. Lmdif can find a local minimum but it does not guarantee all sextupoles are physical. Also, it has difficulty determining the global minimum due to the large degrees of freedom. Therefore, it is necessary to find a starting point close to the global minimum. An algorithm is developed to determine a better starting point, and the basic idea is to feed numbers into Eq.4.3 to compute two unknown variables and compare solutions to approach the global minimum gradually. The detail of the algorithm follows:

Step 1: Generate nominee data set for N-2 free variables $\{\Delta x_3, \Delta x_4, ..., \Delta x_N\}$ within a reasonable range, let α_i denote the data set for Δx_i, α_{ij} denote jth element in the data set α_i.

Step 2: Pick up an element α_{ij} from α_i for each variable Δx_i, and generate a data set for free variables $\{\alpha_{3j}, \alpha_{4j}, ..., \alpha_{Nj}\}$

Step3: Compute Δx_{1j}, Δx_{2j} from $\{\alpha_{3j}, \alpha_{4j}, ..., \alpha_{Nj}\}$ and only record solutions which stay in the desired range ($x_1 + \Delta x_1, x_2 + \Delta x_2$ below the physical limit and sign does not change), denoted as $\Delta x_{1k}, \Delta x_{2k}$

Step4: Find the maximum strength in each solution set $\{x_1 + \Delta x_{1k}, x_2 + \Delta x_{2k}, x_3 + \alpha_{3k}, ..., x_N + \alpha_{Nk}\}$, denoted as X_k

Step5: make a comparison between X_k, and determine the index of the minimum in X_k , denoted as m. Then, a local minimum solution is given by $\{x_1 + \Delta x_{1m}, x_2 + \Delta x_{2m}, x_3 + \alpha_{3m}, ..., x_N + \alpha_{Nm}\}$

Iteration: reset a narrower range around α_{im} to generate a new data set for free variables Δx_i, repeat steps 2 to 5; gradually narrow the data set range until the global minimum is found, check the solution and make sure the sign of all defocusing and focusing sextupoles does not change

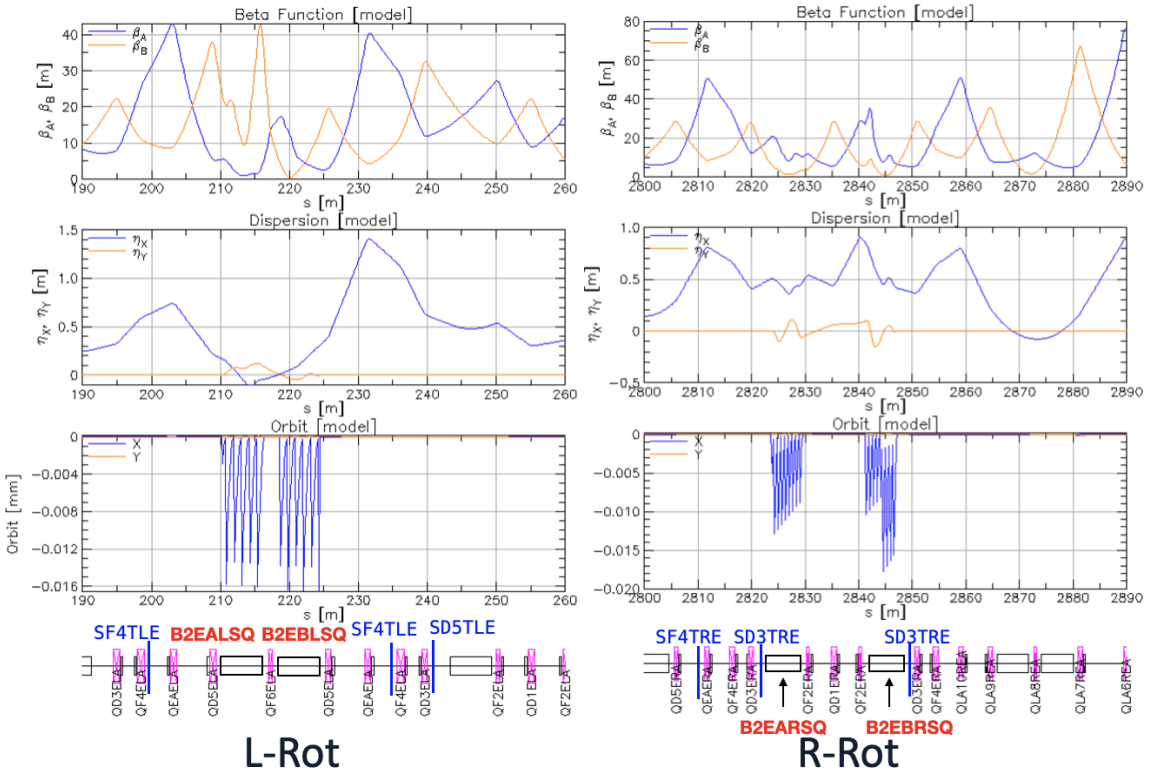

Figure 4.24: Sextupoles in the Rot Tuning Area

Before applying the algorithm, it requires figuring out which sextupoles can be tuned. The phase advance between the sextupole pair needs to be fixed at π to cancel their lowest order of the transverse nonlinearity to each other [25]. Although the dynamics are maintained as the original outside the tuning region, it does change inside the tuning area and affects local sextupoles. As **Figure 4.24** shows, there are three sextupoles in both the L-Rot and R-Rot tuning regions. The phase advance between these sextupole pairs is no longer π, as shown in **Table 4.18**. SD3TRE is affected slightly due to the adjustment of upstream QD5RE; the phase advance is not π but close. SD3TRE is not adjusted due to the phase advance slightly shifted from π , and all the rest sextupole pairs in **Table 4.12** are turned off; their strength is set to be zero. Putting both the L-Rot and the R-Rot into the HER lattice and turning these sextupole pairs off yields new chromaticities $\xi_x = -0.616932, \xi_y = -6.553531$; and the variation of chromaticities needs to be $\Delta\xi_x = 1.593508 - (-0.616932) = 2.21044, \Delta\xi_y = 1.622865 - (-6.553531) = 8.176396$.

Index	sextupole	Ψ_x	Ψ_y	$\Delta\Psi_x$	$\Delta\Psi_y$
1692	SF4TLE	22.6040	24.9780		
2108	SF4TLE	29.1830	30.4680	6.5790	5.4900
2124	SD5TLE	29.5520	30.7900		
2150	SD5TLE	31.8170	33.3440	2.2650	2.5540
5306	SF4TRE	263.6200	245.6500		
5340	SF4TRE	266.7700	248.600	3.1500	2.9500
5356	SD3TRE	267.1100	248.9300		
5762	SD3TRE	269.8800	256.2900	2.7700	7.3600

Table 4.18: Sextupoles located at the rotator tuning area

SLX and SLY sextupoles are not touchable, as mentioned in **Section 3.3**, so candidates can only be chosen from the defocusing sextupoles (SD*) and the focusing sextupoles (SF*). In order to reach the maximum dynamic aperture, all SD/SF sextupoles should be tuned. However, due to computational difficulty applying the algorithm to all the touchable SD/SF sextupole pairs (45 in total), only six sextupole pairs near the rotator tuning region are tuned, including SD3TLE, SF6TLE, SD7TLE, SD7TRE, SF6TRE, and SD5TRE. Sextupoles will be re-tuned after Tune

values are matched to the original. Right now, we only focus on giving an applicable plan for rematching the first-order chromaticities. The non-linear effects will be explored with beam tracking. According to KEK experts [26], all SF/SD sextupoles in the High Energy Ring are the same type of magnets. All SF sextupoles share the same length, so do all SD sextupoles. Thus, the physical limit of the SF and SD sextupoles is temporarily set to be the same as the strongest existing defocusing and focusing quadrupoles, respectively. For defocusing, the strongest one is SD7ORE with $b_2 = -7.242$; for focusing, the strongest one is SF6FRE with $b_2 = 2.296$.

The coefficients p_i, q_i in Eq.4.3 need to be determined to implement the algorithm, which is achieved by manually investigating the lattice of the High Energy Ring with spin rotator installed. The linear relationship in Eq.4.2 holds for the sextupole pair because of having two identical elements, and the slope is the sum of two elements. Begin with zero, increase the strength of one sextupole pair by a step of 0.5 until it reaches $b_2 = 3$, record the corresponding horizontal and vertical chromaticity, and repeat the same procedure for other sextupoles. Then, plot ξ_x, ξ_y as a function of b_2 for each pair, and apply linear regression on the data to determine the slope, which is p_i, q_i.

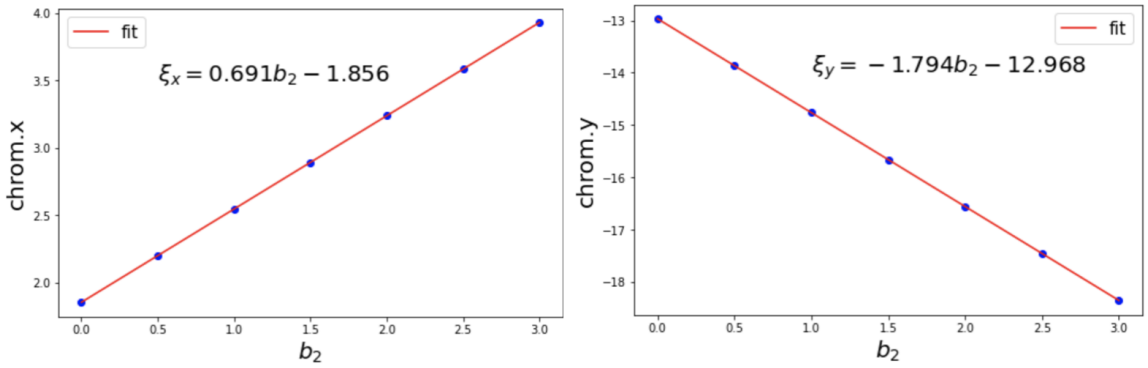

Figure 4.25: chromaticity component vs the strength of SD3TLE pair

The algorithm is implemented on Python to determine the nominee solution for the global minimum and then use it as the starting point to run a BMAD optimization in closed geometry. The result is given in **Table 4.19**, all new sextupoles stay within the physical limit.

Sextupole	length (m)	b_2 (Original)	b_2 (Rot) BMAD	b_2 (Rot) Python
SD3TLE	1.03	-3.577	- 4.027	-4.061
SF6TLE	0.334	0.818	1.008	1.025
SD7TLE	1.03	-3.607	-4.062	-4.061
SD7TRE	1.03	-1.730	-4.042	-4.057
SF6TRE	0.334	0.829	1.596	1.596
SD5TRE	1.03	-1.695	-4.088	-4.058

Table 4.19: Sextupoles used for matching the linear chromaticities

As **Figure 4.26** shows, only the SD3TRE pair is located in the alternative R-Rot tuning region, and the SF4TRE pair is no longer affected, which gives one more candidate for rematching chromaticities. For the alternative rotator ring, turning SF4TLE, SD5TLE, and SD3TRE pairs off changes chromaticities to $\xi_x = -1.219330, \xi_y = -6.084533$, and the variation of chromaticities needs to be $\Delta\xi_x = 2.812838, \Delta\xi_y = 7.707398$ to match the original. Applying the same analyzing process to the alternative rotator ring with tuning the extra SF4TRE pair. The Python algorithm result indicates that the variation on SF6TRE is negligible, not touched in Tao Optimization. The optimization result is shown in **Table 4.20**, all sextupoles are below the physical limit.

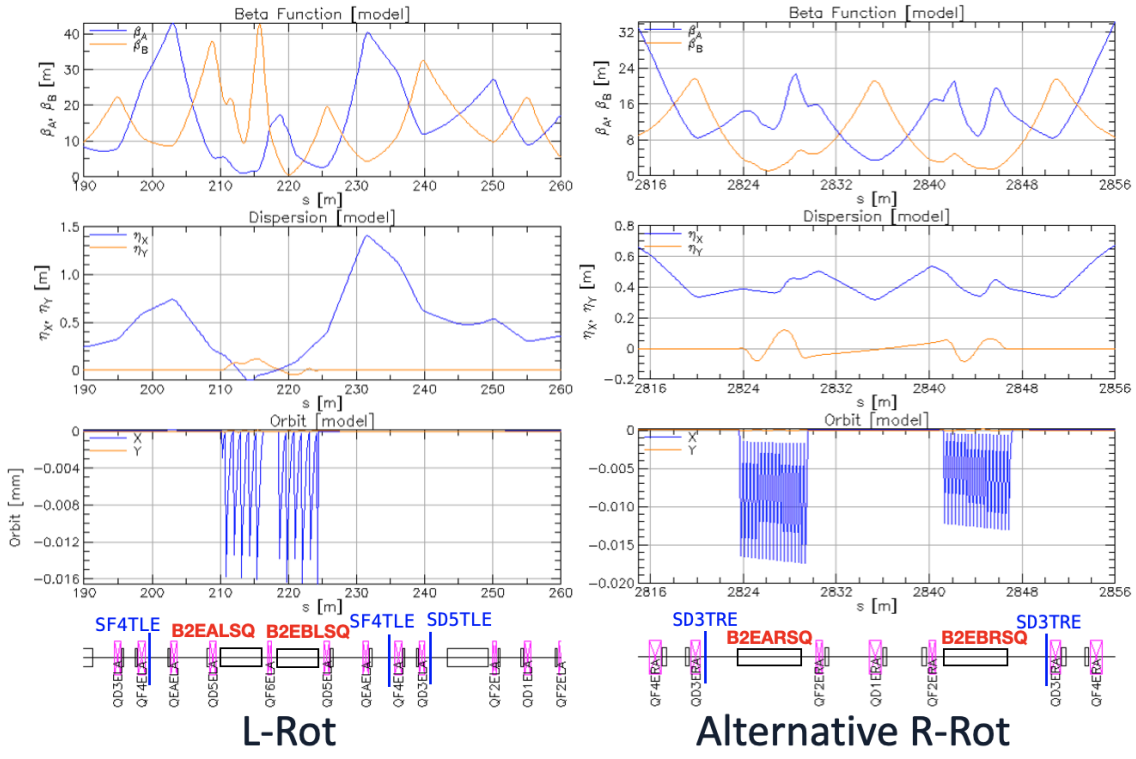

Figure 4.26: Sextupoles in the Alternative Rot Tuning Area

Sextupole	length (m)	b_2 (Original)	b_2 (Rot) BMAD	b_2 (Rot) Python
SD3TLE	1.03	-3.577	- 4.065	-4.008
SF6TLE	0.334	0.818	1.080	1.054
SD7TLE	1.03	-3.607	-3.854	-4.007
SD7TRE	1.03	-1.730	-4.150	-4.015
SF6TLE	0.334	0.829	not applicable	0.858
SD5TRE	1.03	-1.695	-4.005	-4.009
SF4TRE	0.334	0.505	1.274	1.276

Table 4.20: Sextupoles used for matching the first order chromaticities for the alternative Rotator Ring

Chapter 5

Future Steps and Beam Tracking Studies with Bmad

5.1 Tune Match Studies

Machine parameter	Original Ring	Rot Installed	Alternative Rot Installed
Tune Q_x	45.530994	45.777566	45.851677
Tune Q_y	43.580709	44.446774	44.544579
Chromaticity ξ_x	1.593508	1.593508	1.593508
Chromaticity ξ_y	1.622865	1.622865	1.622865
Damping partition J_x	1.000064	0.984214	0.973110
Damping partition J_y	1.000002	1.005265	1.005193
Emittance ε_x	4.44061×10^{-9}	4.88965×10^{-9}	4.84923×10^{-9}
Emittance ε_y	5.65367×10^{-13}	4.01654×10^{-12}	3.93024×10^{-12}

Table 5.1: Comparison of the ring parameters after matching the first-order chromaticities

The original Tunes must be restored to make the spin rotator fully transparent to the High Energy Ring. The tuning procedure begins with finding a straight area where both the horizontal and the vertical dispersion functions are zero. Adjusting the quadrupoles at this area can match the Tunes without affecting the dispersion. The optimization target is not just to recover original Tunes, and it also needs to guarantee the optics to be matched at the exit of the tuning area, including β_x, β_y, and α_x, α_y. Six parameters in total are to be matched, thus, requires at least six variables. **Figure 5.1** shows the straight area between s = 649 to 856 m in the ring

where the tuning is considered to be performed. Local quadrupoles have a symmetric distribution about the focusing quadrupole QFRNE at s = 753 m. There are six pairs of identical quadrupoles labeled from QR7NE to QR2NE symmetrically distributed at both ends and six groups of alternating defocusing quadrupoles QDRNE and focusing quadrupoles QFRNE in the middle. Therefore, the beta function follows a symmetric structure. As an overall machine parameter, the match of the Tune requires a closed-orbit optimization. Adjusting the quarupole in the closed-orbit will affect the downstream beta function and influence the upstream optical functions. The symmetry of the beta functions must be maintained to have the optics matched at both the entrance and the exit of the tuning area, so the strength of quadrupoles with the same name must be kept identical. Thus, eight variables can be applied for the tuning, which gives two degrees of freedom. The adjustment of QDRNE and QFRNE is mainly for fixing the Tunes, and the tuning of the rest quadrupoles is mostly for the optical rematch. In addition, the integrated strength of these quadrupoles must be limited to 0.012 $m^{-1} \leqslant k_1 L \leqslant 0.31\ m^{-1}$ according to KEK expert [27].

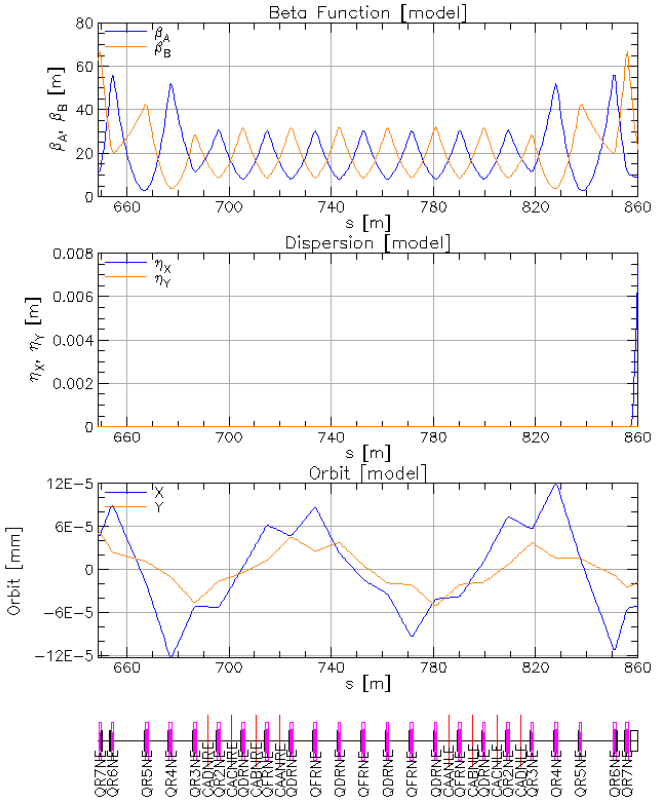

Figure 5.1: Straight area in the High Energy Ring

However, due to the difficulty performing the optimization in the closed-orbit lattice, it is challenging to have both the Tunes and the optics matched simultaneously. Unlike the sextupoles, tuning quadrupoles changes the beta functions, and the variation can not be analytically determined. Instead of fully matching the Tunes, we first aim at matching the fractional component of the Tune. Recall Eq.2.16, the Tune shift is given by: $dQ = \frac{1}{4\pi}\Delta k\beta ds$ when the quadrupole deviation is small. Notice for a small quadrupole deviation, the local beta function is barely affected. Thus, the total Tune shift can be approximated by:

$$\Delta Q \sim \sum_i \frac{1}{4\pi}\beta_i \Delta k_i L_i, \tag{5.1}$$

where β_i is the local beta function, Δk_i is the variation of the quadrupole strength k_i, and L_i is the length of the quadrupole with the index of i.

Based on Eq.5.1, we can conclude that if the deviation is sufficiently small, the Tune can be gradually shifted without changing the beta function too much, which might allow optimizing the Tune and optics simultaneously. Thus, a method called the "Ladder Method" is developed to recover the Tunes. The basic idea is to gradually shift the Tune and approach the optimizing target, as shown in **Table 5.2**. For each step, we vary the Tune with a tiny amount by tuning the QDRNE and QFRNE and then optimize both the Tune and optics by tuning all quadrupoles at the straight section. However, the optimizer still has difficulty optimizing both the β and α simultaneously. We have to give up matching the α to perform the "Ladder Method." Finally, the fractional component of the Tunes is matched to the original and the variation in α is small, $\Delta\alpha_x = 0.00028495$, and $\Delta\alpha_y = -0.01624934$, with $\alpha_x = 0.44282337$, and $\alpha_y = 6.77700412$ before the tuning. The validation of this method is to be confirmed with Uli Wienands and KEK experts since the α is not optimized in this method. **Figure 5.2** is the comparison of the straight section. As it shows, the symmetry of the beta function structure is well preserved. Also, as it shows in **Table 5.3**, there is no significant variation in the quadrupole strength, which indicates the "Ladder Method" might allow it to cross the integer and fully match the vertical Tune.

Step	0th	1st	2nd	3rd	4th
Q_x	45.777566	45.7282516	45.6296228	45.5803084	45.530994
Q_y	44.446774	44.473561	44.527135	44.553922	44.580709

Table 5.2: Ladder Method: taking steps to approach the fraction component of the orginal Tune

Quadrupole	Length (m)	k_1 (m^{-2}) original	$k_1(m^{-2})$ Rot
QFRNE	1.080	0.122	0.107
QDRNE	1.080	-0.118	-0.122
QR7NE	0.826	-0.252	-0.253
QR6NE	1.015	0.196	0.197
QR5NE	1.080	-0.110	-0.110
QR4NE	1.080	0.144	0.146
QR3NE	1.080	-0.145	-0.145
QR2NE	1.080	0.110	0.103

Table 5.3: Quadrupoles used for matching the fraction Tunes for the rotator ring

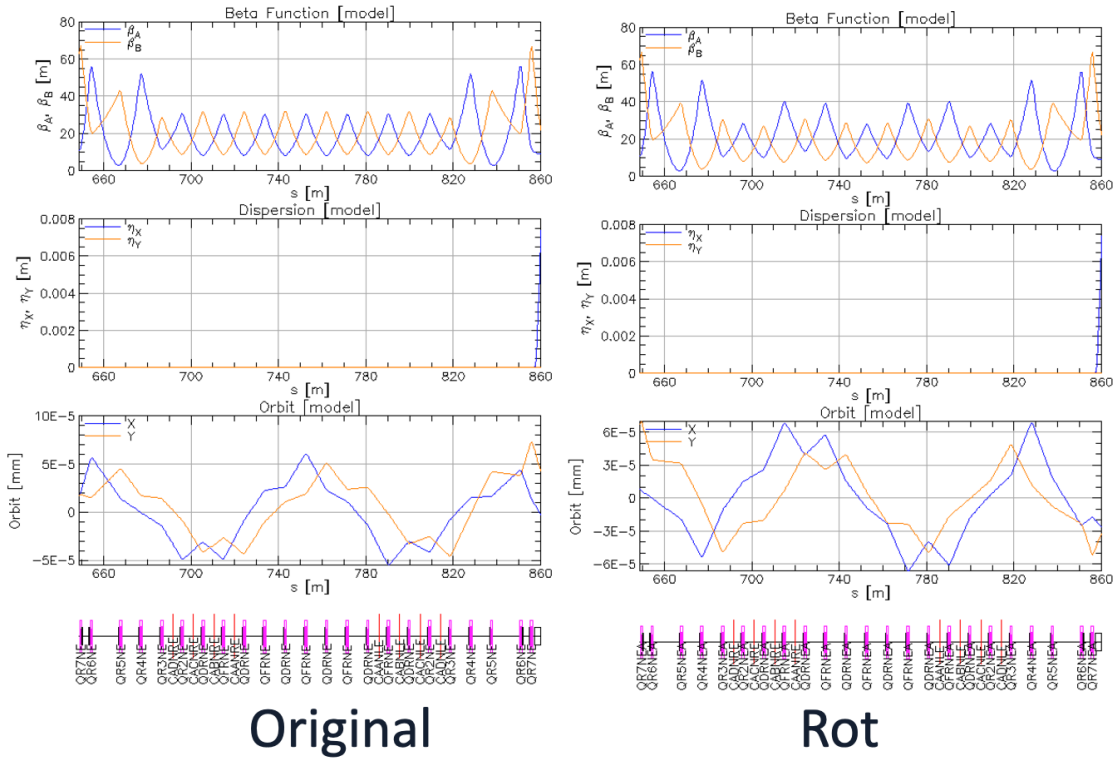

Figure 5.2: Comparison of the straight area before and after performing the Tune match

Another straight area between s =2157 to 2362m in the ring has a symmetric beta functions structure but with wigglers installed, which can not be used for the optimization. If the wiggler is unstalled from this area, it can be used for the Tune match, giving extra degrees of freedom. Additionally, the Tune is an overall machine parameter, so more quadrupoles involved in the optimization can lower the adjustment on individual quadrupoles. If only the fractional component of the Tune can be recovered, either accept the new Tune or step back, modifying the design of the spin rotator to achieve the restorable Tunes.

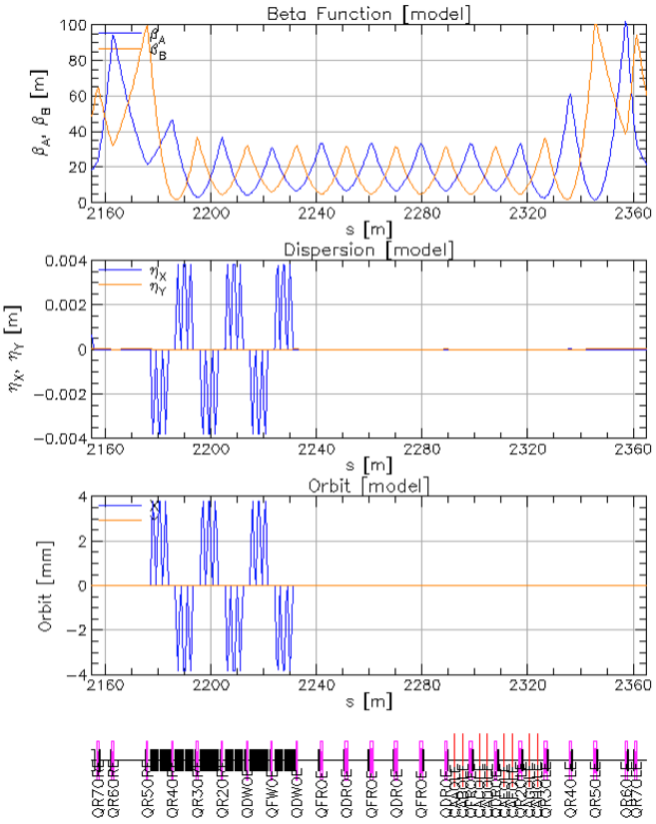

Figure 5.3: Straight area containing the wiggler

The Tune match requires the adjustment of quadrupoles, which changes local optics, thus changing the chromaticities. As mentioned in **Section 4.6**, the adjustment of sextuopoles does not affect optical functions. Therefor, Tunes need to be matched before the chromaticities. Once the Tunes are restored, all touchable sextupoles are adjusted to achieve the maximum dynamic aperture and recover the original chromaticities if possible.

5.2 Long Term Tracking Studies

Once the rotator is fully transparent to the ring, Beam tracking will be taken to examine the stability of the rotator ring and determine the spin polarization lifetime, the beam lifetime, and the dynamic aperture. The beam tracking is implemented with the Long-Term Tracking program built upon the Bmad software toolkit. The Long Term Tracking program is for long term tracking of a particle or a beam possibly including tracking of the spin. The available tracking methods include Map, PTC, and Bmad. The Tracking Method applied to implement the beam tracking is PTC. Tracking with Map computes the Taylor series with a truncate order, which is extremely quick but less accurate compared with two other methods. PTC and Bmad tracks element by element, which is slow but guarantee the accuracy. In addition, PTC can include radiation damping and fluctuations effects [28].

The required amount of beam tracking is 2 million turns in the rotator ring to match the beam topping up rate. The beam tracking with PTC is very computational expensive, the track speed of the current computational device is 70 ms per particle per turn, which requires approximately 4.5 years to track 1000 particles with 2 million turns in the ring on a single machine. Therefore, a computing cluster must be used to perform beam tracking.

Chapter 6

Conclusions

The design of the spin rotator with the dipole-solenoid combined function magnet structure is successfully implemented. The advantage of this design is that the original machine geometry is maintained, providing an alternative plan for future polarization projects such as Electron-Ion Collider (EIC). All new magnets' strengths stay within the technical limit. The longitudinal spin alignment at the IP reaches a significantly high level, greater than 99.99%, which highly satisfies the purpose of beam polarization. Also, the optical rematch is quite successful. The tuning area where the rotator is located does not disturb the outside optical functions. Furthermore, an algorithm is developed which can effectively tune the sextupoles. The original Tunes must be restored to make the rotator fully transparent to the High Energy Ring, and the SF/SD sextupoles have to be adjusted to reach the maximum dynamics aperture. Once the batch computing system is available, beam tracking will be performed to examine the rotator ring's stability and determine the beam and spin polarization lifetime.

Bibliography

[1] Michael Roney. Upgrading SuperKEKB with polarized e- beams. *PoS*, ICHEP2020:699, 2021.

[2] Aleksandrs Aleksejevs, S. Barkanova, Yu Bystritskiy, and Vladimir Zykunov. Application of asymptotic methods to calculating electroweak corrections in polarized bhabha scattering. *Physics of Atomic Nuclei*, 83:307–333, 03 2020.

[3] Vadim Ptitsyn. Lecture notes in Spin Rotators and Snakes in 2021 USPAS summer school, June 2021.

[4] Ya. S. Derbenev and A. M. Kondratenko. Acceleration of polarized particles. *Sov. Phys. Doklady*, 20:562, 1976.

[5] Mei Bai. Polarized protons and siberian snakes. `http://www.phys.virginia.edu/Files/fetch.asp?EXT=Seminars:2000:SlideShow`.

[6] Desmond P. Barber. An Introduction to Spin Polarisation in Accelerators and Storage Rings. `https://www.desy.de/~mpybar/psdump/Redone_CI_lectures_2006.pdf`.

[7] Desmond P. Barber, Michael Böge, H. D. Bremer, Reinhard Brinkmann, W. Brückner, M. Düren, Eliana Gianfelice-Wendt, C. Grosshauser, H. Kaiser, R. Klanner, Mark Lomperski, G. Meyer, Norbert Meyners, Patricia Logan Oelwein, G. Ripken, Klaus Rith, G. Schmidt, Erhard Steffens, W. Wander, W. Wümpelmann, Kirsten Zapfe, and Frank Zetsche. The first achievement of longitudinal spin polarization in a high energy electron storage ring. *Physics Letters B*, 343:436–443, 1995.

[8] Kazunori Akai, Kazuro Furukawa, and Haruyo Koiso. Superkekb collider. *Nuclear Instruments and Methods in Physics Research Section A: Accelerators, Spectrometers, Detectors and Associated Equipment*, 907, 08 2018.

[9] Klaus Wille. *The physics of particle accelerators : an introduction*. Oxford University Press, 2000.

[10] Ryan Bodenstein. *A Procedure for Beamline Characterization and Tuning in Open-Ended Beamlines*. PhD thesis, 12 2012.

[11] S. Y. Lee. *Spin Dynamics And Snakes In Synchrotrons*. World Scientific, 1997.

[12] D. Sagan and D. Rubin. Linear analysis of coupled lattices. *Phys.Rev.*, 2(074001), 1999.

[13] D. Sagan. The BMAD Reference Manual. `https://www.classe.cornell.edu/bmad/manual.html`, 2021.

[14] N. Wang and U. Wienands. Spin Rotator Design for SuperKEKB. *Illinois Accelerator Institute 2019 Internship Project Report*, 2019. `https://www.illinoisacceleratorinstitute.org/2019%20Program/student_papers/Ningdong_Wang.pdf`.

[15] Vladimir N. Litvinenko and Alexander A. Zholents. Compensating effect of solenoids with quadrupole lenses. 1984.

[16] Y. Suetsugu, H. Fukuma, K. Ohmi, M. Tobiyama, John Flanagan, Hirokazu Ikeda, Emy Mulyani, K. Shibata, T. Ishibashi, M. Shirai, Shinji Terui, Kouji Kanazawa, and H. Hisamatsu. Mitigating the electron cloud effect in the superkekb positron ring. *Physical Review Accelerators and Beams*, 22, 02 2019.

[17] Brett Parker, Michael Anerella, John Escallier, Arup Ghosh, Animesh Jain, Andrew Marone, Joseph Muratore, and Peter Wanderer. BNL Direct Wind Superconducting Magnets. *IEEE Trans. Appl. Supercond.*, 22(3):4101604, 2012.

[18] Brett Parker (BNL) and Uli Wienands (ANL). private communication to discuss the technical limit for the combined function magnets.

[19] D. Sagan. Bmad: A relativistic charged particle simulation library. *Nucl. Instrum. Meth. A*, 558:356–359, 2006.

[20] D. Sagan. The Tao Manual. `https://www.classe.cornell.edu/bmad/tao.html`, 2021.

[21] Sad. `http://acc-physics.kek.jp/SAD/index.html`.

[22] Demin Zhou, Maria Biagini, Nicola Carmignani, Haruyo Koiso, Simone Liuzzo, Akio Morita, Yukiyoshi Ohnishi, Katsunobu Oide, David Sagan, and Hiroshi Sugimoto. Lattice Translation Between Accelerator Simulation Codes for Superkekb. In *7th International Particle Accelerator Conference*, page WEPOY040, 2016.

[23] David Sagan and Chris Mayes. An Introduction and Tutorial to Bmad and Tao. `https://www.classe.cornell.edu/bmad/tao.html`, 2021.

[24] David Sagan. private communication to model the rotator magnet with BMAD, 2021.

[25] Katsunobu Oide and Haruyo Koiso. Dynamic aperture of electron storage rings with noninterleaved sextupoles. *Physical review. E, Statistical physics, plasmas, fluids, and related interdisciplinary topics*, 47:2010–2018, 04 1993.

[26] Renjun Yang and Mika Masuzawa. private communication to determine the technical limit for sextupoles, 2021.

[27] Renjun Yang. private communication, 2021.

[28] D. Sagan. Long Term Tracking Program. `https://www.classe.cornell.edu/bmad/other_manuals.html`, 2021.

Appendix A

Additional Information

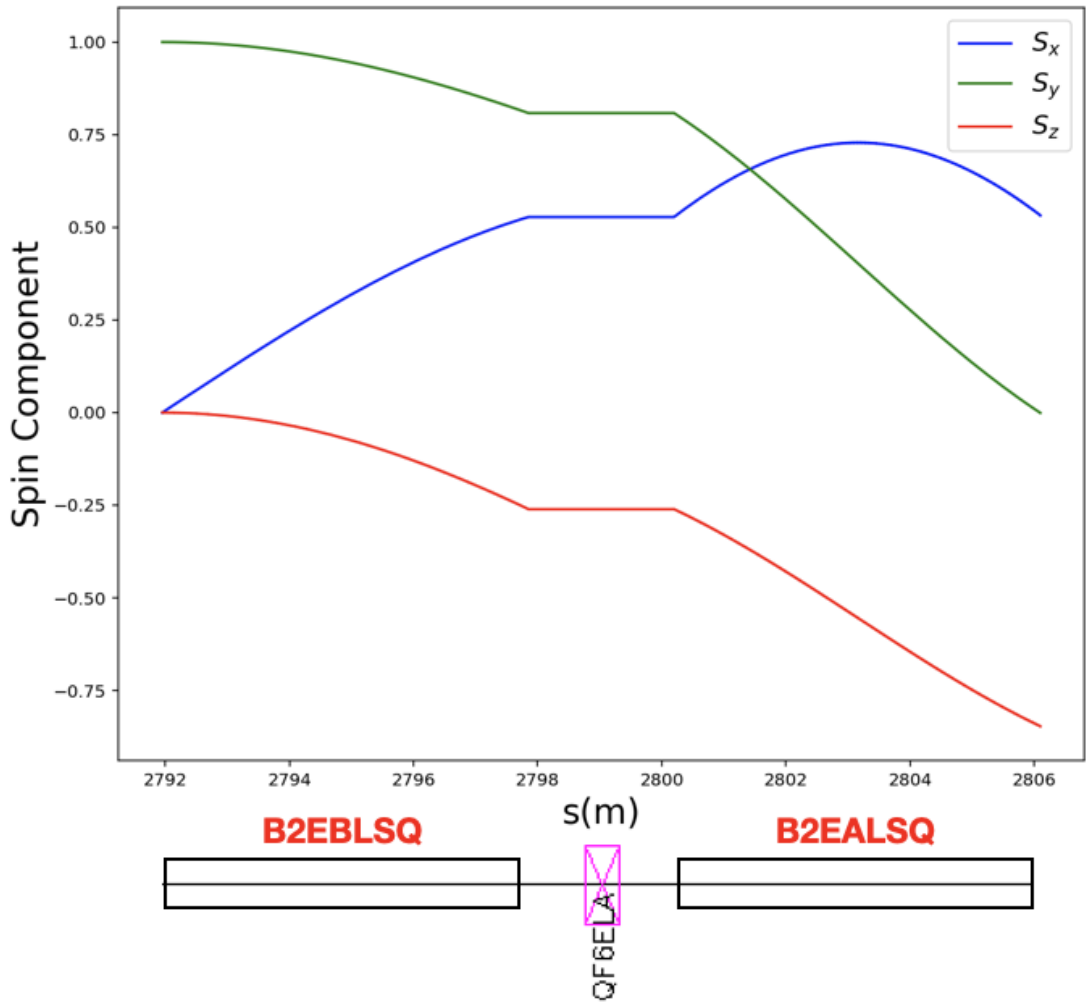

Figure A.1: Spin moition of the electron in the L-Rot (co-moving frame)

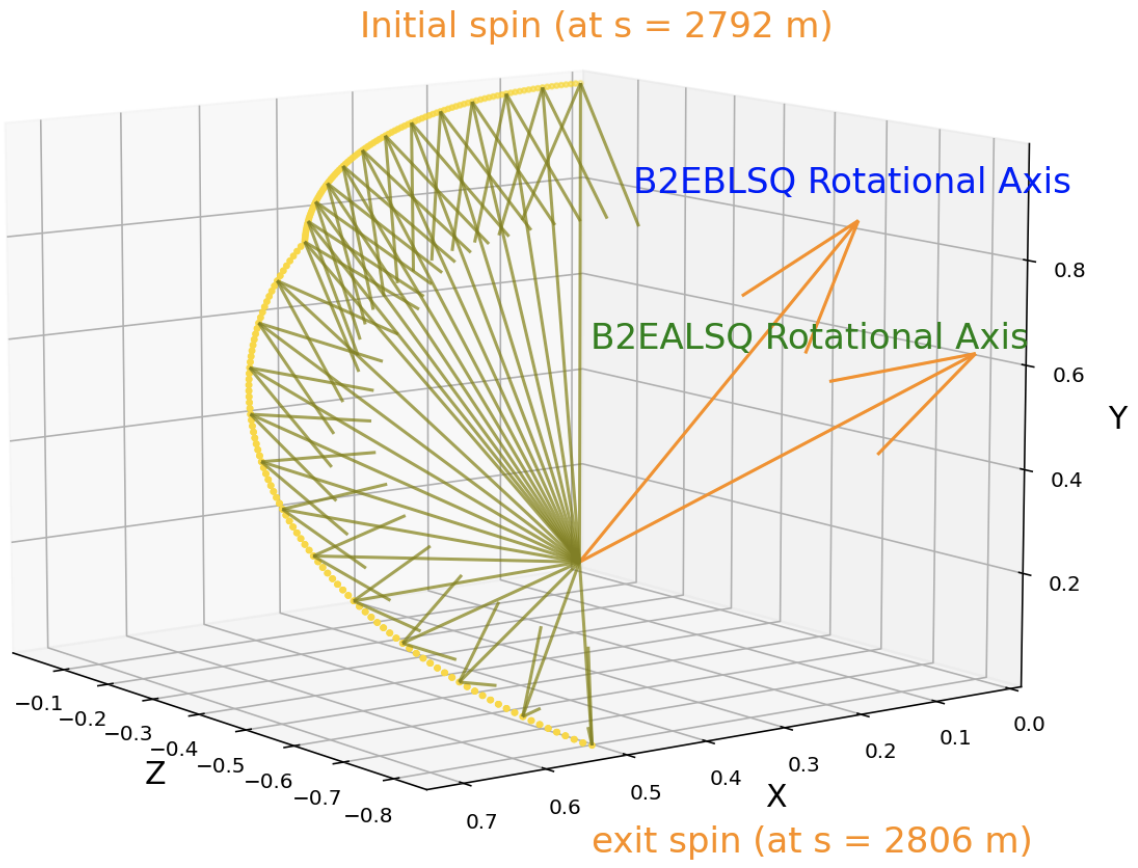

Figure A.2: Spin moition of the electron in the L-Rot (rest frame)

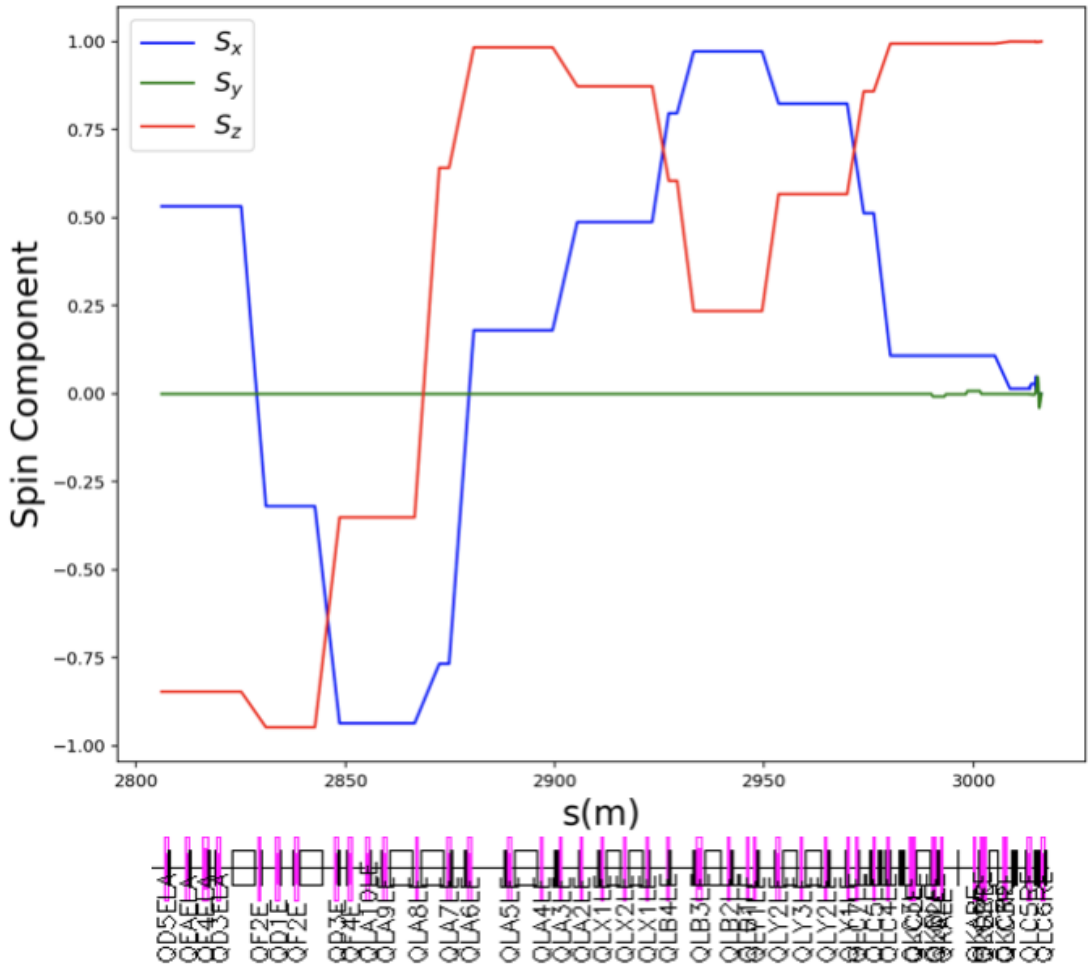

Figure A.3: Spin moition of the electron in the area between the L-Rot and the IP 3020m (co-moving frame)

,

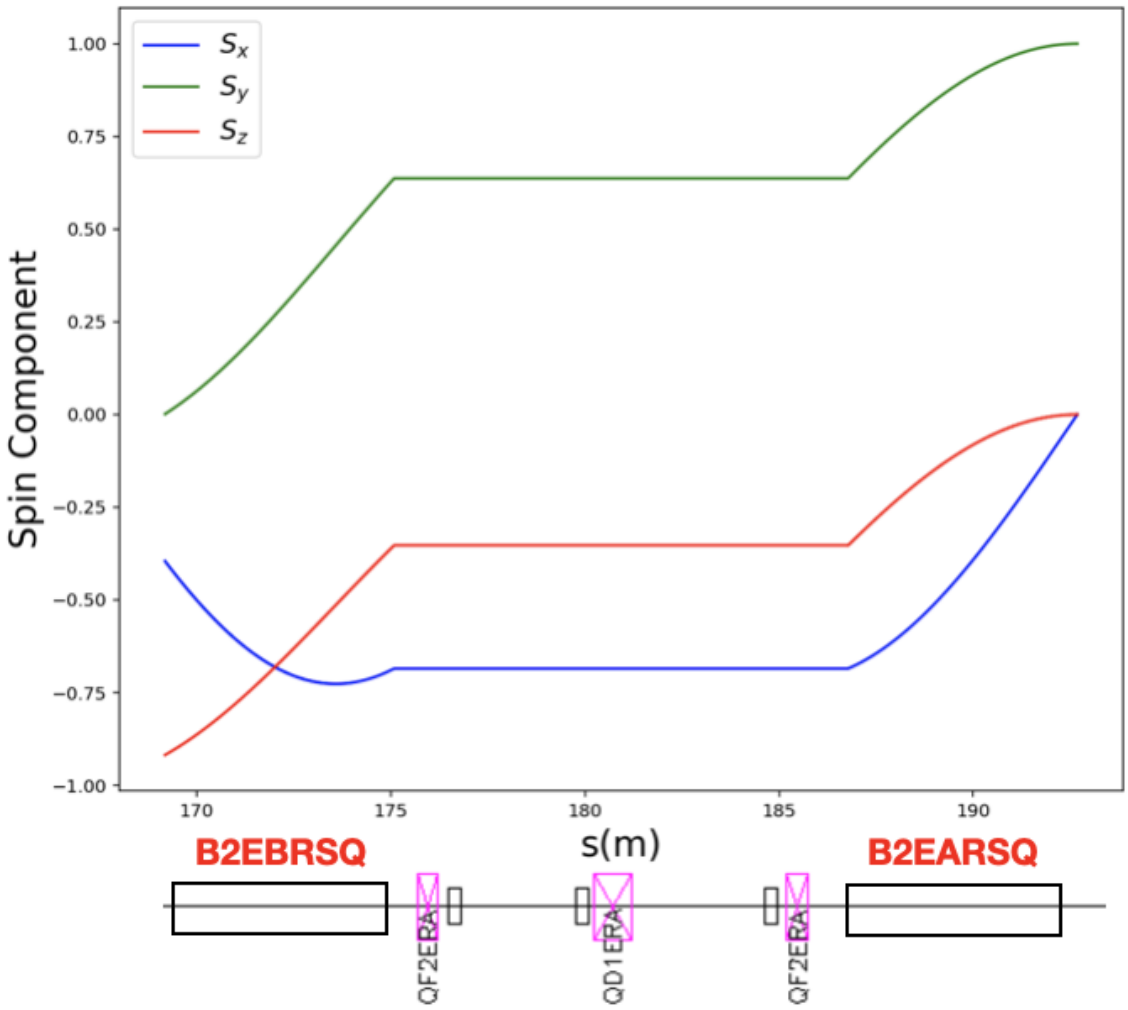

Figure A.4: Spin moition of the electron in the R-Rot (co-moving frame)

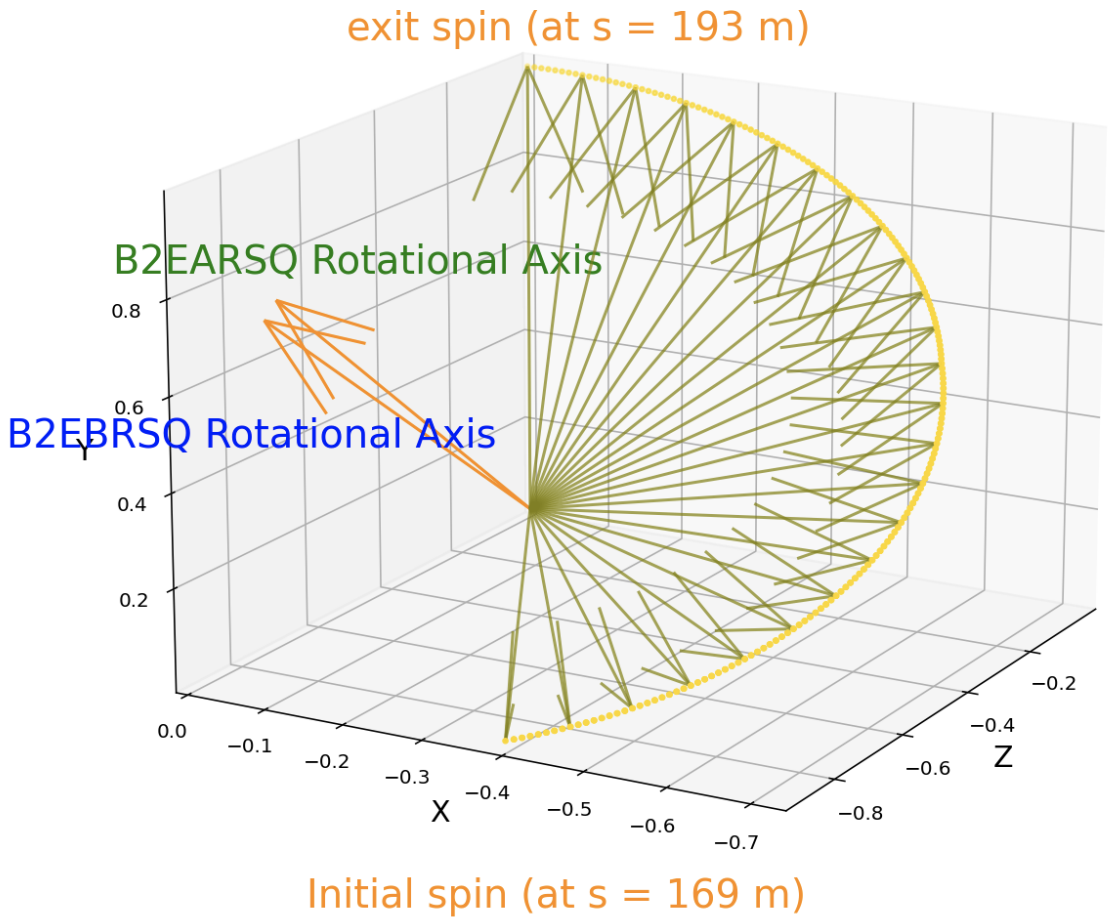

Figure A.5: Spin moition of the electron in the R-Rot (rest frame)

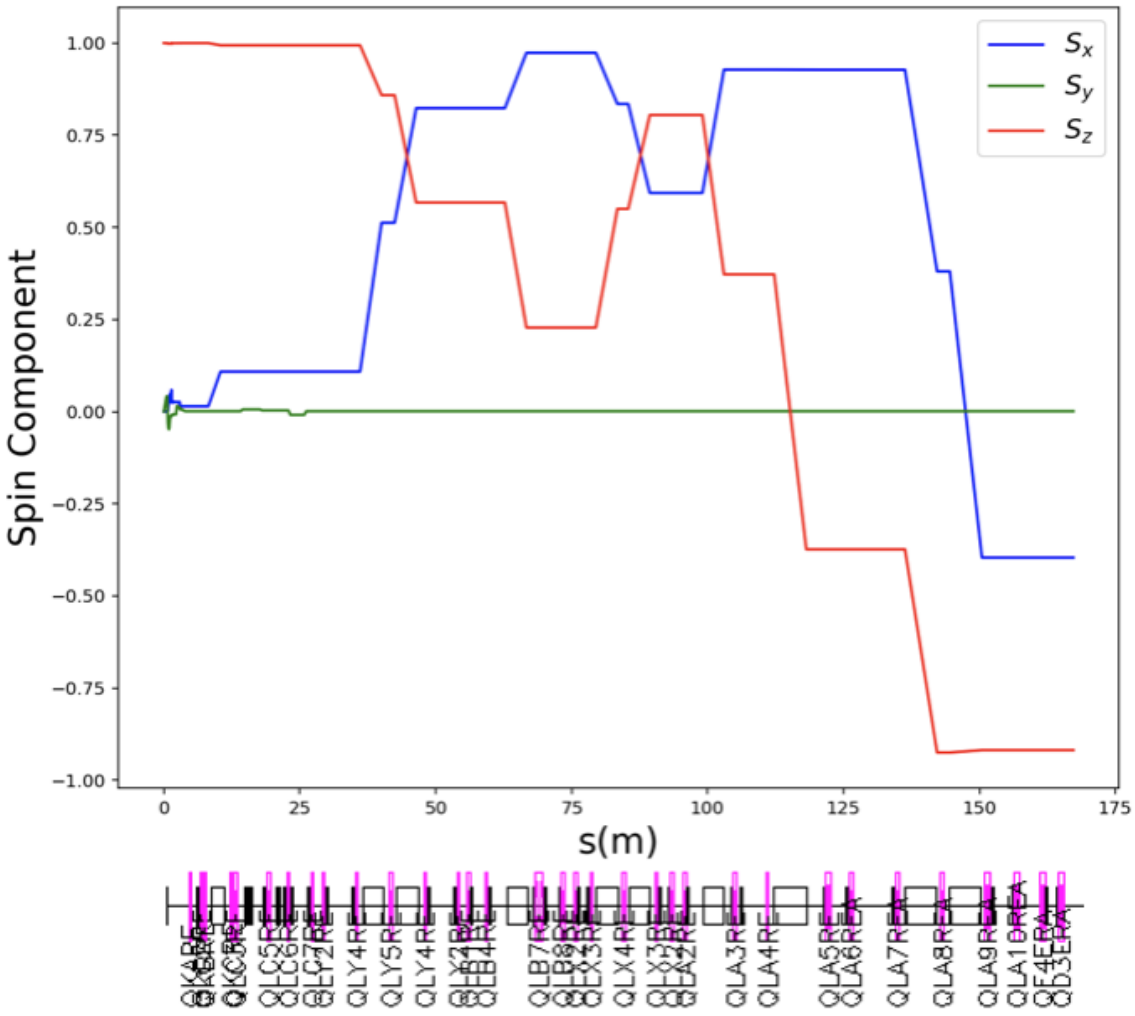

Figure A.6: Spin moition of the electron in the area between the IP (at s = 0) and the R-Rot (co-moving frame)